A Study on iron-based amorphous metals: alloy development, thermodynamics and soft magnetism

Thesis by

Xiao Liu

In Partial Fulfillment of the Requirements

for the Degree of

Doctor of Philosophy

California Institute of Technology

Pasadena, California

2014

(Defended November 12, 2013)

Dedicated to my parents.

Acknowledgments

First of all, I owe my deepest gratitude to my advisor, Prof. William L. Johnson, who has shown his extraordinary scientific talent as a scientist, and excellent guidance as a mentor. I first got interested in Bill's lectures in APh105 - a class on thermodynamics and statistical mechanics. He has my admiration for his passion for science, his profound insights, and his relaxed style of lecturing. After joining Bill's group, I was further intrigued by those long discussions in Bill's office, in the hallway, in the kitchen, and on the balcony of Keck. Bill gave me time, space, research independence, and meanwhile gave me inspiration and encouragement. My research and this thesis could not even be possible without Bill's help and guidance.

My gratitude also goes to the members of my thesis committee. I would like to thank Prof. Brent Fultz, Prof. Julia R. Greer, and Prof. William A. Goddard. They made the discussion on my thesis very interesting and made that day memorable. I truely appreciate that Prof. Fultz gave me the opportunity to come to Caltech and experience five wonderful years. I thank Prof. Greer for those insightful discussions on mechanical behaviors and for her being so kind to let me borrow her textbook. I am very grateful to Prof. Goddard, for his time, consideration and participation to my defense at 8am, from another hemisphere. Thanks to today's telecommunication technology to make it happen.

The members of Johnson group on the third floor of Keck have given me selfless help and countless fun. I would like to thank Dr. Marios Demetriou, for being both a mentor and a friend. Marios has been very patient in teaching me the basic glass-blowing techniques and reading my paper drafts. His high standards of quality have influenced me and encouraged me to pursue the perfection of work. I'm very grateful for our fruitful collaborations over the past few years. Dr. Jong Hyun Na and Dr. Glenn Garrett used to share the same office with me. Now I am alone with three desks, and a lot of interesting memories. Dr. Na is a rather quiet person, but he taught me excellent experimental skills and a rigorous attitude. Dr. Garrett is a true gentlemen, always providing us good food and good scientific suggestions. I would also like to thank Georg Kaltenboeck, for being a great collaborator. Our collaboration dated from the set-up of rapid discharge heating and forming platform, to the development of new alloy. Georg is the experimental master hand in the lab and I have learned a great deal from him. Scott Roberts is another expert in all sorts of pumps, joints, and wrenches, etc.

He has always helped me get problems solved. Andrew Hoff is the youngest member of the group (up to now), yet takes a lot responsibility. Thank you for coordinating our group meetings and for those inspiring chats. I'm also grateful to other Materials Science option members and affiliates: Dr. Doug Hoffman, Dr. Dale Conner, Henry Kozachkov, Joanna Kolodziejska, Jonathan Reyes, Chih-Kai Yang and Mike Vonduras. I thank Pam Albertson for taking care of all the administrative matters for us and keeping the group running smoothly.

I would like to specifically thank Prof. Konrad Samwer and Prof. Marc A Nicolet. They are affiliated with the Johnson group and visit us frequently as most welcomed guests. I was lucky to have many joyful discussions with them which broadened my vision and strengthened my understanding. Their expertise is critical, and I am very thankful for having collaborations with them.

The past five years at Caltech could not have been so vivid without my good friends. They are always there no matter if it is sunny or gloomy (which is very rare in Southern California). I would like to thank these either Techers or non-Techers for sharing those memorable days: Yi Cao, Yalan Ding, Tan Liu, Joyce Zhang, Sharon Wang, Emmy Lei, Liu Yang, Mengtian Sun, Yao Sha, Sha Chang, Wendian Shi, Xin Ning, Wei Mao, Nguyen Phong, Lisa Mauger, Xiaodi Hou, Shuo Han, Sijia Dong, Molei Tao, Gongjie Li, Maolin Ci, Wei Wei, Chenguang Ji, Xiaoqi Ren, and Caren Zhang.

The support from my family is always vital, not only to my research and career, but more importantly, to my entire life. I deeply thank my dear parents, who nurtured me with the best environment they could provide. Finally, my appreciation and love go to my dear husband Alex. He has given me endless love and support, as a boyfriend, a fiance, and a husband.

Abstract

Metallic glass has since its debut been of great research interest due to its profound scientific significance. Magnetic metallic glasses are of special interest because of their promising technological applications. In this thesis, we introduced a novel series of Fe-based alloys and offer a holistic review of the physics and properties of these alloys. A systematic alloy development and optimization method was introduced, with experimental implementation on transition metal based alloying system. A deep understanding on the influencing factors of glass forming ability was brought up and discussed, based on classical nucleation theory. Experimental data of the new Fe-based amorphous alloys were interpreted to further analyze those influencing factors, including reduced glass transition temperature, fragility, and liquid-crystal interface free energy. Various treatments (fluxing, overheating, etc.) were discussed for their impacts on the alloying systems' thermodynamics and glass forming ability. Multiple experimental characterization methods were discussed to measure the alloys' soft magnetic properties. In addition to theoretical and experimental investigation, we also gave a detailed numerical analysis on the rapid-discharge-heating-and-forming platform. It is a novel experimental system which offers extremely fast heating rate for calorimetric characterization and alloy deformation.

Contents

Chapter 1

Introduction

1.1 Metallic Glasses

It was in 1960 that $Au_{75}Si_{25}$ was made noncrystalline directly from liquid state by a rapid-quenching technique. This work by Duwez and his collaborators [1] was the first to demonstrate that liquid-like states can be realized in solid metals and alloys. Since then, metallic glasses have advanced from laboratory samples to commercial products in ribbon form. A lot of alloying systems have since been developed, including Pd-Si-based, Zr-Al-based, Pd-Ni-Cu-P, and Zr-Ti-Be-based systems [2, 3, 4, 5]. There are a number of techniques by which the alloys can be produced in their glassy state and these give rise to a variety of interesting and useful properties. Metallic glass alloys exhibit a range of properties which extend beyond those of crystalline materials. Because the atomic structure of a glassy or amorphous alloy is nonperiodic, it is not uniquely defined. However, an average over the entire structure is reflected in diffraction, magnetic, electrical, chemical, and mechanical properties. Many alloys exhibit high strength and good ductility which make them suitable as reinforcing agents. Others exhibit unique magnetic properties, while some are exceptionally resistant to environmental degradation. Some alloys are expected to possess a surface chemistry not previously known.

Glass is formed by rapid cooling from molten state. When the experimental timescale is short enough, the liquid would become so viscous that it stops flowing and becomes glassified. From a statistical mechanics point of view, when the experimental timescale is short enough to compete with the intrinsic Maxwell timescale of the alloy, the atoms in the alloy are not given enough time to sample all the configurational space to find the stable crystalline state, before they lose their sampling rate. Therefore, they keep the near-liquid configuration which is a metastable glassy state. How large an alloy can be made, is a complicated problem involving both thermodyamics and kinetics. Researchers have so far revealed many parameters with influences on alloy's critical size. However, there is no comprehensive view on the glass forming ability yet. We will try to explain our understanding on this topic in this thesis, especially Chapter 2 and Chapter 3.

1.2 Soft magnetic metallic glasses

Among a set of interesting characteristics of metallic glasses, soft magnetism is of special interest because metallic glasses exhibit excellent soft magnetic properties and offer tremendous potential for application. Soft magnetic materials are used extensively in power electronics and consumer electronics such as transformers, inductors, saturable reactors, magnetic amplifiers, chokes, etc. Here the term "soft magnetic", as the contrary of "hard magnetic", refers to materials which can be magnetized easily, but do not tend to stay magnetized. Usually a small externally applied field can easily magnetize or demagnetize soft magnetic materials. This generally requires that the magnetization be loosely coupled to the material itself, i.e., the material must exhibit a low magnetic anisotropy [6]. Therefore, metallic glasses become an excellent candidate compared to the crystalline counterparts which usually have distinctive preferred axes or directions.

With great researching efforts through the past half century, metallic glasses with various magnetic properties have been obtained through evaporation-deposition and rapid quenching from molten alloy systems which are usually rich in transition metals. Transition metals are those elements with an incomplete d subshell and give rise to paramagnetic individual atoms with unpaird d electron spins. At the beginning, the possible co-existence of amorphism and ferromagnetism was not readily understood and accepted. Gubanov [7] in 1960 first gave a theoretical prediction on the possibility of compatible existence of magnetic ordering and structural disorder. After that, certain magnetic metallic glass thin films had been reported by experimentalists, via evaporation onto cold substrate, chemical reduction and electrolysis. But it was not until 1967 when Duwez and Lin [2] reported an FePC foil from rapid quenching that a metallic glass exhibits good ferromagnetic properties and good thermal stability against crystallization. They not only demonstrated ferromagnetism in glassy FePC, but also unusually soft magnetic properties. Great efforts were spurred by the potential for application of these novel magnetic materials. The large amount of magnetic metallic glasses can be generalized into two categories: the T-M type and the T-T type. The T-M type contains metallic glasses alloyed from transition metals and various kinds of metalloids (such as B, C, Si, P and Ge) to the extent of $15\% - 30\%$ [6]. The first one of this series was reported by O'Handley et al. [8] : $Fe_{80}B_{20}$ with observation of high saturation magnetization and low core loss comparable to silicon steels which are widely used in industry. This composition of $T_{80}M_{20}$ has become the prototype of many alloy designs later. The T-T type contains metallic glasses alloyed from "late" transition metals (such as Fe, Co and Ni) and "early" transition metals (such as Zr, Hf, Y and La). They are very limited in number.

For crystalline transition metals, the Fermi level lies within the energy bands formed from the d electrons. When the effects of alloying disorder are considered, relative few calculations of electronic density of states have been reported. However, abundant experimental research has concluded that

Alloy composition	B_s (T)	T_C (°C)	μ (kOe)	$H_c(Oe)$	ρ ($\mu\Omega cm$)
$Fe_{80}B_{20}$	1.57	320	374	0.04	140
$Fe_{82}B_{10}Si_8$	1.52	300	415	0.17	130
$Fe_{67}Co_{18}B_{14}Si_1$	1.75	200	415	0.08	130
$Fe_{81}B_{13.5}Si_{3.5}C_2$	1.57	300	415	0.08	125
M4-grade silicon steel (Fe-3%Si)	2.03	735	12	0.09	46
H2-grade silicon steel (Fe-3%Si)	2.03	735	30	0.09	46

Table 1.1: Properties of several Fe-based glass-forming alloys [6]

in these transition metal based metallic glasses, density of states still arise from d electrons, in spite of the reduction due to charge transfer and/or hybridization [7]. Because of the absence of a crystal lattice, the magnetic moment in amorphous ferromagnets is not coupled to a particular structural direction, so there is no magneto-crystalline anisotropy. Moreover, since the material is magnetically homogeneous at length scales comparable to the magnetic correlation length, the intrinsic coercivity is small [9]. Comparison in Table 1.1 between magnetic amorphous and crystalline alloys show that the former has lower Curie temperature, higher permeability, lower coercivity, and higher electrical resistivity [6].

The merits of magnetic metallic glasses boost considerable interests on commercial applications. They are currently used widely in power electronics, telecommunication equipments, sensing devices, electronic article surveillance systems, etc. Amorphous magnetic inductors also find applications in pulse power devices, automotive ignition coils, and electric power conditioning systems [10]. All of these applications are possible because of faster flux reversal, lower magnetic losses, and more versatile property modification achievable in amorphous ferromagnets. Since 1980s a series of ferromagnetic metallic glasses were introduced and commercialized under the trade name "Metglas". They can only be made into ribbons of thickness in tens of micrometers due to their very limited glass forming ability. These materials are produced by melt spinning on a copper wheel which resulted in quenching at rates of $10^3 - 10^5$ K/s. Then the ribbons are laminated concentrically to form cores of desired shapes and sizes. Although successful, this process had inherent deficiencies: it is a laborious and expensive laminating process. Besides, there is a low core-packing density due to the air gaps left between the thin foils needed to build up the core, which reduces the overall core efficiency. One of the principle motivations of my last three years' research is to design and understand novel metallic glass materials with good soft magnetism as well as satisfactory glass forming ability and thermal stability. Bulk materials, different from thin ribbons, provide excellent candidates which could yield cost-effective processing and defect-free end products.

Chapter 2 describes in detail how this novel series of Fe-based magnetic metallic glasses were developed. A systematic alloy development and optimization method was introduced. An experimental implementation of this approach was conducted on transition metal based alloying system. Experimental conditions and procedures were reported, as well as abundant results.

Chapter 3 offers a holistic review of the thermodynamics and glass forming ability of the novel Fe-based alloys. First, a deep understanding on the influencing factors of glass forming ability was introduced, based on classical nucleation theory. Experimental data of the new Fe-based amorphous alloys were interpreted to further analyze those factors, including reduced glass transition temperature, fragility, and liquid-crystal interface energy. Various treatments (fluxing, overheating) were discussed for their influences on the alloying systems' thermodynamics and glass forming ability.

Chapter 4 presents some results and analysis which indicate the alloys' soft magnetism. Multiple experimental approaches have been introduced to characterize the alloys. A specific sample preparation procedure through casting is discussed.

Chapter 5 gives a detailed analysis on the rapid-discharge-heating-and-forming (RDHF) platform. RDHF is a novel experimental system which offers extremely fast heating rate for calorimetric characterization and alloy deformation. We investigate its working mechanism and the underlying physical principles, and use finite element analysis for dynamic simulation. The numerical simulation results are in good match with the experimental results.

Chapter 2

Alloy Development and Optimization

2.1 Idea of composition optimization

After the first introduction of $Fe_{80}B_{20}$ glass ribbon by O'Handley et al. in 1976 [8], the $T_{80}M_{20}$ composition (T for transition metals and M for metalloids) has served as the prototype of various compositional derivatives and modifications [11, 12]. These research efforts mainly address the variation and substitution in transition metals (T) or metalloids (M). The first case includes replacing with or adding new elements such as Co, Ni, Nb, Mo, Cr to the Fe content. Some results based on the $T_{80}M_{20}$ were presented in Table 1.1 of Chapter 1. The "Metglas" series shown in Table 1.1 all come in ribbons with size of tens of micrometers. In order to overcome the deficiencies associated with thin ribbons, great efforts have been made to develop magnetic amorphous alloys with better glass forming ability and more robust thermostability. For example, Shen and Schwarz [13] reported a ferromagnetic metallic glass capable of forming bulk three-dimensional amorphous hardware with thickness up to 4mm. Inoue et al. [14] reported a cobalt-based bulk glassy alloy of 1.5mm with ultrahigh strength and permeability, but yet low saturation magnetization. Recently progresses were reported by Demetriou et al. [15] from Caltech group. They used a micro-alloying approach to develop bulk ferromagnetic alloys capable of forming glasses up to 6mm while exhibiting fracture toughness twice as the early bulk alloys. Some of the recent discoveries were present in Table 2.1.

However, after reviewing the course of new metallic glass development, one will not hesitate to conclude that the exhaustive search (with some intuition and hint, of course) requires tremendous time and labor resource while the result and improvement may not be satisfactory. Actually it is not exhaustive enough especially for alloys with multiple constituents. New materials development is always the frontier of materials science research. To address this problem, we have explored new approaches and developed a systematic development and optimization method. This method originates from the general idea of optimization problem, which will be discussed in this section. In

Alloy composition	Bs (T)	GFA (mm)
$Fe_{65.5}Cr_4Mo_4P_{12}C_5B_{5.5}$	0.89	4
$Fe_{20}Co_{43}Ta_{5.5}B_{31.5}$	0.49	1.5
$Fe_{70}Ni_5Mo_5P_{12.5}C_5B_{2.5}$	1.02	4
$Fe_{69}Ni_4Co_2Mo_5P_{12.5}C_5B_{2.5}$	1.04	4
$Fe_{68}Ni_2Co_5Mo_5P_{12.5}C_5B_{2.5}$	1.07	3
$Fe_{72}Ni_3Mo_4P_{11.5}Si_1C_5B_{2.5}$	1.12	4
$Fe_{68}Ni_3Co_5Mo_4P_{11.5}Si_1C_5B_{2.5}$	1.15	3

Table 2.1: Some recent progresses on magnetic bulk amorphous alloys [13, 14, 15]

next section we will describe a concrete case as an implementation of the method with abundant experimental data.

The concept of optimization is not new at all. Other than in mathematics, it has found wide application in statistics, computer science, management science and empirical sciences. An optimization problem deals with maximizing/minimizing a real function by systematically choosing input values from within an allowed set. In a broader context, an optimization problem includes finding the best available value of some given objectives within a given domain, where the definition of "best", objectives and domain could all be controversial to quantify. In our exploration process we started with the simplest case of single objective function of glass forming ability and extended to multiple objectives including various magnetic properties and processability. While scientific research often deals with generalized and idealized cases, trade-offs among various objectives are always prevalent in real world situations.

When the objective function is smooth or differentiable, there exist many algorithms and techniques to solve optimization problems. Iterative methods include gradient descent, Newton's method (finding the root of derivative function), quasi-Newton method (finding the stationary point to make gradient zero), etc., while heuristic methods can help speed up the algorithm and find approximate solutions. The partial derivatives of a local optimum (not necessarily a global optimum) are zero, which inspires a practical iterative optimization method for alloy composition development.

Assume that an alloying system consists of n elements, then we have n-1 degrees of freedom to denote the composition as (Element 1)$_{c_1}$(Element 2)$_{c_2}$...(Element n-1)$_{c_n-1}$(Element n)$_{1-c_1-c_2-...-c_{n-1}}$. Ideally the glass forming ability of the system is a function of c_1, c_2, ..., c_{n-1} as $GFA(c_1, c_2, ..., c_{n-1})$. For a local optimum (here should be maximum for the GFA function) we have

$$\frac{\partial GFA}{\partial c_i} = 0, \forall i \tag{2.1}$$

When the partial derivatives cannot be expressed explicitly, we resort to iterative methods to search for optima. First, choose an appropriate starting point. When a system has multiple local

optima, a random starting point may lead the iteration into a local optimum nearby and afterwards it is very difficult to escape out of this local optimum into another one. Therefore it is important to choose the starting point to be within the promising vicinity of the global optimum. This requires some experience and an intuitive understanding of the alloying system. A general guideline is that we look for good glass formers near deep eutectic compositions. For systems with many comprising elements, there exist many phase diagrams in varous databases which are very helpful. From the starting point composition $P^{(0)} = (c_1^{(0)}, c_2^{(0)}, ..., c_{n-1}^{(0)})$, coordinate values of c_2 till c_{n-1} are fixed. And we vary c_1 within certain range defined by the experimental design until a partial optimum is found at $P_1^{(1)} = (c_1^{(1)}, c_2^{(0)}, c_3^{(0)}, ..., c_{n-1}^{(0)})$, which satisfies

$$\left.\frac{\partial GFA}{\partial c_1}\right|_{P_1^{(1)}} = 0 \tag{2.2}$$

The notion $P_i^{(j)}$ has the meaning of optimizing the $i-$th coordinate c_i during the $j-$th iteration. After getting $P_1^{(1)}$, we keep $c_1, c_3, ..., c_{n-1}$ fixed to process c_2 until the partial optimum for c_2 is found at $P_2^{(1)} = (c_1^{(1)}, c_2^{(1)}, c_3^{(0)}, ..., c_{n-1}^{(0)})$, which satisfies

$$\left.\frac{\partial GFA}{\partial c_2}\right|_{P_2^{(1)}} = 0 \tag{2.3}$$

$$\begin{aligned}
\left.\frac{\partial GFA}{\partial c_1}\right|_{P_2^{(1)}} &\approx \left.\frac{\partial GFA}{\partial c_1}\right|_{P_1^{(1)}} + \bigtriangledown\left(\frac{\partial GFA}{\partial c_1}\right)\Big|_{P_1^{(1)}} (P_2^{(1)} - P_1^{(1)}) \\
&= 0 + \bigtriangledown\left(\frac{\partial GFA}{\partial c_1}\right)\Big|_{P_1^{(1)}} (0, c_2^{(1)} - c_1^{(1)}, 0, ...0) \\
&= \left.\frac{\partial^2 GFA}{\partial x_1 \partial x_2}(c_2^{(1)} - c_2^{(0)})\right|_{P_1^{(1)}}
\end{aligned} \tag{2.4}$$

In this first step of Eqn. (2.4) we have neglected higher order terms. With the assumption that we are in the vicinity of the target, we approximate the expansion with the first two leading terms. Apparently the second-order partial derivative $\frac{\partial^2 GFA}{\partial c_1 \partial c_2}$ determines how far we deviate from the partial optimum of c_1 when we optimize along c_2 direction. Ideally when c_1 and c_2 are orthogonal directions, this second-order partial derivative vanishes, which guarantees that the optimizing of c_2 will not affect the previous result when $c_1 = c_1^{(1)}$. The orthorgonality of c_1 and c_2 indicates that Element 1 and Element 2 are making independent influences to the system's thermodynamics. The nucleation events containing Element 1 and Element 2 are two distinctive phases. In real situation this is not always the case, i.e., there may be a primary nucleation phase containing both Element 1 and 2. Then the natural coordinates c_1 and c_2 are not independent. However, the natural coordinates c_i can undergo a linear transformation to yield a set of orthorgonal coordinates which are the intrinsic eigenvectors of the given system. The physical significance of this set of orthorgonal coordinates will

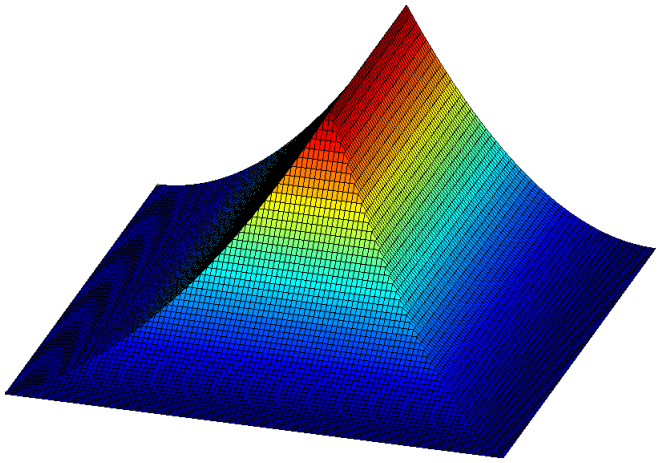

Figure 2.1: GFA landscape

be discussed in detail later.

Following this process, after all n-1 degrees of freedom are processed, we have completed one round of optimizing iteration to reach $P^{(1)} = (c_1^{(1)}, c_2^{(1)}, c_3^{(1)}, ..., c_{n-1}^{(1)})$. We may continue with $P^{(1)}$ to run k iterations until the target function GFA converges and we get a good enough optimum at $P^{(k)} = (c_1^{(k)}, c_2^{(k)}, c_3^{(k)}, ..., c_{n-1}^{(k)})$. From an experimental point of view, often times $P^{(1)}$ or $P^{(2)}$ is already a good result since the uncertainty from experimental conditions may obscure the accurate convergence of the target function. We are satisfied when the incremental improvement after each step is well within the range of experimental error.

The above mathematical discussion is only valid for differentiable functions, i.e., the GFA dependence on composition is differentiable. This requires that there is only one type of underlying crystallization behavior, which is an oversimplified case of the reality. In reality, each crystal phase/crystallization behavior corresponds to a differentiable surface in the GFA space. The overall GFA landscape consists of multiple such surfaces and is piecewise differentiable, as illustrated by Figure 2.1. Where two surfaces intersect, there is a "ridge". A "peak" may be the intersection of three or more crystallization events. At "peak" or "ridge", the GFA function is not differentiable. Yet the optimization approach is still applicable. We can still find the optimum value by varying only one coordinate at each step.

A rough estimation will give us a comparison: for an n-dimensional system with $\sim m$ steps along each coordinate direction, while this optimization method uses $\sim n \times m$ data points to identify a reasonable approximate optimum, a conventional exhaustive search will need $\sim m^n$ data points to

cover the whole searching region. For a ternary alloying system with $n = 2$ (note that 3 elements correspond to 2 degrees of freedom) and $m = 10$, the work load comparison is 20 *vs.* 100. For systems with more comprising elements, the advantage of the optimization approach is more significant. We have successfully implemented this optimization algorithm for Fe- and Ni-based systems [16]. A detailed study for Fe-based alloy development will be reported in next section. We would like to add that from a mathematical point of view, there exist many other, sometimes even faster, optimization algorithms; however, this algorithm stands out because it doesn't require much foresight from the system and therefore it is very easy to follow.

2.2 Implementation for Fe-based amorphous alloys

2.2.1 Problem description

After introducing the optimization idea in the previous section, we hereby describe an example which has successfully implemented this optimization method to develop novel Fe-based soft magnetic metallic glasses.

Compared to pure transition metals, the various transition metal based metallic glasses have those 3d magnetic moments diluted by non-magnetic impurities. They have a density of states at the Fermi level which is more or less depressed. Nevertheless, the d-character of these states is basically preserved [7]. Therefore, the issues of magnetic ordering and impurity states in transition metal based metallic glasses are usually treated in d-band hosts. Generally, the case of dilute impurities in an amorphous matrix is very hard to give quantitative description. It is difficult to predict which impurity has what magnetic moment in which host above what temperature. We will not go into detailed discussion here, except for trend description. Interested readers may refer to Durand's papers [7, 17] for further reading.

From the view of diluted moments, Fe and Co are chosen as the base elements of the system since they have the largest magnetic moment per atom. For Fe, Co and Ni, the magnetic moment (in unit of Bohr magnetons) per atom is ∼2.6, 1.6, 0.6 respectively. Slater-Pauling curve in Figure 2.2 shows the atomic moment (in unit of Bohr magnetons) as a continuous function of the number of 3d and 4s valence electrons per atom across the first series of transition metals [18]. It suggests that Fe-Co alloy may result in stronger ferromagnetism. The average Fe(Co) moment was found to be practically the same in crystalline and amorphous modifications of Fe(Co) compounds [17].

Starting from the prototype $Fe_{80}B_{20}$, efforts have been made to replace with or add into B other metalloids. Among all of them the addition of Si has been found to be advantageous because it has a remarkable tendency to incease the thermal stability without obvious sacrifice of saturation magnetization or Curie temperature [6]. A hindsight from later experiments (see Chapter 3 sections 3.5-3.8 for more details) reveals that Si helps stablize oxygen impurity into amorphous silicon oxide

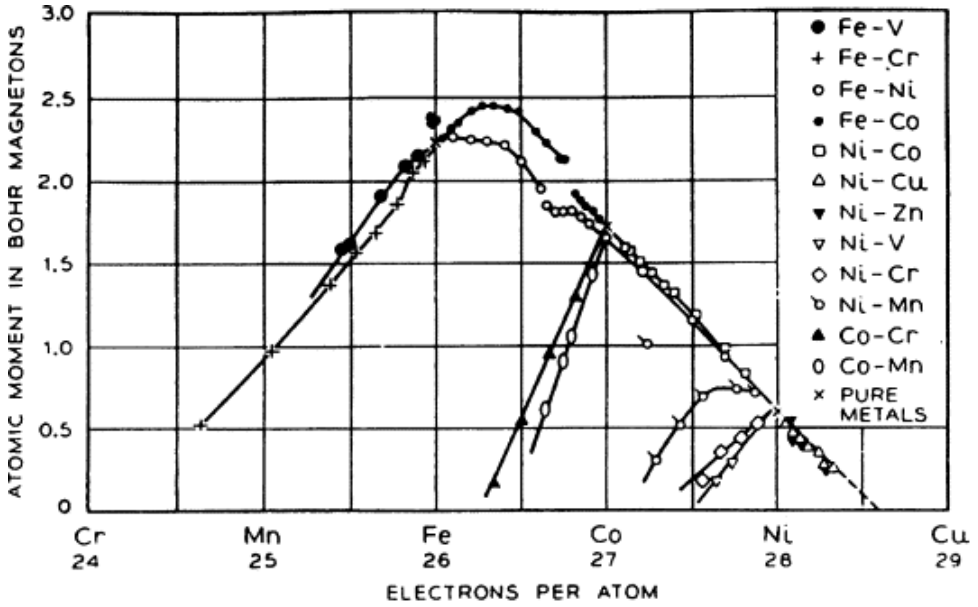

Figure 2.2: Slater-Pauling curve

which benefits the whole alloy's glass forming ability. Fe-Si-B system is a major type of alloy widely utilized in industries. The addition of P may also help to stabilize Fe-rich alloys. It has been found that 2% of P can effectively increase the critical thickness of amorphous $Fe_{78}Si_9B_{13}$ from 50 μm to 90 μm [19]. Moreover, the addition of P may help reduce the alloy's liquidus temperature, which yields a lower reduced glass transition temperature and a potential for better glass forming ability. The influence of reduced glass transition temperature will be discussed in further detail in section 3.3 of Chapter 3. Other candidate metalloids include C and Ge. Replacing B with $\sim 5\%$ C helps improve the room temperature magnetization, yet powder carbon makes it difficult to prepare good quality alloys and actually decreases the saturation. For simplicity, we will choose a five component system of Fe-Co-Si-B-P.

To choose a good starting composition, alloy phase diagrams were resorted to search for deep eutectic points which might be potential compositions of glass formers. Alloy phase diagrams are of significant use for materials scientists and engineers. They make it more efficient and cost effective to develop new alloys with specific applications and to design treatment procedures for specifically required properties. Figure 2.3 presents the ternary phase diagrams for Fe-Si-B system and Co-Si-B system from ASM alloy phase diagram database. The junction of the multiple liquidus projections represents a eutectic trough. With the phase diagrams and the prototype of $Fe_{80}B_{20}$ taken into account, we choose metal (Fe, Co) ~ 75 atomic percentage. From the phase diagrams, the eutectic points appear to have similar Si and B atomic percentages. Thus for the starting composition, we choose the similar values for Si and B and add in a little of P. For the five-element system Fe-Co-Si-

B-P we denote the four degrees of freedom as follows: x, total metal content; y, ratio of % Fe out of % total metal; u, ratio of % (Si-B) out of % total metalloid; v, ratio of % P out of %total metalloid. Therefore the composition is expressed as $(Fe_yCo_{1-y})_x(Si_{(1+u-v)/2}B_{(1-u-v)/2}P_v)_{100-x}$. They are chosen like this with a little ex ante consideration that metals are grouped together and metalloids are grouped together. Theoretically this choice could be arbitrary but the guess for intrinsic nucleation phases could help identify the steepest direction therefore expedite the optimization algorithm. The initial composition is chosen as $Fe_{20}Co_{56}Si_{10.5}B_{8.5}P_5$ which corresponds to x=76, y=0.26, u=0.08, v=0.2.

2.2.2 Experimental method

First, ingots of FeCoSiBP metallic glasses were prepared by induction melting pure Fe (99.95%), Co (99.95%), Si (99.9999%), B (99.5%) and P (99.9999%) in Ar atmosphere at negative pressure. All elements were sealed in a quartz tube with Fe, Co, Si, B pieces mixed as much as possible and P pieces set aside, so that P could be controlled to heat up later to avoid severe evaporation loss. P was weighed 1% more than the nominal composition to compensate for this loss during melting. The weight loss should be checked after melting to make sure that it is within ∼1% of P weight. When the composition was near eutectic point, no obvious sublimation of P was observed. Otherwise, red/orange sediment would adhere to the upper part on the inner wall of the quartz tube. This may indicate non-eutectic composition.

The ingot was then fluxed with boron oxide in Ar atmosphere at positive pressure to remove oxygen impurity in the alloy. The principle and effect of fluxing will be further discussed in detail in section 3.7 of Chapter 3. The atmosphere pressure was set to be positive so that the sublimation of P would be mostly suppressed.

After fluxing, the ingot was fully melted in Ar atmosphere at negative pressure. It was then cast into quartz capillary by Ar flow and water-quenched to form needle-shape metallic glass. The needle diameter ranged around 0.3 mm to 3 mm. Quartz capillary wall thickness was around 0.1-0.2 mm; yet it was not controlled to a high precision and the wall thickness near bottom (with diameter 2-3 mm) could be considerably larger. The capillary technique was specifically for developing metallic glasses with small glass forming ability. For alloys with glass forming ability above 1 mm, capillaries were replaced by standard quartz tubes with various sizes which can be purchased at reasonable prices.

Samples' glass forming ability was characterized by Netstch DSC at 20 K/min in Prof. Johnson's lab. Structure characterization and analysis were facilitated by XRD of Prof. Haile's lab and SEM of GPS division.

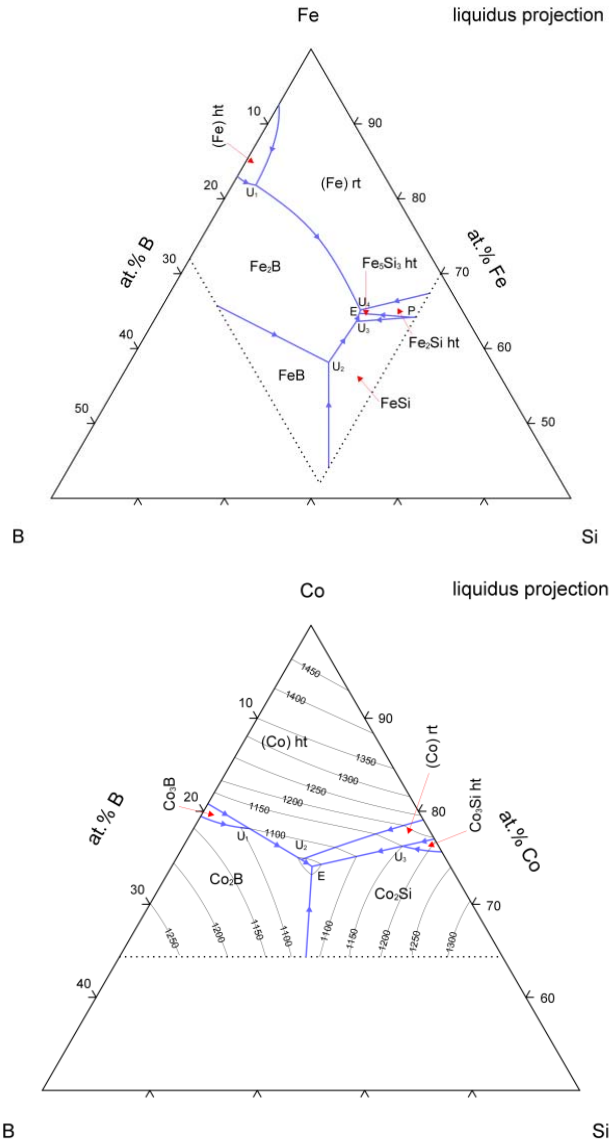

Figure 2.3: Ternary phase diagrams: Fe-Si-B and Co-Si-P

2.2.3 Glass forming ability results

We started with the initial composition $Fe_{20}Co_{56}Si_{10.5}B_{8.5}P_5$. Note that this corresponds to x=76, y=0.26, u=0.08, v=0.2 in the alloy system notation $(Fe_yCo_{1-y})_x(Si_{(1+u-v)/2}B_{(1-u-v)/2}P_v)_{100-x}$. The four degrees of freedom were optimized one by one. After two rounds of interation, we have improved glass forming ability to about 1mm. Some experimental results are presented in Figure 2.4. The first panel shows the GFA variation with total metal content, i.e., for the four coordinates we have chosen before, x varies from 74 to 80, while the other three are fixed. A cusp exists at around x=77, which yields $Fe_{20.5}Co_{56.5}Si_{10}B_{8.5}P_{4.5}$.

The second panel follows from the previous result for further optimization within metal contents, i.e., coordinate y is being optimized while other three are fixed. As y varies from around 0.2 to 0.9, we are actually varying Fe content from 20, 30, ... to 70. Here the change in glass forming ability is significant. It is more than doubled from less than 1 mm to larger than 2 mm. There appears to be a "plateau" for Fe 50 to 60, instead of a single peak as in panel (a). This may be due to any experimental error for the data point at Fe 55, or due to any heterogeneous effect which overshadows the effect of intrinsic crystallization. Considering the slopes at both sides, we think the cusp at around 60% Fe gives a local optimum. From a hindsight, this 60% Fe local optimum is also located at the top of Slater-Pauling curve, which indicates that the composition with best glass forming ability may actually have a "side effect" of excellent magnetism optimization.

The third panel varies P percentage from 4 to 10, which corresponds to coordinate v from around 0.2 to 0.5. Glass forming ability was further enhanced to above 3 mm, with the optimum at around 7% P. For all the three panels here, the data presented give the lower limit of the glass forming ability, because we did needle diameter test for incremental increase, with an error bar of 0.2 mm, i.e., for a data point at 1 mm GFA in Figure 2.4, the actually GFA lies between 1 mm and 1.2 mm.

When glass forming ability in capillary reaches 2 or 3 mm, it is better to transfer the casting process from capillary to standard tube since the latter provides a more uniform control of cooling rate and therefore reduces experimental uncertainty. Quartz tubes with inner diameters 2 mm - 4 mm and wall thickness 0.5 mm were used to cast amorphous metal rods. Figure 2.5 shows a photo with the capillary and tube, as well as the as-cast needle and rod.

2.3 A look-back and better understanding on the optimization approach

2.3.1 Some considerations on crystallization

Since the amorphous alloy is essentially a metastable state, it inherently possesses the tendency to transform into a more stable crystalline state. However, the excellent properties of metallic

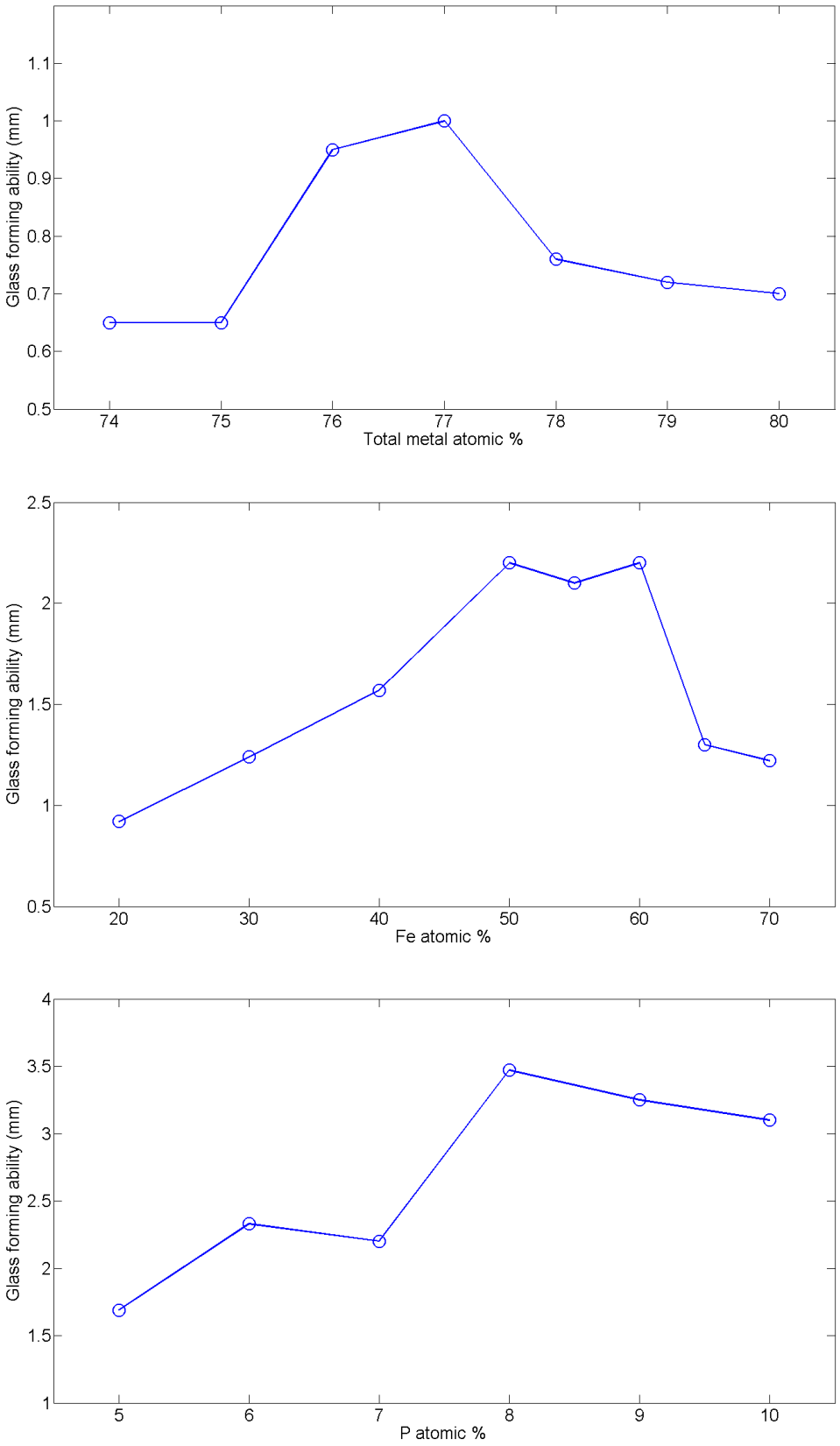

Figure 2.4: Glass forming ability dependence on composition

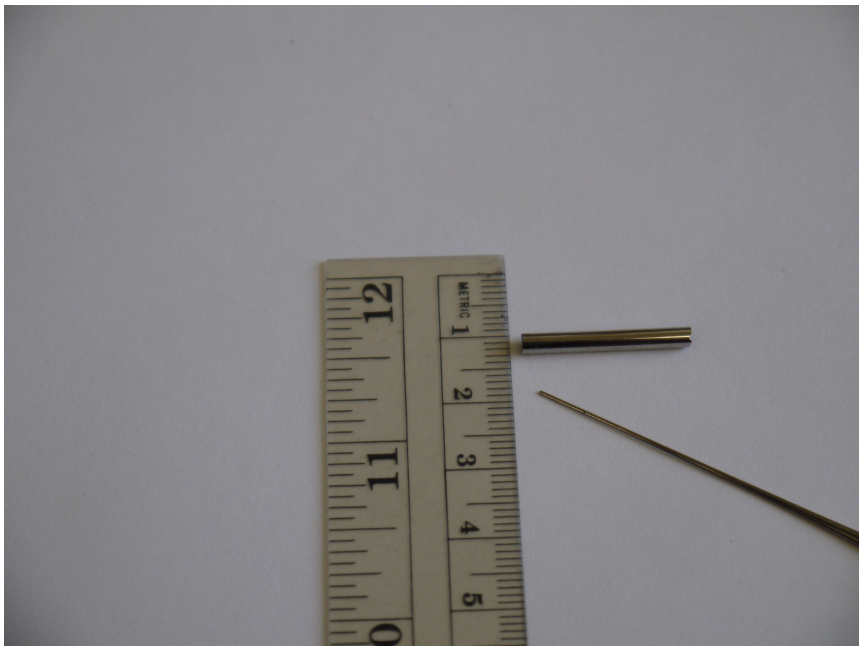

Figure 2.5: Capillary and tube, needle and rod

glasses, including magnetic behavior, high strength, high corrosion resistance. etc., will deteriorate drastically during crystallization. Therefore, it is rather crucial to understand the micromechanisms of crystallization [20]. On the other hand, controlled crystallization can be used to design very special partially crystalline materials, such as the high-toughness and high-ductility composites developed by Hofmann et al. [21]. Crystallization in metallic glasses is of utmost importance, but also with extreme complication. The crystallization behavior depend on a variety of parameters: the phase of crystallization, the number of quenched-in nuclei, the activation energy for diffusion, and the driving force. Driving force is the free energy difference between the amorphous and crystalline phases, which may be represented through a schematic diagram as Figure 2.6.

Panel (a) is a eutectic crystallization situation. At eutectic temperature, the liquid phase, α phase and β phase have a common tangent with slope k_E, which touches the liquid curve at eutectic composition c_E. α and β are two typical crystalline phases each at one side of the eutectic point. When the concentration deviates from c_E towards α phase, c_1 is called hypoeutectic, while c_2 towards β is called hypereutectic.

As shown in panel (b), when there is undercooling, the temperature is lowered to below eutectic point, and the liquid curve is moved upward relative to the crystalline curves, because of the expression $dG = VdP - SdT$. When the composition is at c_E, this is called eutectic crystallization. Eutectic crystallization is the simultaneous crystallization of at least two crystalline phases at the same time. The driving forces to form α and β precipitates are indicated by arrows. The two driving forces are the same because α and β share the same parallel tangent, as indicated by the dotted

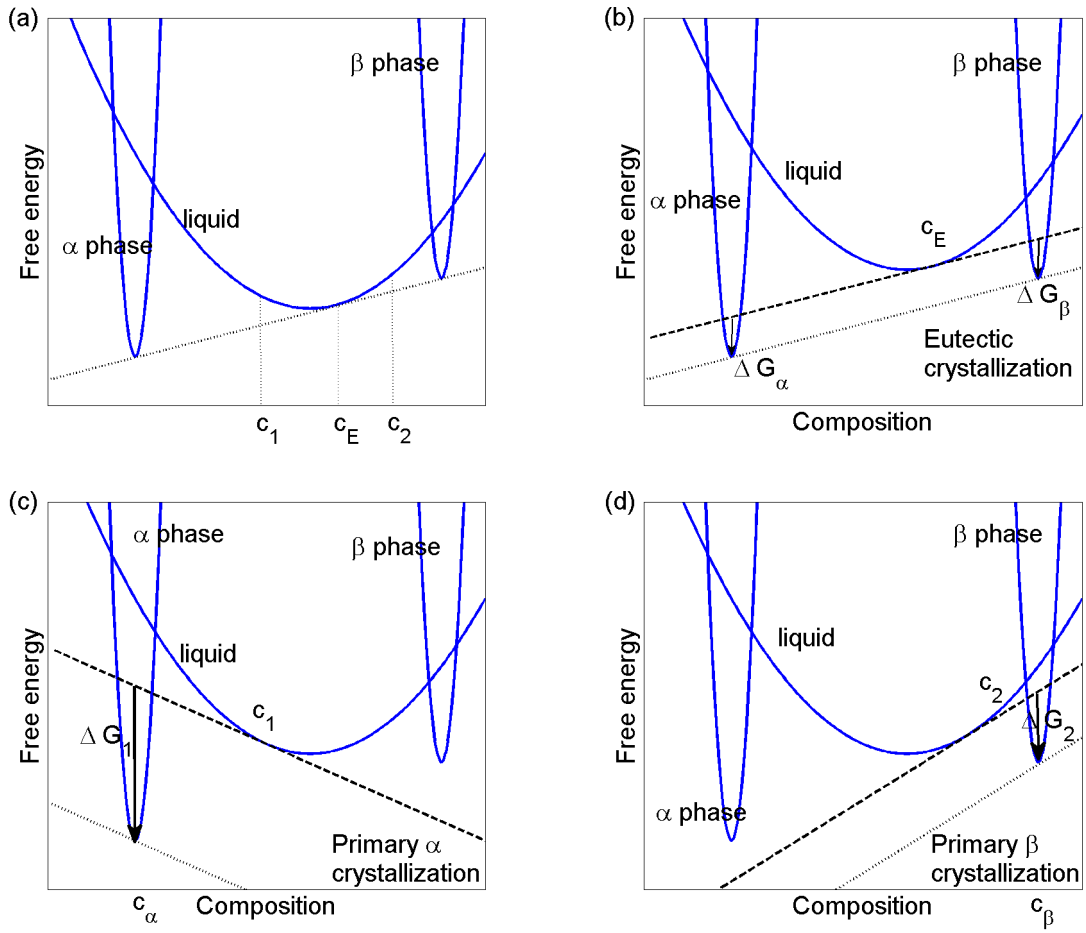

Figure 2.6: Gibbs free energy of various phases on composition

line. During eutectic crystallization, there is no concentration difference across the reaction front, i.e., between the crystalline phase and the amorphous matrix. But at the reaction front where the crystalline phases emerge, the two components have to separate into two phases of α and β. Therefore eutectic crystallization usually takes more time with higher diffusion barrier and sometimes it is not the major crystallization behavior.

If the concentration is hypoeutectic c_1, as shown in panel (c), α will be the dominant crystalline phase. During the reaction, the amorphous phase state will be enriched in one element towards the direction of hypereutectic composition, until it reaches the metastable equilibrium: the mix of α phase and the liquid phase. The mixed metastable state is indicated by the dashed line, which is the tangent line at composition c_1. The liquid at c_1 undergoes composition fluctuation to become a mixture of composition c_α and c_1'. c_1' still remains in the liquid state, while being right to the original nominal composition c_1. To be more accurate, c_α is the most likely composition for solid nucleation, since it gives the largest driving force between the liquid and solid state. This intuitively

obvious assumption is used because of its simplicity. Further justification based on a more rigorous calculation can be found in Thompson and Spaepen's paper [22]. The part with composition c_α will have a driving force ΔG_1 to become crystalline α state. The primary α phase formed may act as the preferred nucleation site for the following crystallization of the amorphous matrix, which further favors the primary α crystallization. Meanwhile, since the metastable line (dashed line) is below β phase, there is no driving force for β crystal to precipitate out of the liquid.

Similarly, if the concentration is at c_2 which is hypereutectic, it is less likely that theres still α crystallization, since the tangent at c_2 lies below α state, as shown in panel (d). Following the same rationale we may indicate the driving force for β crystallization ΔG_2 as the arrow here.

If this is plotted on phase diagram, it may be illustrated by Figure 2.7. The left panel is a schematic binary phase diagram. The blue dashed curves depict the undercooling region. The two undercooling curves for hypo- and hyper-eutectic parts have different dependence on concentration, because α phase and β phase have different driving forces. Specifically in panels (c) and (d) of Figure 2.6, $\Delta G_1 > \Delta G_2$, which makes α phase easier to crystallize, thus allows a smaller undercooling region. Therefore, the undercooling curve for α phase is closer to the liquidus curve. For glass forming, it is not the deepest undercooling that determines, but the shallowest undercooling, i.e., the easiest crystallization gives the weakest glass formation. At hypoeutectic, β allows a much deeper undercooling than α phase, thus, α is the key decision maker for glass forming. Same for the hypereutectic part. Near c_E, α and β phases are competing with each other to make a larger impact on the system's crystallization. At the crossover of the two curves, the contribution to crystallization (or, the limit to glass forming) of α and β phases are essentially equal. This is the point where the whole system has the largest undercooling, or, the best potential glass forming ability. Note that this crossover concentration c^* is usually different from the system's eutectic c_E, unless the α and β crystallization curves are totally symmetrical. Panel (b) is a real case of Fe-B phase diagram. The shaded area shows the glass forming range, which corresponds to a finite undercooling. The undercooling curve on the left corresponds to α-Fe phase, and it is much steeper than the curve on the right which is for Fe_3B or Fe_2B.

We may further relate the undercooling to the glass forming ability, which can be measured directly by experiments. When a molten sample is quenched in water, its outer surface is nearly isothermal to the surrounding water temperature while its centerline is gradually cooling down from the melting point. Temperature distribution within the sample is governed by Fourier's equation

$$\frac{\partial T}{\partial t} - \kappa \bigtriangledown^2 T = 0 \tag{2.5}$$

The time-dependent part of its solution has the exponential decay form $exp(-n^2\pi^2\kappa t/D^2)$, where n is an integer to denote Fourier series, κ is thermal diffusivity and D is the characteristic sample

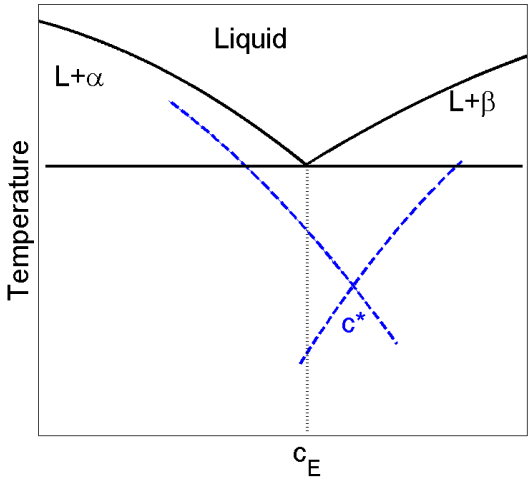

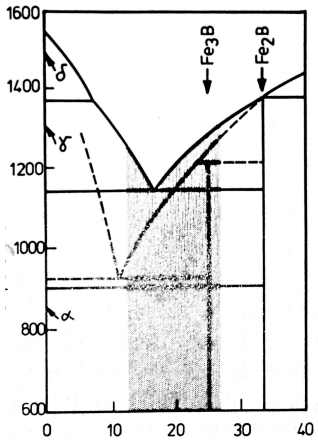

Figure 2.7: Undercooling near eutectic composition

size. $\sqrt{\kappa t}$ has the dimension of length and it actually is a characteristic length for the sample which determines the temperature evolution. When $\sqrt{\kappa t}$ is about the value of D, the temperature of the sample rod's center has dropped below e^{-1} of its initial value towards to surrounding environment's temperature. Effectively we can assume that when $\sqrt{\kappa t}$ is comparable to the sample size, it is reasonable to consider the centerline temperature as close enough to boundary condition temperature, i.e.

$$\sqrt{\kappa t} \sim D \tag{2.6}$$

Then the characteristic time scale for rapid cooling is

$$t = \frac{D^2}{\kappa} \tag{2.7}$$

The cooling rate is inversely proportional to time scale, as is the nucleation rate. From nucleation theory we know that the nucleation rate is given by

$$\dot{\nu} = N * f \tag{2.8}$$

where f is a kinetic factor which describes diffusion and can be expressed in the liquid's viscosity. N is the the average number of clusters that reach the critical size to serve as crystallization nuclei:

$$N = N_0 \cdot exp(-\frac{\Delta G_{barrier}}{k_B T}) \tag{2.9}$$

$\Delta G_{barrier}$ is the energy barrier to crystallize from liquid. It is different from the thermodynamic

driving force ΔG_1 or ΔG_2. Yet $\Delta G_{barrier}$ can be expressed by the driving force ΔG

$$\Delta G_{barrier} = constant \cdot \frac{\sigma^3 V_m^2}{\Delta G^2} \tag{2.10}$$

where σ is the interfacial energy between liquid and crystal, V_m is the molar volume. For a spherical nucleus model, the constant equals $16\pi/3$. Then the nucleation rate is inversely proportional to time scale as

$$\dot{\nu} \sim \frac{\kappa}{D^2} \tag{2.11}$$

The nucleation rate has two contributing factors: kinetic and thermodynamic, and the thermodynamic term can be expressed in driving force ΔG. According to Eqns. (2.8) - (2.10)

$$\dot{\nu} = f N_0 exp(-\frac{A}{\Delta G^2}) \sim \frac{1}{D^2} \tag{2.12}$$

where A is a coefficient $\sim \sigma^3 {V_m}^2/k_B T$. We have dropped the thermodiffusivity here since it is a material property for a given alloy. If we neglect the variation in the kinetic term f and assume that when the composition deviates from eutectic but is still close to it, the composition change only affects the driving force ΔG, then

$$\begin{aligned} D &= D_0 exp(\frac{A}{2\Delta G^2}) \\ &= D_0 exp(\frac{A}{2(\Delta G(\delta c))^2}) \end{aligned} \tag{2.13}$$

Eqn. (2.15) gives an explicit expression of glass forming ability's dependence on composition. If only thermodynamic term is taken into account, the glass forming ability is changing exponentially with composition variation from eutectic point. However, this claim has two risks. First, the evaluation of driving force is a bit vague here. From the previous discussion, the exact solid composition is not for sure, although the most likely one can be found by parallel tangent. Yet we can solve the exponential form by fitting parameters.

Another risk, however, is not to be neglected. In the previous discussion we have neglected the kinetic part. But actually it may play a very crucial role here. When the alloy's composition shifts from eutectic, not only the thermodynamic factor, but also its viscosity, or kinetic factor, changes accordingly. A more detailed and comprehensive discussion on their influences on glass forming ability is in Chapter 3.

2.3.2 Further interpretation of the optimization of Fe-based system

Figure 2.8 presents the glass forming ability dependence on Si and B concentrations for the FeCoSiBP alloying system. Panel (a) is a 3D colormap while panel (b) is a 2D projection from (a). Warm colors (red, orange, etc.) denote larger glass forming ability while cool colors (blue, green, etc.) denote smaller glass forming ability. The best glass former in this Fe-based metal-metalloid system can reach 3 mm in quartz tube by water quenching. Here Si and B concentrations are chosen as natural coordinates. However, this "GFA peak" is in no way isotropical or symmetrical. Along one diagonal direction, the altitude of the "GFA mountain" changes very slowly; while in another diagonal direction, it drops much more drastically. According to our analysis in the previous section, a fast optimization approach would like to follow the steepest descent, or the direction with most sensitivity to concentration. Along the (Si-B) direction, the variation of glass forming ability is relatively mild. Along the (Si+B) direction, the variation of glass forming ability is relatively steep. Along this direction, the total (Si+B) concentration, or, identically P concentration, is fixed; however, the difference, or ratio, between Si and B, i.e., Si-B or Si/B, is varying. This may indicate that the primary crystallization along this direction is not associated much with total (Si+B) concentration or P concentration, but indeed associated with Si-B concentration or Si/B ratio. Moving along this direction is essentially optimizing coordinate u with the other three coordinates fixed. Another steep direction would be the vertical one, i.e., B concentration varies while Si is fixed. With a minor change of about 2 % B, the glass forming ability boosts from 1 mm to 3 mm. The high sensitivity on B concentration may indicate that there are major crystallization phases associated with B with steep liquidus projection. There is an implication that we are still missing the real optimal glass forming ability composition, since in experiments we vary composition by step of 0.5 %. This footstep may still be too large so that the true optimum is still hiding in this very coarse fitting surface. Ongoing work from Na et al. [16] has shown that an appropriate footstep may be as small as 0.2 or 0.25 %. It is interesting to note that the other direction (Si-B) presents an opposite trend. This appears to be the "ridge" of the GFA landscape where the change is very slow. Along this direction, the difference between (Si-B) is fixed while (Si+B) is changing, indicating that the influence of (Si+B) concentration, or P concentration, is not very big. Therefore, the initial natural coordinate v (which represents P concentration) may not be the best choice to optimize the glass forming ability. A better set of notation for the metalloid part would be $\mathrm{Si}_{u'+v'}\mathrm{B}_{v'}\mathrm{P}_{1-u'-2v'}$, with u': difference between Si and B; v': B content. Compared to the initial natural coordinates $\mathrm{Si}_{\frac{1+u-v}{2}}\mathrm{B}_{\frac{1-u-v}{2}}\mathrm{P}_{v}$ there is a relationship

$$\begin{aligned} u' &= u \\ v' &= \frac{1-u-v}{2} \end{aligned} \tag{2.14}$$

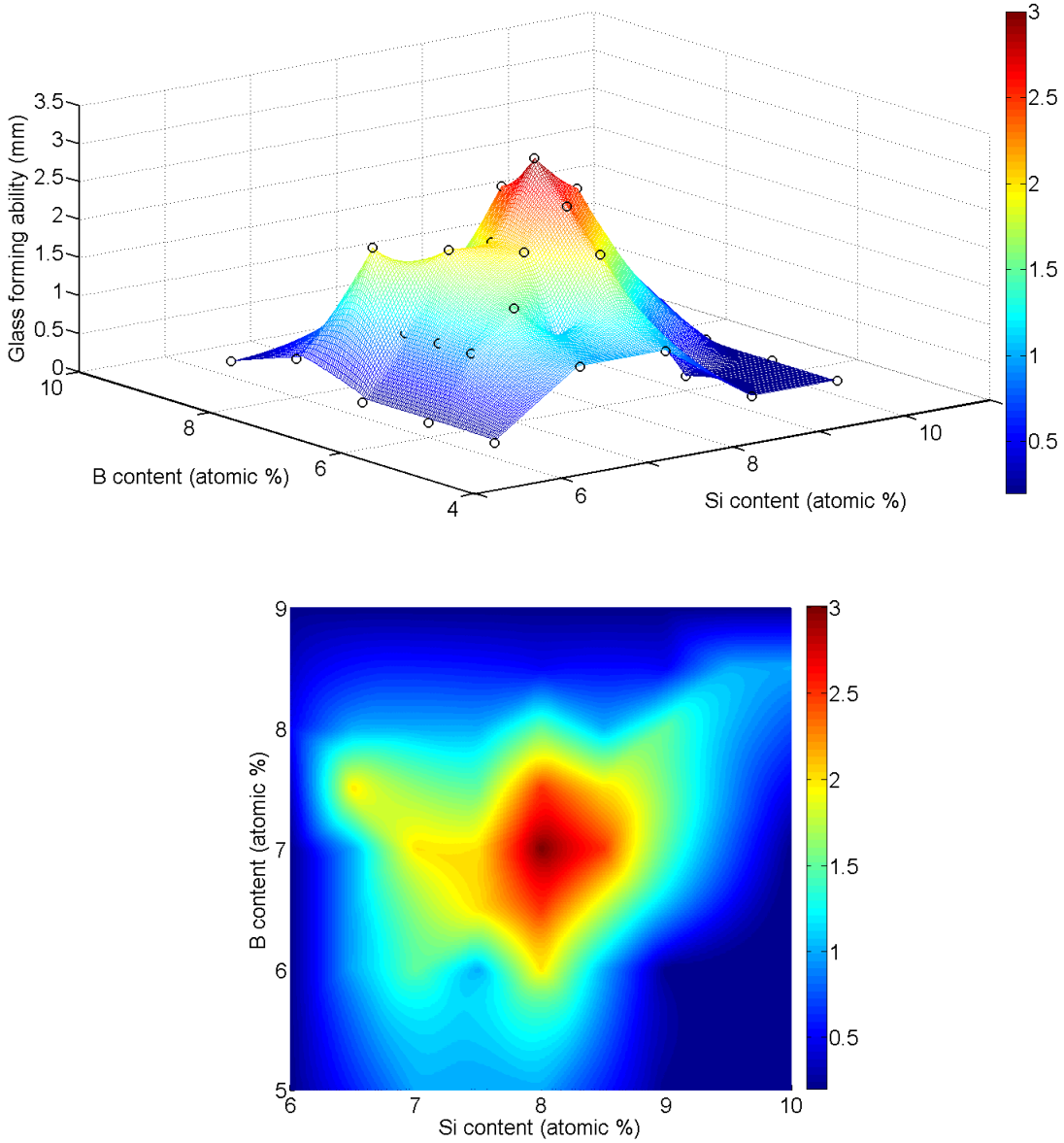

Figure 2.8: Glass forming ability dependence on metalloid contents. (a) The 3D colormap is fitted with experimental data (black circles). (b) 2D colormap is projected from (a).

Essentially, the new coordinates u' and v' will give the steepest directions along which is the fastest path to find the GFA peak. These steepest directions are associated with major crystallization phases. Sometimes it is difficult to know the crystalline phases ex ante. A path along the original u and v will still converge to the peak although in a slower way.

Figure 2.9 illustrates the difference in optimizing speed between different coordinate selection. This is a ternary phase diagram of Co-Si-B based on the reprint of Figure 2.3. This 3-component system has 2 degrees of freedom. It may seem natural to choose two components as independent variables, e.g., $Co_xB_ySi_{100-x-y}$. However, with this choice we may not be following the best way to get to the eutectic. Assume in the first round we are fixed at $x = 65$ (point A) and would like to optimize y. $x = 65$ corresponds to the straight line for fixed Co content. The optimization for y (at $x = 65$) gets B content to be around 20 % (point B). Then we fix $y = 20$ and again search for x along fixed B content. We get a little improvement with $x = 68$ (point C). Then little by little we move towards the eutectic along this jaggered route in green. However, a better choice of the independent variables will include the relative ratio of the metalloids, e.g., $Co_x(B_zSi_{1-z})_{100-x}$, with z denoting the ratio of % B/% total metalloid. Then we start again from A and the optimization of z get us to $z = 0.8$ (point B). When fixing z to optimize x again, we are moving close to the liquidus projection. Therefore the optimization route in red is very fast and in only two steps it almost reaches eutectic. For systems with more components, it could offer more convenience if we can cleverly choose the independent variables to leverage the liquidus curves.

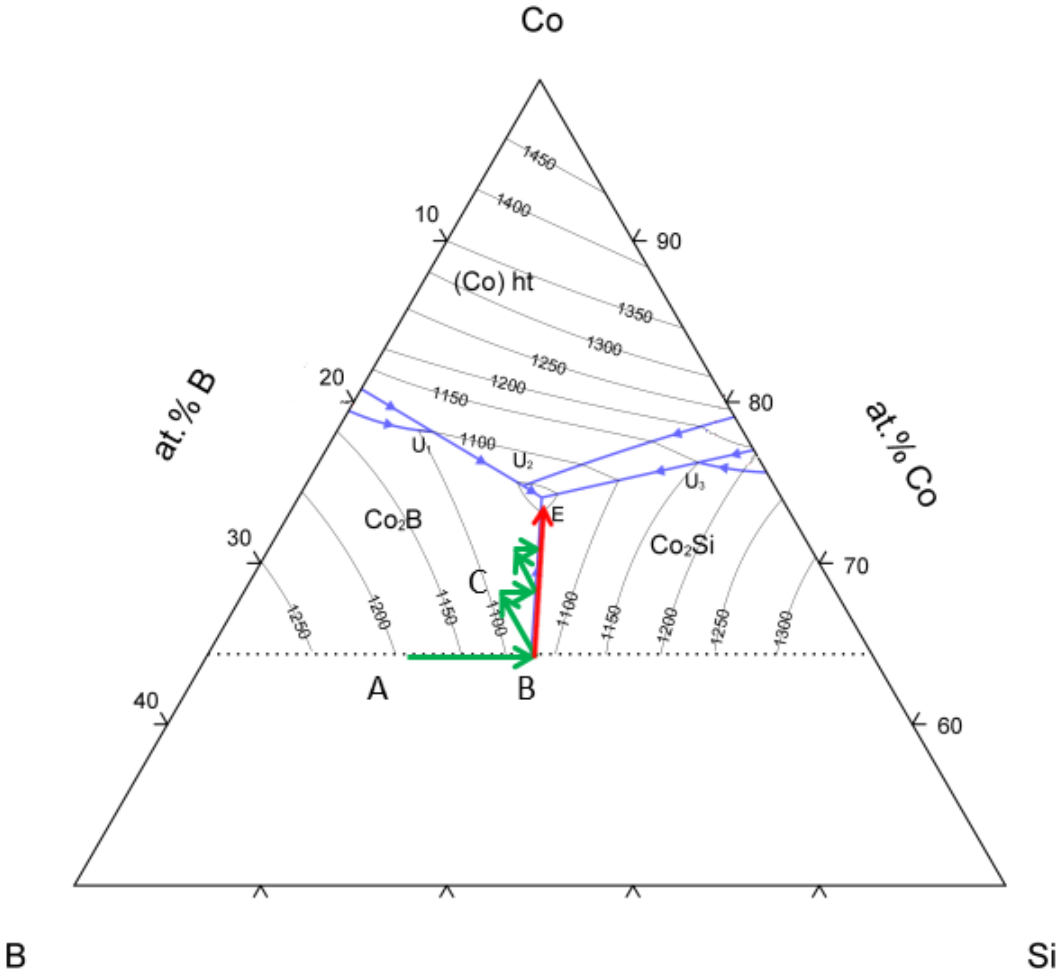

Figure 2.9: Different optimization routes. Green: Co and B contents are chosen as independent variables. Red: Co content and B/Si ratio are chosen as independent variables.

Chapter 3

Thermostability and structural analysis

In this chapter, the thermodynamics of the pentiary FeCoSiBP alloying system are extensively examined by differential scanning calorimetry, X-ray diffractometer and scanning electronic microscopy. The glass transition, crystallization and melting behavior are reported in this chapter. The glass forming ability of this system reaches as much as 3 mm. We will discuss the effects of reduced glass transition temperature and fragility on glass forming ability.

Of greater significance is that our research reveals the influence of oxide inclusions on glass forming ability. Possible explanations are presented in this chapter, as well as recommendations for experimental optimization. In Chapter 2 we have discussed the crystallization behavior of metallic glasses. Here we will make further investigations into the influence of oxidation. Oxidation behavior is of significant importance to metallic glasses, on one hand because oxides may serve as nuclei for crystallization and therefore deteriorate the GFA and mechanical properties. On the other hand, however, nanocrystalline alloys may have their own advantage in biological and magnetic applications [23]. Oxidation is suppresed in laboratory processing by providing high-purity vacuum/Ar environment. It may become a more important issue in industrial processing when large scale high vacuum is more difficult. Our study reveals a deeper understanding of oxidation behavior of metallic glasses and its influence on structure and thermostability. Moreover, we identify several approaches to take advantage of oxidation.

3.1 Thermodynamics of nucleation

Here we propose a model based on nucleation theory in order to understand the influence of various factors on glass forming ability. The overall crystal nucleation rate has the form

$$\dot{\nu} \sim \eta^{-1} \cdot exp(-\frac{\Delta G}{k_B T}) \tag{3.1}$$

This nucleation rate is function of material composition and temperature, provided that all discussion is under standard pressure condition. The first term in the above expression is a kinetic one, which indicates the rate of atomic configurations being sampled in a liquid. It is proportional to the liquid fluidity, or inverse viscosity. Intuitively, this is the hopping rate among configurational states. The faster the hopping rate, the greater the chance that the liquid falls into the more stable crystalline state. The second term is a thermodynamic one, where ΔG is the energy barrier for crystallization from liquid. The characteristic time t for nucleation is the inverse of the nucleation rate. Its natural logarithm is thus the sum of the kinetic term and the dynamic term

$$ln(t) = -ln(\dot{\nu}) = ln(\eta) + \frac{\Delta G}{k_B T} \tag{3.2}$$

Note that both η and ΔG depend on composition and temperature. Given certain composition, if we plot $ln(t)$ on horizontal axis and temperature T on vertical axis, we obtain the well-known Time-Temperature-Transformation, or TTT-diagram for crystal nucleation. As temperature drops below its melting point T_{liq}, there is a competition between these two terms: viscosity goes up but $\Delta G/k_B T$ goes down. Therefore, when temperature is below T_{liq} but still close to T_{liq}, the kinetic term, i.e., viscosity, is the key determinator; when temperature gets very low to near T_g, the thermodynamic term, i.e., the magnitude of energy barrier for sampling, is more important to influence the time to crystallization. Between T_{liq} and T_g, there is a temperature where their sum, $ln(t)$, is minimized. This is the "nose" on the TTT-diagram. This minimum time scale is the shortest time allowed for undercooling without encountering nucleation and therefore is the bottleneck to determine critical cooling rate.

Viscosity of the liquid is described as a function of temperature [24]

$$\eta(T) = \eta_\infty \cdot exp[\frac{W_g}{k_B T} \cdot exp(2n(1 - \frac{T}{T_g}))] \tag{3.3}$$

where $W_g = k_B T_g \, ln(\eta_g/\eta_\infty)$. $\eta_g = 10^{12} Pa \cdot s$, and it is the Newtonian viscosity limit at T_g. η_∞ constitutes the limit of viscosity at high temperature and can be well approximated by the Planck limit. For various amorphous metals η_∞ is around $10^{-3} \sim 10^{-4} Pa \cdot s$. n is a parameter of liquid fragility which can be obtained by fitting experimental viscosity data. Then the first term in Eqn. (3.2) becomes

$$ln(\eta) = ln(\eta_\infty) + ln(\frac{\eta_g}{\eta_\infty}) \cdot \frac{T_g}{T} exp(2n(1 - \frac{T}{T_g})) \tag{3.4}$$

Now we take a look at the thermodynamic term. The nucleation barrier ΔG has the form of

$$\Delta G \sim \frac{\sigma_{XL}^3}{\Delta g_{XL}^2} \tag{3.5}$$

If we assume classical spherical nucleus model, the coefficient is calculated to be $16\pi V_m^2/3$, where V_m is molar volume. σ_{XL} is the liquid/crystal interfacial free energy. Based on Spaepen and Turnbull's monoatomic layer model, it is about 0.7 to 0.8 times the heat of fusion per atomic layer

$$\sigma_{XL} = 0.7 \sim 0.8\Delta h_F \tag{3.6}$$

Δg_{XL} is the difference between liquid and crystal free energy per unit volume, or the "driving force." In this chapter's discussion we do not distinguish between physical quantities per unit volume and per unit mol. To be more precise, the variance between C_P and C_V should be taken into account as higher order adjustment. The Turnbull model uses straight lines to approximate the temperature dependence of free energy. However, there is another $1/T$ term adjustment which fits well with experiment.

At melting, there's no Gibbs free energy difference between solid and liquid, which is exactly the definition of phase transition equilibrium when taking temperature and pressure as natural variables. Yet there is heat of fusion to describe the difference in enthalpy, and therefore entropy of fusion.

$$\begin{aligned}
\Delta g_{XL}(T) &= \Delta h_{XL}(T) - T\Delta s_{XL}(T) && (3.7)\\
\Delta g_{XL}(T_{liq}) &= 0 && (3.8)\\
\Delta h_{XL}(T_{liq}) &= \Delta h_F && (3.9)\\
\Delta s_{XL}(T_{liq}) &= \frac{\Delta h_{XL}(T_{liq})}{T_{liq}} = \frac{\Delta h_F}{T_{liq}} && (3.10)
\end{aligned}$$

The enthalpy change Δh_F is a measure of the actual energy that is freed as heat. The reaction is exothermic when Δh_F is negative. When temperature drops below the melting point, at constant pressure, $dg = vdP - sdT = -sdT$,

$$g(T) = \int -s(T)dT = g(T_{liq}) - \int_{T_{liq}}^{T} s(T)dT \tag{3.11}$$

This applies to both liquid state and crystal state. Hence, the free energy difference at temperature below melting point is derived as

$$\begin{aligned}
g_X(T) &= g_X(T_{liq}) - \int_{T_{liq}}^{T} s_X(T)dT\\
g_L(T) &= g_L(T_{liq}) - \int_{T_{liq}}^{T} s_L(T)dT\\
\Delta g_{XL} &= -\int_{T_{liq}}^{T} \Delta s_{XL}(T)dT && (3.12)
\end{aligned}$$

Dulong-Petit law gives the classical heat capacity of a solid crystal to be $c_V = 3R$ and $c_P = 3R + aT$.

The heat capacity of liquid is described by [25]

$$c_P^{liq} = 3R + aT + bT^{-2} \tag{3.13}$$

The aT term is the electronic and anharmonic contribution, as in solids. The term bT^{-2} is the configurational contribution, which is based on the assumption that density of configurational states is a Gaussian distribution. This usually fits well with experimental data near high temperature, i.e., around melting point. The deviation may not be neglected when temperature drops, especially on reaching glass transition. The heat capacity for a crystal contains only the first two terms. So the difference from a solid (either crystal or glass) is the third T^{-2} term.

The temperature-dependent entropy difference is the integral of heat capacity

$$s(T) = s(T_{liq}) + \int_{T_{liq}}^{T} \frac{c_P}{T} dT \tag{3.14}$$

Therefore, the entropy difference between liquid and crystal is

$$\begin{aligned} \Delta s_{XL}(T) &= \Delta s_{XL}(T_{liq}) + \int_{T_{liq}}^{T} \frac{\Delta c_{P,XL}}{T} dT \\ &= -\Delta s_F - \int_{T_{liq}}^{T} \frac{b}{T^3} dT \\ &= -\Delta s_F + \frac{b}{2}(\frac{1}{T^2} - \frac{1}{T_{liq}^2}) \end{aligned} \tag{3.15}$$

Note that the substrate "XL" refers to $s_X - s_L$ which is actually a negative value. Δs_F indicates the entropy of fusion which is generally positive, therefore there is a sign change in the second equation here. Putting this back to Eqn. (3.12) we get

$$\begin{aligned} \Delta g_{XL}(T) &= -\int_{T_{liq}}^{T} \Delta s_{XL}(T) dT \\ &= -\Delta s_F (T - T_{liq}) + \frac{b}{2} \frac{(T - T_{liq})^2}{T T_{liq}^2} \end{aligned} \tag{3.16}$$

In order to compare materials with different melting temperature, we introduce a dimensionless temperature scale

$$T^* = T/T_{liq} \tag{3.17}$$

Note that the temperature range we are interested in is $T^* \in [0, 1]$. When T^* is close to 1, we may

rearrange the above expression in series of $(1 - T^*)$.

$$\begin{aligned} \Delta g_{XL}(T) &= -\Delta s_F T_{liq}(1-T^*) + \frac{b}{2}\frac{1}{T}(1-T^*)^2 \\ &= -\Delta s_F T_{liq}(1-T^*) + \frac{b}{2T_{liq}}\frac{(1-T^*)^2}{T^*} \\ &= -\Delta s_F T_{liq}(1-T^*) + \frac{\Delta c_{P,F} T_{liq}}{2}\frac{(1-T^*)^2}{T^*} \end{aligned} \tag{3.18}$$

The last equation comes from that $\Delta c_{P,F} = -c_{P,X} + c_{P,L} = b/T_{liq}^2$, where $\Delta c_{P,F}$ is a positive value for the magnitude of heat capacity change. Note that the first term here is just Turnbull approximation. Figure 3.1 illustrates the straight-line Turnbull approximation and the adjustment with the $(1 - T^*)^2/T^*$ term resulting from the heat capacity $1/T^2$ term.

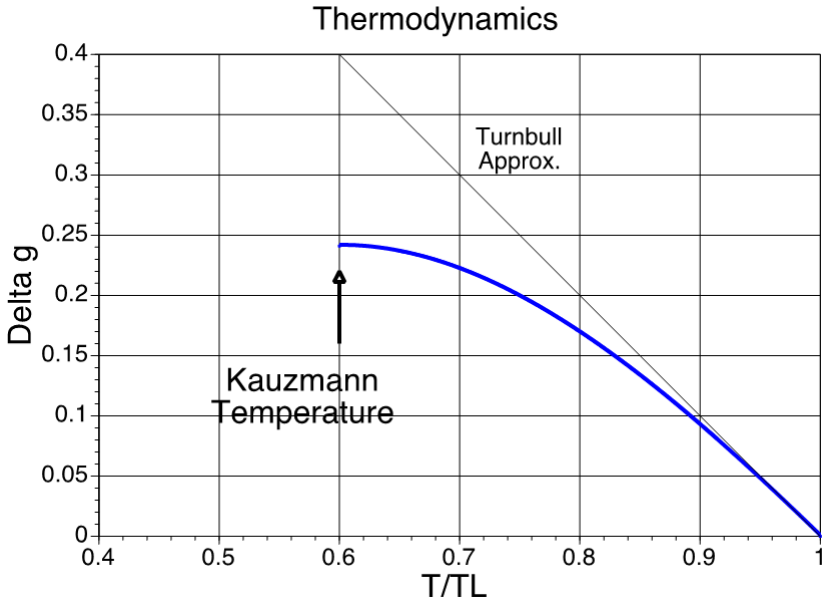

Figure 3.1: Gibbs free energy difference between crystal and liquid states: Turnbull straightline model and adjustment with $1/T^2$ heat capacity term

When the temperature decreases, the entropy difference between supercooled liquid and crystal also decreases towards zero as in Eqn. (3.15). It reaches zero at a temperature called the Kauzmann temperature T_K. From Eqn. (3.15) it can be derived as

$$T_K = T_{liq}/\sqrt{1 + \frac{2\Delta s_F}{\Delta c_{P,F}}} \tag{3.19}$$

The Kauzmann paradox comes from the situation that if a liquid could be undercooled to T_K, it would have an entropy lower than crystal, which is a paradoxial situation. One resolution to this is that a phase transition, glass transition, happens before that, so the Kauzmann temperature

can never be really reached. A deeper understanding of the above derivation is from the basic assumption that there is a $1/T^2$ term in the liquid heat capacity. However, this is only true for high temperature limit. The $1/T^2$ term comes from the Gaussian distribution assumption for the density of configurational states. The Gaussian model is not valid when temperature is low since it has no lower bound on the ground state energy. The case in reality is that there is indeed a lower bound for liquid energy distribution, which is the ground state energy level of crystal. Johnson et al. [26] has brought up another model which describes the whole energy spectrum. At high temperature limit it is Gaussian distribution asymptotically. At low temperature limit it has the form of $xlnx + (1-x)ln(1-x)$, which has a clear stopping point of x=0.

Recall Eqn. (3.2) . The natural logarithm of time to nucleation is

$$\begin{aligned} ln(t) = ln(\eta_\infty) + ln(\frac{\eta_g}{\eta_\infty}) \cdot \frac{T_g}{T_{liq}} \cdot \frac{1}{T^*} exp(2n(1 - \frac{T^*}{T_g/T_{liq}})) \\ + \frac{16\pi {\sigma_{XL}}^3}{3k_B T_{liq} T^*} \cdot \frac{1}{[\Delta s_F T_{liq}(1-T^*) - \frac{T_{liq}}{2}\Delta c_{P,Fusion}(1-T^*)^2]^2} \end{aligned} \tag{3.20}$$

This expression seems to be a bit complicated; however, there is only one independent variable T^*. All other parameters are pre-determined by the sample material and experimental design. The term T_g/T_{liq} is called reduced glass transition temperature T_{rg}. It is one of the widely used indicators for an alloy's glass forming ability. Intuition suggests that when this ratio increases, the interval between T_g and T_l decreases, and the probability of being cooled through this interval without crystallization is enhanced. In many alloying systems, T_g and T_{sol} do not change significantly; however, the liquidus temperature, T_{liq}, may vary a lot. T_{liq} is often relatively small where the composition is near eutectic. Hence, a higher reduced glass transition temperature may yield better glass forming ability.

There have been many studies on the correlation between T_{rg} and glass forming ability. Lin et al. [27] proposed a relationship between the reduced glass transition temperature, the critical cooling rate and the glass forming ability. If we plot temperature versus $ln(time)$ to get the TTT-diagram, there is a minimum time scale t_{nose} which corresponds to the "nose" on TTT diagram. This "nose" can be calculated by taking $\partial ln(t)/\partial T^*$ to be zero in order to get T^*_{nose}. When a molten sample is cooled down from liquidus temperature, only when the cooling rate is fast enough to bypass the "nose" so glass can be made by quenching. The slowest critical cooling rate corresponds to a maximum critical sample size. A good approximation for the critical situation would be: the sample takes time t_{nose} to cool down from $T^* = 1$ (i.e., liquidus temperature) to T^*_{nose}. This critical cooling rate is averaged as

$$R_C = \frac{T_{liq} - T_{nose}}{t_{nose}} = T_{liq}\frac{1 - T^*_{nose}}{t_{nose}} \tag{3.21}$$

The value of $T*_{nose}$ (i.e., the solution of minimizing Eqn. (3.20)) is observed to be very similar for most alloys. Although liquidus temperature does vary according to materials, the variance is normally of order 10% within a certain alloying system. However, t_{nose} varies significantly and often involves differences of orders of magnitude. Hence, roughly speaking,

$$ln(R_C) \sim -ln(t_{nose}) \tag{3.22}$$

Recall that t_{nose} depends on reduced glass transition temperature T_{rg}. Lin et al. [27] presented the relationship between $log(R_C)$ and T_{rg}, which is monotonically decreasing. However, the data is relatively scattered; no strong correlation can be drawn from the data. It is still controversial to simply claim a function between GFA and the Turnbull parameter. Eqn (3.20) shows that the dependence on T_{rg} is very complicated. There are three major parameters which are material properties: T_{rg}, n and σ. The parameter n characterizes the rheology of the liquid. σ describes the interface between liquid and crystal, and therefore is dependent on the specific crystal phase, even when cooling down from the same liquid. This complicated relationship may smear our understanding of what are the most important factors contributing to GFA. In the next section we will conduct a systematic analysis on glass forming ability for a novel series of iron-based bulk metallic glasses.

3.2 Thermostability of the Fe-Co-Si-B-P alloying system

Table 3.1 lists a few novel compositions of the FeCoSiBP alloying system with their glass transition temperature (T_g), crystallization temperature (T_x), solidus temperature (T_{sol}) of melting onset and liquidus temperature (T_{liq}) of melting offset, obtained by DSC at heating rate of 20 K/min. Samples in Table 3.1 were all cast at the same condition of 1150 °C in quartz capillary with estimated quartz wall thickness to be 0.1-0.2mm.

T_g of some samples are not available in Table 3.1 due to the proximity to the Curie temperature. Figure 3.2 illustrates a typical specific heat curve obtained by DSC.

The glass transition is an endothermic event characterized as a jump in heat capacity before the crystallization, which may consist of single or multiple exothermic heat release events. T_{sol} is the onset of the melting of the crystalline phases, while T_{liq} is where all the crystalline phases are fully melted. For ferromagnetic glasses, the Curie temperature T_C can be detected as small cusp on the DSC curve when it is below T_g, because it is second order transition and has a "λ" shape anomaly near the critical point. When T_g and T_C are too close (<20K difference), T_g can not be clearly identified. In this situation, we determine T_x as the inflection point: the interception of two slopes before and after it. For this family of alloys, T_g is similarly determined as the inflection point, where the first-order derivative of enthalpy change ΔH is minimum or second-order derivative of ΔH is

Alloy composition	GFA	T_C(°C)	T_g(°C)	T_x(°C)	T_{sol}(°C)	T_{liq}(°C)	ΔT	T_{rg}
$Fe_{19}Co_{57}Si_{10}B_{11}P_3$	0.9 mm	487	499	534	942	1058	35	0.580
$Fe_{19}Co_{58}Si_{9.7}B_{8.5}P_{4.6}$	1.0 mm	492	505	521	945	1009	16	0.607
$Fe_{23}Co_{54}Si_{9.7}B_{8.5}P_{4.6}$	1.0 mm	500	NA	518	944	1014	NA	NA
$Fe_{20}Co_{57}Si_{8.5}B_{7.5}P_7$	0.9 mm	472	496	524	945	979	28	0.614
$Fe_{30}Co_{47}Si_{8.5}B_{7.5}P_7$	1.2 mm	493	507	527	942	989	20	0.618
$Fe_{40}Co_{37}Si_{8.5}B_{7.5}P_7$	1.1 mm	495	508	528	960	1007	20	0.610
$Fe_{50}Co_{27}Si_{8.5}B_{7.5}P_7$	2.1 mm	483	499	527	972	1020	28	0.598
$Fe_{55}Co_{22}Si_{8.5}B_{7.5}P_7$	2.1 mm	489	NA	520	980	1056	NA	NA
$Fe_{60}Co_{17}Si_{9.5}B_{8.5}P_5$	1.6 mm	480	499	525	985	1071	26	0.574
$Fe_{60}Co_{17}Si_9B_8P_6$	2.2 mm	475	500	528	986	1057	28	0.581
$Fe_{60}Co_{17}Si_{8.5}B_{7.5}P_7$	2.2 mm	462	492	525	987	1036	33	0.584
$Fe_{60}Co_{17}Si_8B_7P_8$	3.2 mm	463	499	528	988	1075	29	0.573
$Fe_{60}Co_{17}Si_{7.5}B_{6.5}P_9$	3.2 mm	454	492	523	988	1076	31	0.567
$Fe_{60}Co_{17}Si_7B_6P_{10}$	3.1 mm	450	493	531	990	1066	38	0.572
$Fe_{65}Co_{12}Si_{8.5}B_{7.5}P_7$	1.0 mm	454	483	521	992	1079	38	0.559
$Fe_{70}Co_7Si_{8.5}B_{7.5}P_7$	0.9 mm	437	472	519	1003	1091	47	0.546

Table 3.1: Glass forming ability and key temperatures of novel iron alloys

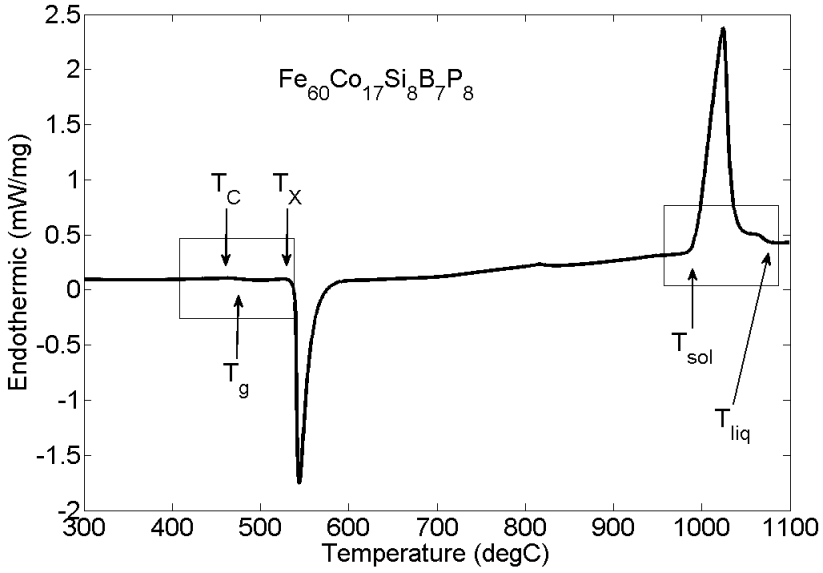

Figure 3.2: DSC curve

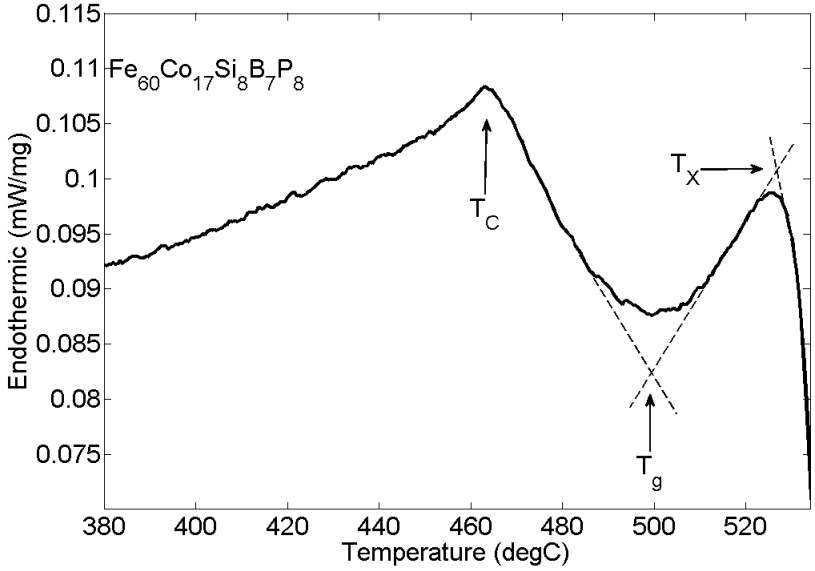

Figure 3.3: Enlarged DSC curve near glass transition

zero. Since DSC curve presents heat flow, with constant heating it also represents the first derivative of enthalpy change with respect to temperature $\partial H/\partial T$ or heat capacity C_P. Thus T_g lies where the DSC curve is minumum, or the slope of DCS curve changes direction, as shown in Figure 3.3. $\Delta T = T_x - T_g$, and it is called the undercooled liquid region.

Shown in Figure 3.4 is the solidus and liquidus temperatures determined by the intercept method. When the composition is very near eutectic, T_{sol} and T_{liq} are very close (e.g., 10-20K difference) with only one melting peak; otherwise there may exist multiple peaks as well as a "shoulder." The "shoulder" and the large difference between T_{sol} and T_{liq} shown in Figure 3.4 indicate that this best glass-forming sample is off-eutectic, which is consistent with discussions in section 2.3.1.

3.3 Impact of reduced glass transition temperature on glass forming ability

The reduced glass transition temperature T_{rg}, first introduced by Turnbull, plays an important role in glass forming alloys. Turnbull proposed a criterion: higher T_{rg} generally infers a better glass forming ability. A quantitative relationship was suggested by Lin and Johnson [27]. The critical cooling rate can be calculated from the critical sample size which can be quenched to the amorphous state. It is obtained by dividing temperature difference from T_{liq} to T_g by the time t_{nose}. For a sample with typical dimension D, the cooling time is determined by solving the Fourier's equation for heat transfer. The solution to Fouriers equation gives critical time scale as Eqn. (2.9) in Chapter

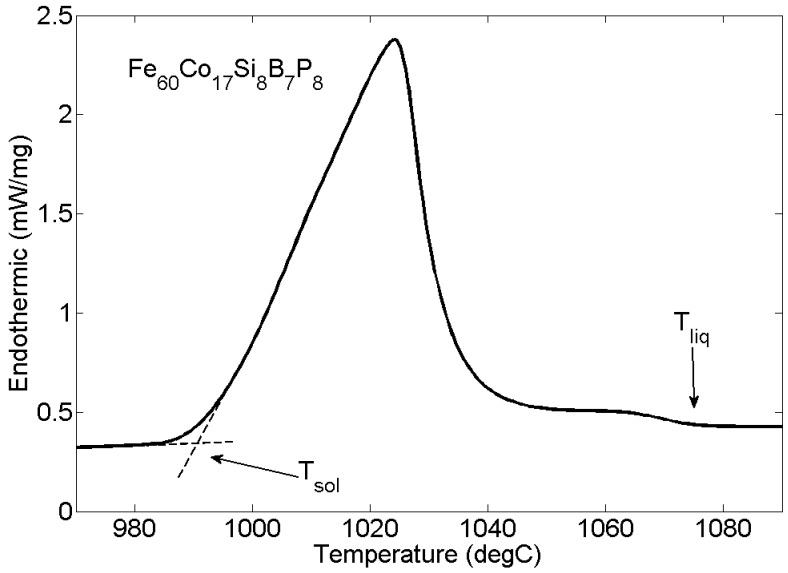

Figure 3.4: Enlarged DSC curve near melting point

2:

$$\tau = \frac{D^2}{\kappa} \tag{3.23}$$

where κ is the thermal diffusivity of the alloy. $\kappa = K/C$, where K is the thermal conductivity and C is the unit volumn heat capacity. Therefore,

$$\begin{aligned} ln(R_C) &= ln(T_{liq} - T_g) - ln(t_{nose}) \\ &= ln(T_{liq} - T_g) + lnK - lnC - 2lnD \end{aligned} \tag{3.24}$$

For this family of iron-based alloys, $T_{liq} - T_g \sim 500K$. For typical molten alloys, $K \sim 0.1W/(cm \cdot s \cdot K)$, and $C \sim 4J/(cm^3 \cdot K)$. We can get a numerical expression of R_C to be

$$ln(R_C)[K/s] = ln25 - 2lnD[cm] \tag{3.25}$$

For rod samples, the critical size is taken as the rod radius.

In Figure 3.5, we present the natural logarithm of critical cooling rate (from critical rod diameter for rods made in capillary or tube) versus reduced glass transition temperature T_{rg}, for two series of alloys. The first series of data (blue circles) are for series $(Fe_xCo_{77-x})Si_{8.5}B_{7.5}P_7$, with x varying from 20 to 70. The second series of data (red diamonds) are for series $(Fe_{60}Co_{17})Si_{12-y/2}B_{11-y/2}P_y$, with y varying from 4 to 11. The black crosses in the left panel are extracted from Lin's data [27], for various families of alloying systems, including from pure Ni (the left most data point), to μm-level

Fe-glass, to *cm*-level vitreloys. It seems that the new data (blue and red) abide this general trend that a relatively high Trg (∼0.6) allows a relatively slow cooling rate, and therefore large GFA. The second panel is a zoom-in view of the rectangular area. Within a certain family of alloys, however, the scattering of data is still large. There is no strong trend between the Turnbull parameter and critical cooling rate. This suggests that T_{rg} alone is not enough to explain the variance of GFA. T_{rg} gives a general guideline yet it is very rough. Other factors also have significant influences that cannot be neglected.

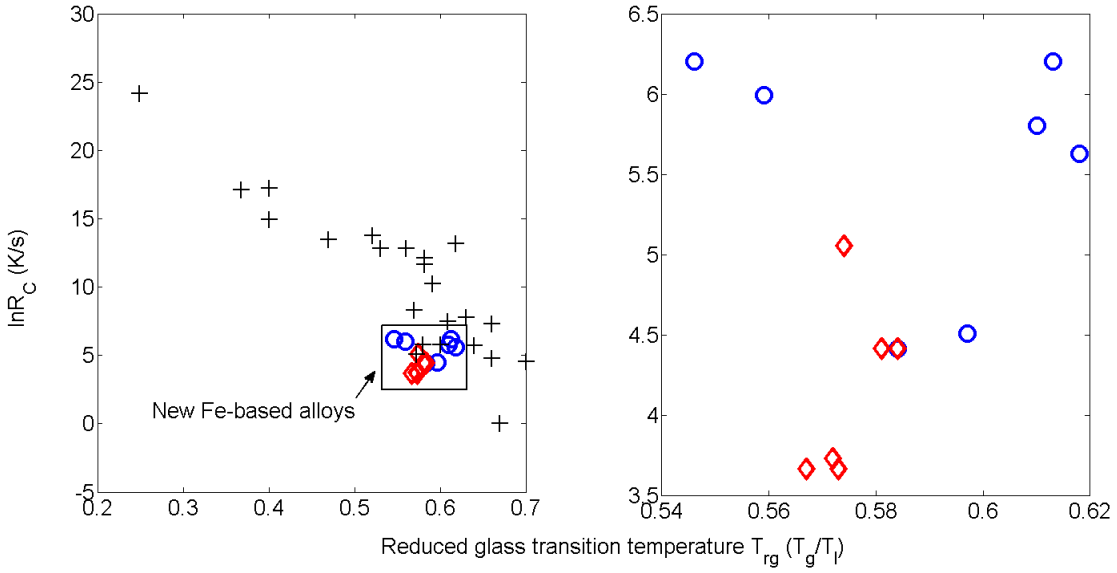

Figure 3.5: Critical cooling rate variation with reduced glass transition temperature

We may take advantage of GFA dependence on composition which could be directly and relatively easy to examine. There are three major contributing factors: T_{rg}, n and σ. In general, we can write:

$$\frac{\partial ln(GFA)}{\partial c} = \frac{\partial ln(GFA)}{\partial T_{rg}}\frac{\partial T_{rg}}{\partial c} + \frac{\partial ln(GFA)}{\partial n}\frac{\partial n}{\partial c} + \frac{\partial ln(GFA)}{\partial \sigma}\frac{\partial \sigma}{\partial c} \tag{3.26}$$

where n is a fragility parameter that describes how strong the liquid is, or how close its temperature dependence follows ideal Arrhenius law. Alongside the reduced glass transition temperature T_{rg} (Turnbull parameter), the fragility plays another important role in determining glass forming ability. Even for glasses with similar compositions, the fragility may vary a lot. Na et al. [28] have researched the FePCB alloys and found that the fragility parameter n ranges from 0.8 to 1.5 while their glass forming ability varies from 4 mm to 16 mm. In next section, we will discuss in further detail the fragility and some key challenges to measure it. Now, σ is the liquid-crystal interface free energy.

We have expressed it as a fraction of the heat of fusion per atomic monolayer. Yet if the interface energy is far from monolayer model, its value may need to be adjusted.

3.4 Impact of fragility on glass forming ability

Fragility of a glass-forming liquid is a measure of the configurational breakdown in the liquid above the glass transition [28]. Angell [29] first introduced a fragility parameter m to describe the relaxation time of the liquid and its deviation from Arrhenius behavior.

$$m = \left.\frac{\partial log < \tau >}{\partial (T_g/T)}\right|_{T=T_g} \tag{3.27}$$

where $< \tau >$ is the average relaxation time and T_g is the glass transition temperature. Typical characterization of fragility, m, is through direct rheology by measuring the change in viscosity of the liquid with respect to temperature around the glass transition.

$$m = \left.\frac{\partial log \eta}{\partial (T_g/T)}\right|_{T=T_g} \tag{3.28}$$

where the onset of glass transition T_g is the temperature at which the viscosity η of the supercooled liquid reaches $10^{12}\ Pa{\cdot}s$. As shown in Figure 3.6, when the liquid closely follows Arrhenius equation, it is said to be "strong" with relatively small m value (20-40). A "fragile" liquid deviates from Arrhenius considerably and is characterized by larger m (60-150). Most of bulk glass-forming liquids fall into the intermediate group with m of 40-60 [30]. It is highly likely that the strong covalent metal/metalloid bonding may induce a "strong" liquid; therefore we expect the FeCoSiBP alloys to have small m values.

The fragility can be obtained through accurate rheological measurements, by fitting viscosity vs temperature data near glass transition according to the relationship

$$\frac{\eta(T)}{\eta_\infty} = exp\{\frac{W_g}{kT} exp[2n(1 - \frac{T}{T_g})]\} \tag{3.29}$$

where η_∞ is the high-temperature limit of viscosity, which is approximated by the Planck limit defined as the ratio between Planck's constant and molar volume, $\eta_\infty \sim 10^3$. W_g is the activation energy barrier at glass transition, given by $k_B T_g ln(\eta_g/\eta_\infty)$. η_g is the viscosity at glass transition, $\eta_g \sim 10^{12}$. Fitting parameter n is related to the fragility, m, via

$$m = (2n+1) log(\frac{\eta_g}{\eta_\infty}) \tag{3.30}$$

Taking $\eta_g \sim 10^{12}$ and $\eta_\infty \sim 10^{-3}$, we have

$$m \approx 30n + 45 \tag{3.31}$$

Na et al. [28] have performed accurate rheological measurements to directly obtain the fragility for several FePCB alloys with this method. The measurement of viscosity by three-point beam bending requires the glass to be fully relaxed to an equilibrium state to obtain the equilibrium liquid viscosity. However, it is very challenging for the new Fe-based alloys because they crystallize before reaching equilibrium. This is due to the extremely small ΔT of $\sim$ 20-30K (see Table 3.1), which allows very little leeway for relaxation of the glass prior to crystallization.

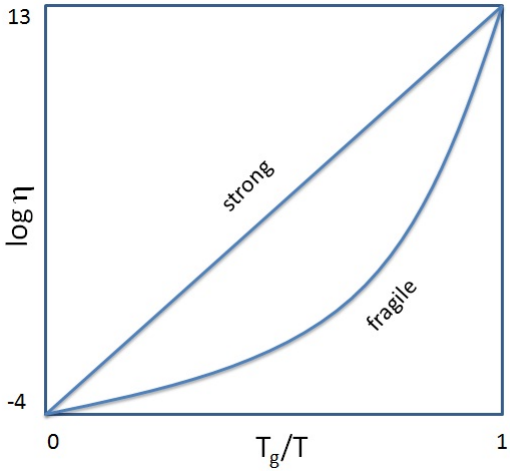

Figure 3.6: Strong and fragile liquids

Other than rheological measurements, calorimetric data can also be used to calculate fragility. The glass transition can be viewed as kinetic freezing of a supercooled liquid, which depends on cooling rate R_C [31]. On the other hand, the relaxation of a glass into supercooled liquid during heating also depends on heating rate R_H [29]. By varying heating rate, the onset of the glass transition is shifted accordingly. When the heating rate increases, the experimental time scale decreases, so the relaxation into liquid is suppressed. This manifests as a delayed glass transition (higher T_g). The influence on T_C is negligible compared to that on T_g. The left panel in Figure 3.7 presents the DSC scans of $Fe_{60}Co_{17}Si_8B_7P_8$ at various heating rates, where 0.333 K/s (20 K/min) is regarded as standard heating rate during most glass transition characterizations, as well as all through this thesis. 0.833 K/s (50 K/min) is the fastest rate achievable for the equipment we have. When the heating rate is slower than 0.167 K/s (10 K/min), the glass transition will completely merge with the Curie temperature (456 °C) and it becomes very hard to get an accurate T_g value. In the right panel, the circles are T_g extracted for each heating rate.

The relationship between the heating rate R_H and T_g can be described by the following Vogel-

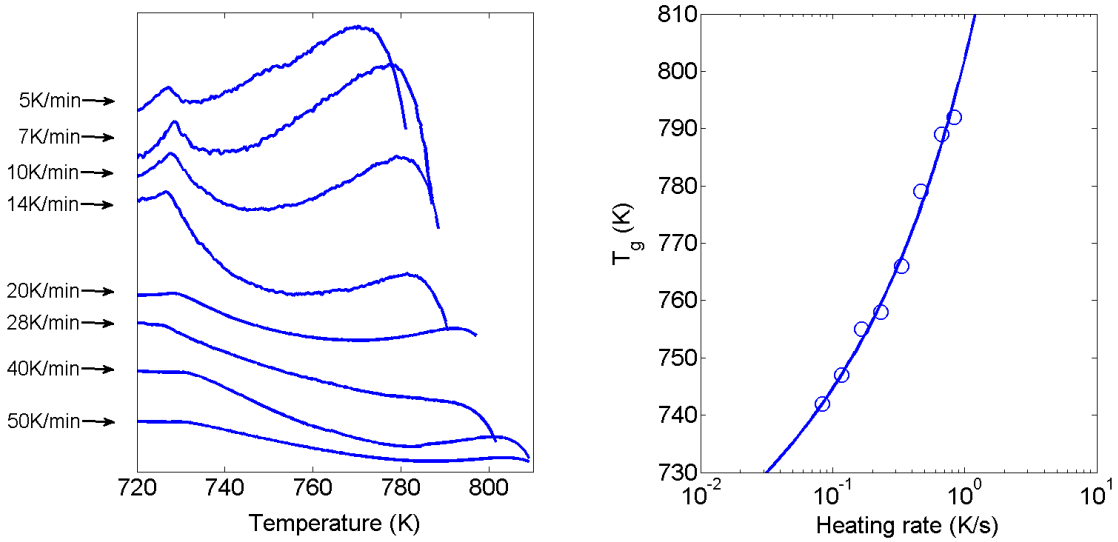

Figure 3.7: T_g with varying heating rate

Fulcher like equation [32, 33]

$$R_H = A \cdot exp\frac{DT_g^0}{T_g^0 - T_g} \tag{3.32}$$

where A, D and T_g^0 are all fitting parameters. T_g^0 has the physical implication of glass transition at the limit of R_H approaches 0, i.e., infinitely slow heating rate. A is a constant with with the dimension of heating rate. D is the strength parameter, which describes how closely the liquid follows on Arrhenius law [34]. In the right panel of Figure 3.7, the blue curve is the fit to experimental data which are circles here. The above relationship can be expressed as

$$ln(R_H) = lnA + \frac{DT_g^0}{T_g^0 - T_g} = \frac{lnA \cdot T_g - (lnA + D)T_g^0}{T_g - T_g^0} \tag{3.33}$$

Using the curve fitting toolbox in Matlab, a rational relationship fitting $y = (p_1 x + p_2)/(x + q_1)$ yiels coefficients with 95 % confidence interval

$$\begin{aligned} p_1 &= 3.572 \; of \; range \; (-0.4222, 7.566) \\ p_2 &= -2865 \; of \; range \; (-6038, 307.5) \\ q_1 &= -655.5 \; of \; range \; (-744.4, -566.7) \end{aligned}$$

Therefore, the fitting parameters in Eqn. (3.32) are calculated as

$$\begin{aligned} T_g^0 &= 655.5K \\ A &= 35.6K/s \\ D &= 0.799 \end{aligned}$$

The fragility is then given by

$$m = \frac{DT_g^0 T_g}{(T_g - T_g^0)^2 ln10} \tag{3.34}$$

Putting in the fitting parameters, we get the fragility for $Fe_{60}Co_{17}Si_8B_7P_8$ to be $m = 14.3$. However, this value is unphysically low. Even though we expect the new Fe-alloys to be strong glass formers (small m), this is still below the reasonable range for any known glasses. The findings of Na et al. [28] and Biswas et al. [34] show that a typical range for Fe-based glasses is from 40 to 70. We believe that this small fragility is due to inability to separate glass relaxation effects from the glass transition itself.

According to the potential energy landscape (PEL) theory of Stillinger and later refinements [35, 36, 37, 24], the glass transition can be identified with the configurational freezing of inherent states. Figure 3.8 is a schematic illustration of the potential energy landscape. It consists of multiple little "basins" which are local minuma with their own distinct depth of potential energy. The alloy is jumping over the "saddles" (or transition states) to sample these basins, until it is cooled enough to freeze the hopping motion. Therefore, the as-cast state is influenced by the sample's thermal history and is determined when it is quenched. The "ideal glass" state, if it exists, must correspond to the inherent structure with the lowest free energy, without any crystalline order nearby. Given the extremely short time of cooling and sampling, it is likely that the as-cast alloy is not at the lowest free energy state (if it ever exists), but in another state with excess free energy compared with a fully relaxed liquid. Isothermal annealing near T_g is often used to relax the glass after it has been cast. Lind et al. [37] have found that the shear modulus G of the alloys shows a strong reversible dependence on annealing temperatures and, thus, on the equilibrium specific configurational potential energy. There, the shear modulus G is directly related to the viscosity and fragility of the liquid.

Angell [38] has proposed another calorimetric method to determine the fragility from the activation energy barrier and proved it to be in good agreement with those determined by viscosity, dielectric relaxation, and other methods. The activation energy barrier is determined by Kissinger analysis by varying heating rate. The dependence on the heating rate R_H of the glass transition

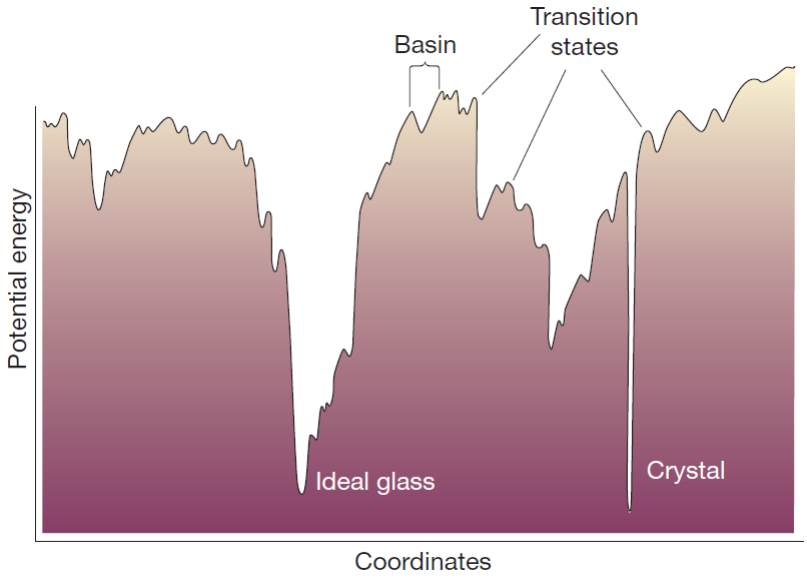

Figure 3.8: Schematic illustration of potential energy landscape (Adapted from [35])

temperature T_g obays an exponential law

$$R_H = R_{H0} exp(-\frac{E_g}{RT_g(R_H)}) \tag{3.35}$$

The m fragility is then derived as

$$m = \frac{E_g}{ln10RT_g} \tag{3.36}$$

Note that this is slightly different from Eqn. (3.32) and is easier to handle from the perspective of data fitting. Therefore, by taking multiple runs of calorimetric characterization at various heating rate, we get multiple pairs of R_H and $T_g(R_H)$ data. Fitting the data pairs $(-\frac{1}{RT_g(R_H)}, lnR_H)$ to a straight line, we may get the activation energy E_g as the slope of the line. Putting E_g back to Eqn. (3.36) we get the m fragility.

Table 3.2 presents the fragility analysis for two series of new Fe-based alloys: series I is for varying metalloid composition and series II is for varying metal composition.

As shown in Table 3.2, each composition was fit with three cooling rates: 10, 20 and 40 K/min. The linear fitting here may be improved by conducting more experiments with more heating rates, as we did for $Fe_{60}Co_{17}Si_8B_7P_8$ in Figure 3.7. This improvement will for sure be much more time-consuming. Here the simple three-point linear fitting yields the fragility of $Fe_{60}Co_{17}Si_8B_7P_8$ to be 12.6, which is close enough to 14.3, the result of Figure 2.7 and Eqn. (3.34). Therefore, we believe the two calorimetric methods basically are equivalent. Then it is not surprising that in Table 3.2 all the m values are unphysically small. As demonstrated by Figure 3.8, if the glass'

Alloy composition	T_g(K), 10 K/min	T_g(K), 20 K/min	T_g(K), 40 K/min	$E_g(kJ)$	m
$Fe_{60}Co_{17}Si_{9.5}B_{8.5}P_5$	763	771	775	546.6	37.0
$Fe_{60}Co_{17}Si_9B_8P_6$	759	765	775	415.5	28.4
$Fe_{60}Co_{17}Si_{8.5}B_{7.5}P_7$	754	762	768	354.7	24.3
$Fe_{60}Co_{17}Si_8B_7P_8$	755	766	789	185.3	12.6
$Fe_{60}Co_{17}Si_{7.5}B_{6.5}P_9$	747	761	786	169.7	11.7
$Fe_{60}Co_{17}Si_7B_6P_{10}$	761	764	774	476.9	32.6
$Fe_{20}Co_{57}Si_{8.5}B_{7.5}P_7$	763	771	782	359.2	24.3
$Fe_{30}Co_{47}Si_{8.5}B_{7.5}P_7$	774	777	786	540.1	36.3
$Fe_{40}Co_{37}Si_{8.5}B_{7.5}P_7$	774	779	788	489.3	32.8
$Fe_{50}Co_{27}Si_{8.5}B_{7.5}P_7$	763	773	779	418.6	28.3
$Fe_{60}Co_{17}Si_{8.5}B_{7.5}P_7$	754	762	768	354.7	24.3
$Fe_{65}Co_{12}Si_{8.5}B_{7.5}P_7$	734	742	755	299.0	21.1
$Fe_{70}Co_7Si_{8.5}B_{7.5}P_7$	726	736	758	190.1	13.5

Table 3.2: Activation energy barrier and fragility

configuration coordinates fall in the local basin with higher average energy than the fully relaxed state, the activation energy barrier (the saddle point) it needs to cross will be smaller. Directly from Eqn. (3.36) we may see that a smaller activation energy E_g will give a smaller fragility m. It is likely that all the fragility measurements we have been able to conduct via the calorimetric approach do not correspond to a relaxed equilibrium liquid. In order to overcome this problem, proper annealing treatment may be necessary.

Two runs of annealing were conducted for $Fe_{60}Co_{17}Si_8B_7P_8$ alloy. The samples were sealed in quartz tube under Argon pressure. Then quartz tube was then placed in furnace at set temperature near T_g for multiple hours before it is quenched in water. After annealing, we did the same variable heating rate DSC measurements and the results are shown in Table 3.3. It is clear that annealing does affect the glass' fragility by allowing the configuration to sample more close to an equilibrium liquid. The value of m increases from 12.6 to 18.7, an increase of about 50%. Yet we cannot be sure that this is sufficient to reach the fully relaxed state. So far it has been an unsuccessful attemp to measure the fragility accurately. However, the apparent m values still possess their relative trend.

Annealing conditions	T_g at 10 K/min	T_g at 20 K/min	T_g at 40 K/min	$E_g(kJ)$	m
As cast	755 K	766 K	789 K	185.3	12.6
477°C (750K), 16 hrs	743 K	758 K	776 K	201.0	13.9
500°C (773K), 20 hrs	750 K	756 K	773 K	270.7	18.7

Table 3.3: T_g of $Fe_{60}Co_{17}Si_8B_7P_8$ after annealing, annealing temperature is nominal

In Figure 3.9 we present the consolidated data for series I (varying metalloid) and series II (varying metal). The subfigures in the left panel (blue circles) are for series I and those in the right panels (red crosses) are for series II. As we have proposed earlier (see equation (3.26)), there are three major factors to influence the glass forming ability: reduced glass transition temperature T_{rg}, fragility m and the liquid-crystal interface energy σ. When alloys have very similar structure

and interactions (at least within the same series), we believe that they should have very similar σ. Therefore T_{rg} and m should account for most of the GFA variance. For series I (blue circles in left panels), the content of P is tuned. When P increases, Si and B decrease accordingly while the total metalloid content is intact and metal constituents are fixed. When P content increases from 5 to 10, the reduced glass transition temperature T_{rg} shows mild fluctuation, but generally keeps very similar value. However, the fragility m shows significant variance, which has a minimum around 8$\sim$9% P, which is exactly the composition with the best glass forming ability. This result is consistent with the findings of experiments of Na et al. [28] that smaller m (stronger glass) appears to yield better glass forming ability. It is also consistent with the findings of Johnson et al. [26] that when other things are equal, smaller m corresponds to a longer time to crystalization. In turn, this allows a slower critical cooling rate, and thus larger glass forming ability. For series II (red crosses in right panels), as the content of Fe increases, Co decreases accordingly while all metalloids are intact. Here both the glass transition temperature and fragility present nearly monotonically descent. Qualitatively we know that larger T_{rg} with smaller m are preferred for better GFA. Therefore there appears to be a competition between these two factors, where the best GFA (around 60% Fe) emerges as a maximum from these two contributions. For both T_{rg} and m data, their curves show a kink at around 60 % Fe. The situation near the low Fe end is interesting. It appears that at 20% Fe the alloy has a better T_{rg} and the same m as at 60% Fe; but the GFA is significantly smaller (which "should" be better considering T_{rg} and m). This may be due to the third factor we haven't been able to identify: the interface energy σ. σ is assumed to be the same under the assumption of similar crystalline phase and structure. However, at low Fe end, when the major crystalline structure are very different, the interaction may not necessarily be the same. In this sense, even T_{rg} and m are not enough to accurately determine glass forming ability.

3.5 Thermodynamics of oxidation reaction

Enthalpy H basically includes two parts: internal energy (the energy necessary to create a system), and energy required to make room for the system by displacing its environment and establishing its volume and pressure.

$$dH = TdS + VdP \tag{3.37}$$

"Standard enthaply of formation" of a compound is the change of enthalpy during the formation of this substance in its standard state from its constituent elements in their standard states. For instance, when aluminum gets oxidized at room temperature and standard atmospheric pressure, the standard enthalpy of formation for allumina would be the change of enthalpy between alumina

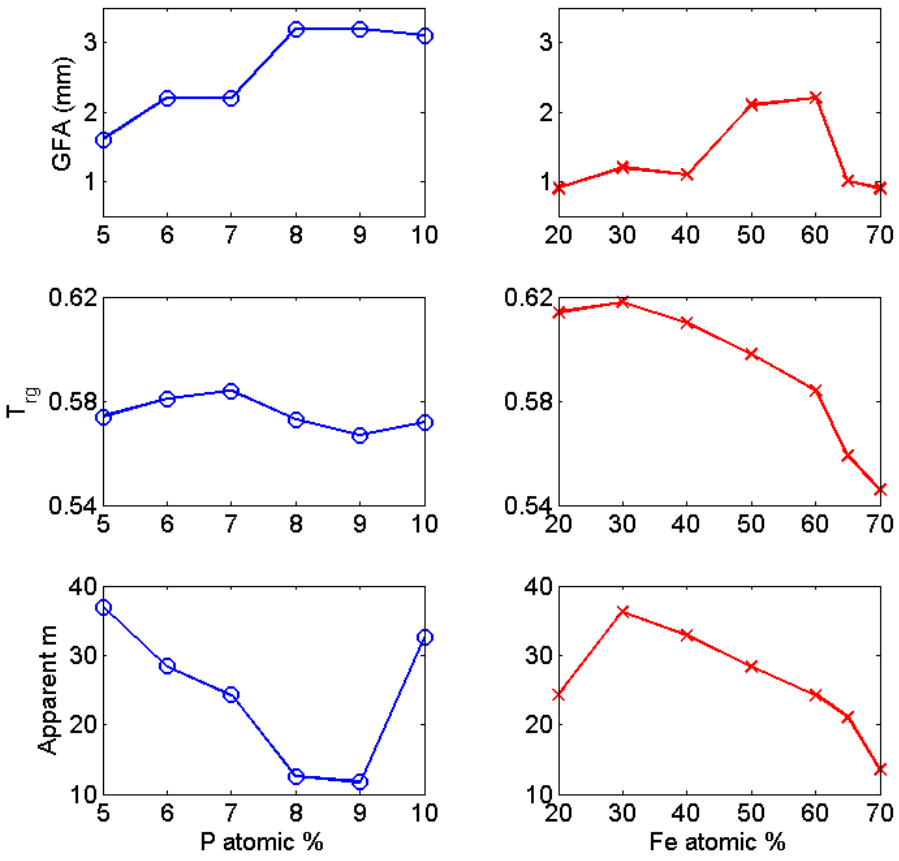

Figure 3.9: Consolidated GFA dependence on Turnbull parameter and fragility

solid from aluminum solid and oxygen gas. Therefore all elements in their standard states have a standard enthalpy of formation of zero.

Gibbs free energy G describes the capacity of a system to do non-mechanic work. It has temperature and pressure as its natural variables.

$$dG = dH - d(TS) = -SdT + VdP \tag{3.38}$$

For a system at constant temperature $dT = 0$, the above equation yields $dG = VdP = \frac{nRT}{P}dP$. For 1 mole of the substance, this integral gives

$$G = G_0 + RT\frac{P}{P_0} \tag{3.39}$$

We now consider a chemical reaction at fixed temperature. Particularly we are interested in oxidation reaction. Similar to enthalpy, there is "standard free energy of formation" of a compound, which

derives from the Gibbs free energy difference between this compound and its constituent elements at their standard states. In oxidation reactions, the reactant A is usually solid or liquid depending on the temperature and reactant B is oxygen gas. The product may be a solid or liquid oxide. Assume the following reaction:

$$\text{A (solid or liquid)+ B (oxygen gas)} \rightarrow \text{C (solid or liquid)}$$

Note that we have simplified the case by taking the stoichiometric coefficient of oxygen to be unit. The coefficients need adjustments accordingly, which will be shown in Ellingham diagram later. Using Eqn. (3.39), the free energy of oxidation reaction is

$$\begin{aligned} \Delta G &= G_C - G_A - G_B \\ &= (G_{C0} - G_{A0} - G_{B0}) + RT(ln\frac{P_C}{P_{C0}} - ln\frac{P_A}{P_{A0}} - ln\frac{P_B}{P_{B0}}) \\ &= \Delta G_0 + RTln\frac{P_C}{P_A P_B} \end{aligned} \tag{3.40}$$

The last equal sign assumes that substances A, B and C have the same pressure at their standard states (say, 1 atm), which is usually true. In oxidation reactions, the ambient environment pressure is usually kept the same. Therefore, the product oxide and the reactant A as solids or liquids have the same pressure as the environment. But the other reactant (oxygen gas) may have a totally different partial pressure. Then the above relation reduces to

$$\Delta G = \Delta G_0 + RTln\frac{1}{P_{O_2}} \tag{3.41}$$

For a chemical reaction to occur spontaneously, there must be thermodynamic driving force, i.e., the free energy change ΔG must be negative. In a closed system, as the reaction continues, the amount of reactants will decrease while the products increase. Specifically for Eqn. (3.41), the partial pressure of oxygen decreases until ΔG increases to zero and the reaction is at equilibrium. Therefore, we could express ΔG_0 as a function of temperature

$$\Delta G_0 = RTlnP_{O_2,equil} \tag{3.42}$$

Note that $P_{O_2,equil}$ is the equilibrium oxygen partial pressure at a given temperature. The standard free energy of oxidation reaction ΔG_0 is the change of free energy at a certain given temperature and at standard pressure, say, 1 atm. (Recall that T is fixed in our discussion here.) It describes the thermodynamic feasibility of a reaction. Notice the difference between ΔG_0 and ΔG. ΔG_0 is for standard pressure, i.e., at the beginning of the reaction, while ΔG contains the instantaneous pressure condition during the reaction process.

3.6 Ellingham diagram

For a reaction at a given temperature T, the standard free energy change of reaction ΔG_0 can be expressed as

$$\Delta G_0 = \Delta H_0 - T\Delta S_0 \tag{3.43}$$

All the subscript "0" denotes standard condition of pressure 1 atm. If we plot ΔG_0 versus temperature, we get a straight line, which is called Ellingham diagram, as shown in Figure 3.10. ΔS_0 is the slope and ΔH_0 is the intercept, where ΔS_0 and ΔH_0 are fairly constant with temperature. The enthalpy change ΔH_0 is a measure of the actual energy that is freed/absorbed as heat. The reaction is exothermic if ΔH_0 is negative, and endothermic if ΔH_0 is positive. The entropy change ΔS_0 is a measure of the change in degree of disorder. In an oxidation reaction where the reactant oxygen gas is greatly reduced, there is normally a large negative change in entropy. It is the dominant contribution to entropy change ΔS_0, while the other reactant and the product oxide are in a condensed state. Therefore, ΔS_0 is negative and quite similar for all metals. The slope ΔS_0 is almost constant, unless melting or vaporizing occurs and significant changes system phase and entropy. Standard free energy of formation is negative for most metal oxides, so the Ellingham diagram is drawn with intercept values to be negative, and the vertical axis has $\Delta G_0 = 0$ at the top.

Since ΔG_0 is negative, there is a thermodynamic driving force to initiate the oxidation reaction. Reactions on the lower part of the diagram have larger driving forces and therefore are easier to happen than reactions on the upper part. When the reaction proceeds, the oxygen partial pressure will decrease until equilibrium, i.e., until the driving force $\Delta G = 0$. Recall Eqn. (3.42) $\Delta G_0 = RTlnP_{O_2,equil}$. If we also plot this on Ellingham diagram, we get a straight line through the origin with slope $RlnP_{O_2,equil}$. For a given temperature, only one equilibrium partial pressure exists, which yields a straight line from origin and intersect the reaction line at the pre-set temperature. With this rationale we could actually read the equilibrium partial pressure from the Ellingham diagram. Assume we are concerning reaction at a given temperature T^*. First, we locate the point for a given oxidation reaction at T^*. Then we connect this point and the origin of the diagram to yield a straight line. With this slope we may calculate the equilibrium partial pressure with Eqn. (3.42). On Figure 3.10, the drawn line crosses the nomographic scale on the right, which is calculated beforehand according to different slopes. Then the equilibrium partial pressure may be easily read off. Here we also see that reactions on the lower part have smaller oxygen pressure at equilibrium.

When two metals are present, two equilibria have to be considered. The lower the position of a metal's line in the Ellingham diagram, the greater the stability of its oxide. The oxide with the more negative ΔG_0 will be formed and the other oxide will be reduced. For example, the line for Al (oxidation of aluminium) is found to be below that for Fe (formation of Fe_2O_3). Metallic aluminum

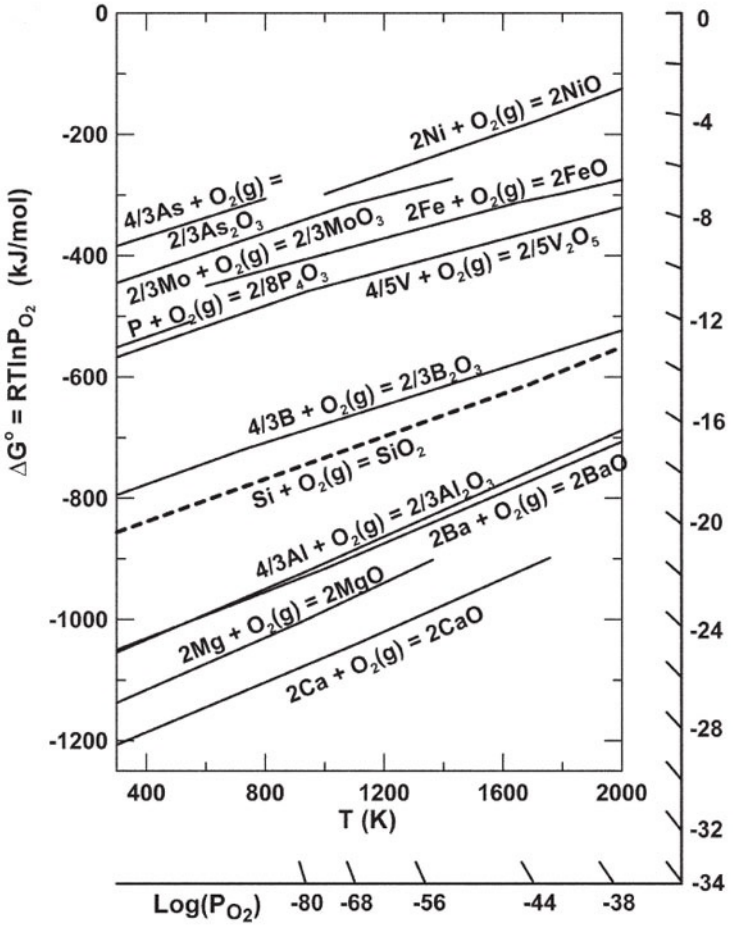

Figure 3.10: Ellingham diagram for oxidation (adapted from [39])

can reduce iron oxide to metallic iron, aluminium itself being oxidized to aluminium oxide. This type of reaction is actually what's happening in the multi-element alloying system. We will discuss later how to take advantage of the Ellingham diagram to suppress crystallization and improve glass forming ability. We need to point out here that Ellingham diagram is purely thermodynamic and not kinetic. As with any chemical reaction prediction based on purely thermodynamic grounds, a spontaneously favorable reaction may be very slow if one or more stages in the reaction pathway have very high activation energies.

3.7 Removing crystalline oxide inclusions by fluxing

The preparation procedure and treatment play a crucial role in determining the alloy's glass forming ability, because often times the intrinsic glass forming ability is overshadowed by extrinsic influences, such as oxide inclusions as heterogeneous nucleation sites. Lin et al. [40] has conducted research on

the effect of oxygen content on crystallization for bulk glass forming ZrTiCuNiAl (Vit105) system. They observed a drastic reduction in the crytallization time for alloys with higher oxygen content. It is critical to control and reduce those heterogenous nuclei in order to make larger alloys.

For multi-element alloys, the constituent metals have very different driving forces for oxidation. The oxides may be either crystalline (for instance, many metal oxides) or glassy (for instance, SiO_2). If there is a significant amount of crystalline inclusion impurities in the alloy, they may serve as initial nucleation clusters as described in Eqn. (2.6). As discussed in Chapter 2, the nucleation rate is proportional to cluster densities; therefore, the existence of crystalline inclusions will significantly increase nucleation and severely limit glass forming ability. Recall that

$$ln(GFA) \sim -ln(R_C) \sim ln(t) \sim -ln(\nu) \sim -ln(N_0) \tag{3.44}$$

In order to prevent metal oxidation, mechanical pump and Ar atmosphere are used for the whole preparation process. However, for some alloying systems which are highly sensitive (for instance, Fe/Co-based) this is not enough. Another stage of fluxing is necessary. During fluxing boron oxide is used as purifying agent. On Ellingham diagram, boron oxidation lies below most metal alloys, which indicates that the residual oxygen tends to combine with boron and dissolve out as flux. The original boron oxide flux works more like a catalyst, which facililates the formation of new boron oxide, therefore the reduction of oxygen in the alloying system, leaving iron and cobalt behind. We have found that even for the best glass former $Fe_{60}Co_{17}Si_8B_7P_8$, if it is quenched right after melting without fluxing, it cannot form a 0.5 mm glass when subsequently quenched.

Another idea to restrict crystalline oxides is to directly include glass forming elements in the alloying system, such as some metalloids. Similar to boron, silicon sits quite low on Ellingham diagram and attracts oxygen from other metal elements, e.g., Fe, Co, Zn, Cr, Mn. The P line is also below that of Fe or Co. More importantly, the resulting products - boron oxide and silicon oxide or phosphate - are all glass formers. Even though these oxide inclusions remain in the alloy, they will not behave as crystalline nuclei, but rather they facilitate glass forming. Fused silica is a glassy state of pure silica. It sustains high temperature and is frequently used in our experiments. Pyrex is another type of glass commonly used for chemical glasswares and cooking glasswares and has main constituents silica and boron oxide. Phosphate glass is a type of optical glasses composed of metaphosphates of various metals. In this sense it makes sense to contain silicon and boron in the consituent elements. We may also have a hindsight for transition metal based system to have the transition metal-metalloid combination. We would like to point out that the amount of B or Si loss due to the formation of boron oxide or silicon oxide in fluxing is very tiny, since there is very limited amount of oxygen at the first place (less than 500 ppm considering the purity of the raw materials in Chapter 2 and the experimental procedure). Therefore, a reduction of 100 ppm oxygen

will not affect the alloy composition by reducing B or Si, but significantly bring down the density of oxide inclusions as heterogeneous nulei. Since the density of nuclei N_0 is directly proportional to the nucleation rate, it has a big impact on the critical cooling rate and glass forming ability.

We are able to observe oxide inclusions in Fe-based alloys. Figure 3.11 are SEM micrographs of amorphous $Fe_{60}Co_{17}Si_8B_7P_8$ alloy. What we observe here are actually pit holes left in the matrix. It is highly likely that the inclusion surfaces have a weaker bonding with the matrix so that they are removed during polishing, leaving pit holes behind. These pit holes (or corresponding inclusions) in Fe-based alloys have the size of $\sim 2-5\mu m$, and average spacing of tens of micron. Figure 3.12 presents the compositional analysis of EDS (energy-dispersive x-ray spectroscopy). EDS analysis reveals that the pit holes have particularly high O/Si/P (probably B as well) concentration and low Fe/Co concentration compared to the matrix. Boron's characteristic X-ray peak cannot be shown on EDS analysis because it is so light that it's very hard to pass through the instrument's Be window. This finding proves that these inclusions are indeed glass-forming substrates, either oxides or phosphates. These pit holes are only found in amorphous samples, but not crystallline ones. The lack of glass-forming inclusions in crystalline samples further fortifies the importance of careful oxygen control. If the oxygen doesn't get the chance to combine with Si/B/P, but rather stays with Fe/Co, the metal oxides form as crystalline nuclei and initiate spontaneous crystallization in a larger scale, resulting in loss of amorphism. Conner et al. [41] has used SEM to find a small fraction of crystals with size $\sim$1 μm and average spacing of tens of microns in Vit106 with high oxygen concentration (1020ppm). They did not see visible crystals in samples with low oxygen concentration (410ppm). They also analyzed the composition of the crytalline phase to find a slight increase in Ni and decrease in Zr and Cu, compared to the matrix. We didn't observe any similar phase separation or crystals in "quenched crystallized" sample.

"Quenched crystalline" means that the sample is prepared by quenching after melting. DSC characterization shows no glass transition behavior nor crystallization behavior heat release, indicating that the sample is crystalline. But XRD indicates that the crystalline peaks are not very sharp. Figure 3.13 is the X-ray diffractometry analysis of a "quenched crystalline" sample. The main (α-Fe) peak is relatively broad. We may estimate the corresponding crystal size by Scherrer equation:

$$\tau = \frac{K\lambda}{\beta cos\theta} \tag{3.45}$$

Here K is a dimensionless shape factor, which is about 0.9 if we assume the crystallite is close to spherical shape. λ is the X-ray wavelength. Cu K_α X-ray has energy of 8.05 eV and corresponding wavelenth of 0.154 nm. β is the broadening at half of maximum intensity, which is about 0.01 for the major peak here. The Bragg angle θ for the major peak is about 45 deg. The calculation yields

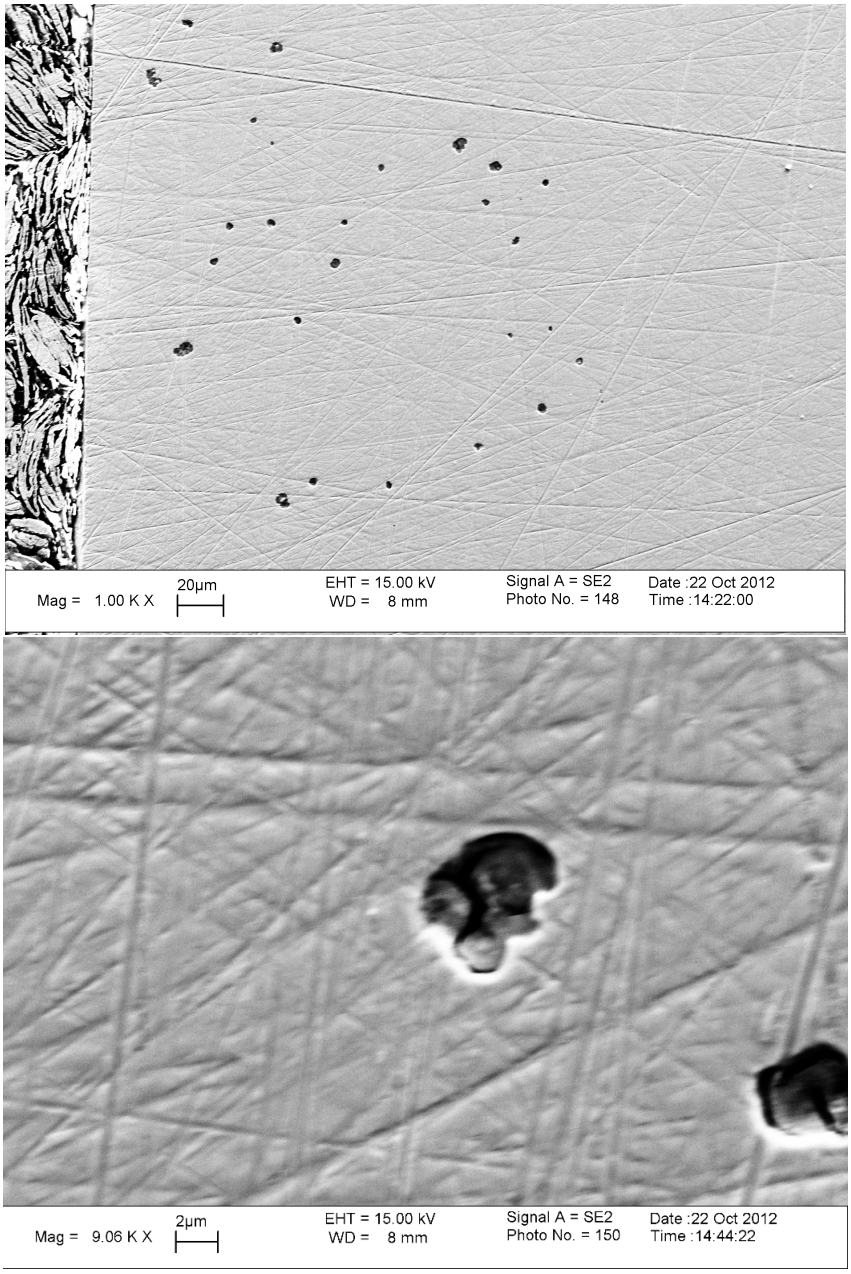

Figure 3.11: SEM graphs of pitholes

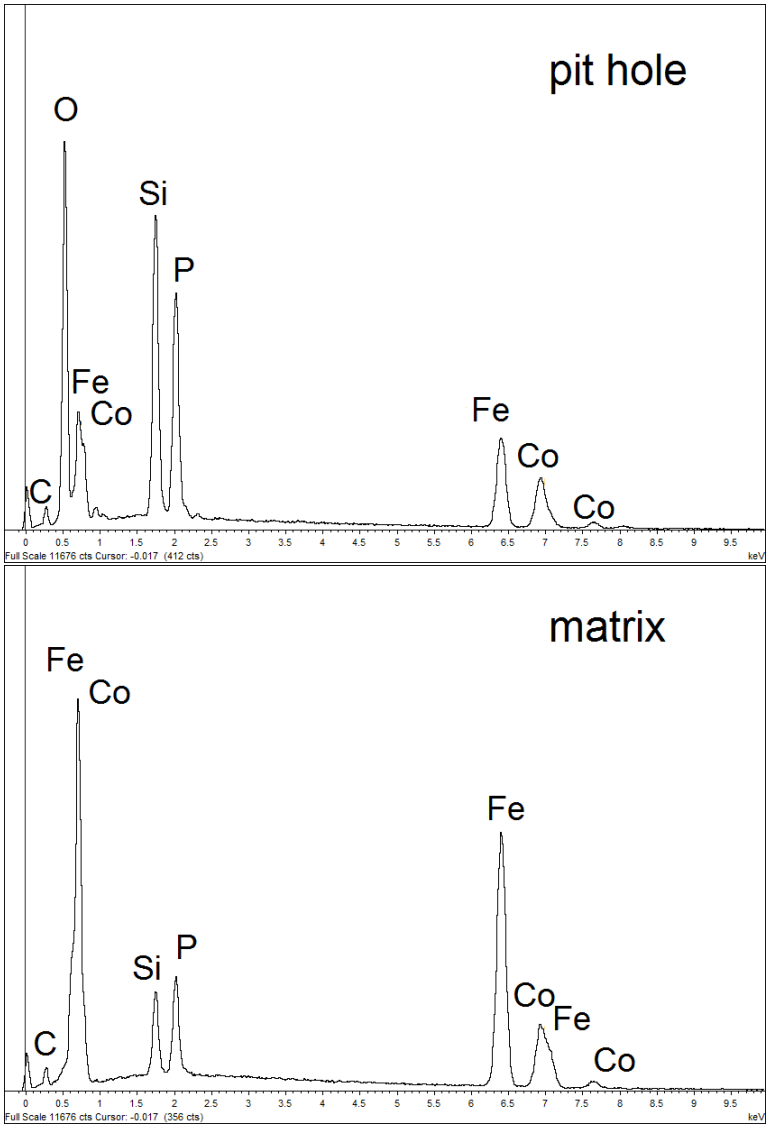

Figure 3.12: EDS compositional analysis

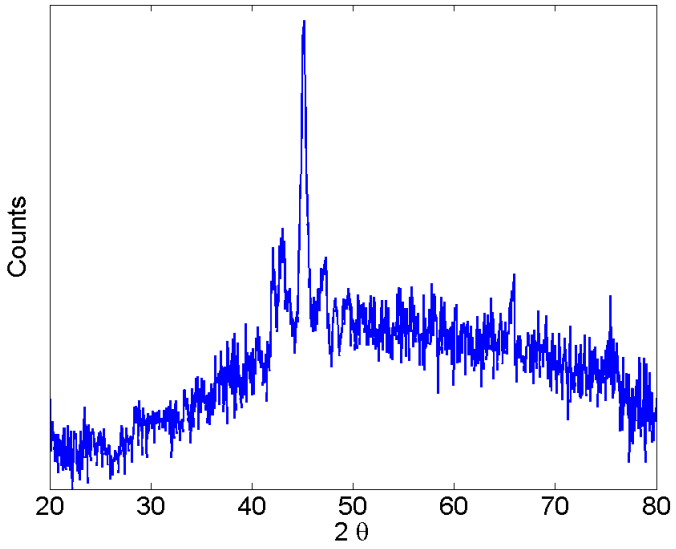

Figure 3.13: XRD of quenched crystalline sample

the average size of crystallite to be $\tau \sim 20nm$, about 100 times smaller than the pit holes in Figure 3.11. This value suggests that for "quenched crystalline" samples the crystallite is very small, and the fluctuation in structure or composition is very hard to be captured by SEM image.

3.8 Removing crystalline oxide inclusions by overheating

Other than fluxing, appropriate overheating is also found to be necessary to control oxide inclusions and improve glass forming ability. The effect of overheating on the crystallization behavior of Zr-based alloys have before been studied by Mukherjee et al. [42]. A threshold overheating temperature was found for $Zr_{41.2}Ti_{13.8}Cu_{12.5}Ni_{10}Be_{22.5}$ (Vit1), $Zr_{52.5}Cu_{17.9}Ni_{14.6}Al_{10}Nb_5$ (Vit105) and $Zr_{57}Cu_{15.4}Ni_{12.6}Al_{10}Nb_5$ (Vit106), above which there is a drastic increase in the undercooling level and the crytallization times. Time-temprature-transformation (TTT) diagrams were obtained for all these three alloys with high-vacuum electrostatic levitator (ESL) technique. It suggests that when the liquid is cooled from a temperature below the threshold, the heterogeneous sites are never dissolved and induce the crystallization. Lin et al. [40] has found that the threshold temperature shows a strong dependence on overall oxygen concentration in Vit105.

Table 3.4 lists several alloys with enhanced glass forming ability after being overheated. The constituent elements are first melted together by induction melting to form a single ingot. The ingot is fluxed and then re-melted in furnace at specific temperatures before being water quenched.

Here glass forming ability only offers a very rough evaluation of the effect of overheating, because the range of GFA for this Fe-based system is not big, and GFA under 2mm is difficult to evaluate

Composition	Melted at 1150 °C	Melted at 1350 °C
$Fe_{60}Co_{17}Si_8B_7P_8$	2 mm	3 mm
$Fe_{60}Co_{17}Si_{7.5}B_{7.5}P_8$	NA	2 mm
$Fe_{60}Co_{17}Si_{8.5}B_{6.5}P_8$	NA	2 mm
$Fe_{60}Co_{17}Si_8B_{6.5}P_{8.5}$	NA	2 mm
$Fe_{60}Co_{17}Si_{8.5}B_{5.5}P_9$	NA	2 mm

Table 3.4: Effects of overheating on glass forming ability

accurately with 0.5mm thick quartz tube wall. However, we are still able to qualitatively justify the existence of the overheating temperature threshold. This threshold lies between 1150 and 1350 °C for this specific system. When the best glass former in the above table $Fe_{60}Co_{17}Si_8B_7P_8$ was heated up to 1400 °C, there is no further improvement in the glass forming ability. A detailed discovery of this threshold temperature can be obtained by researching the crystallization time via ESL. For Zr-based alloys Vit1, Vit105 and Vit106, their threshold temperatures are 1027 °C (1300 K), 952 °C (1225K), and 1137 °C (1410K), respectively.

The high temperature of overheating is used to melt the heterogeneous oxide inclusions so that they won't become preexisting nucleation sites during rapid cooling. We have discussed in previous sections the Ellingham diagram. Although Si and B lines are located below Fe and Co, this thermodynamic driving force only cannot guarantee that oxygen is totally depleted from Fe or Co. The complete equilibrium may take a very long time to reach. In order to understand and control oxygen remaining with Fe (or Co), we resort to the partial phase diagram. The first panel in Figure 3.14 below is the partial Fe-O phase diagram at low O concentration, calculated by Sundman [43]. This diagram covers oxygen concentration from zero up to 350 ppm, which satisfies our region of interest. For this FeCoSiBP system, the oxygen concentration mainly comes from the impurity of the raw materials, which is at most a few hundred ppm. As seen on the phase diagram, the liquidus line is highly sensitive to the oxygen concentration. When the oxygen concentration is only 40 ppm (0.004 %), the liquidus temperature is about 1150 $\sim$ 1200 °C. When the oxygen concentration rises to 80 ppm (0.008 %), the liquidus temperature is much higher, at about 1300 $\sim$ 1350 °C. At this oxygen level, if the alloy is heated only to 1150 °C, the temperature is not enough to dissolve the crystalline α-Fe and Fe_3O_4 and they serve as heterogeneous sites to induce crystallization. When it is overheated to 1350 °C, these crystalline inclusions will dissolve into liquid state. Then it will be harder to crystalize from liquid than with existing nuclei.

The second panel of Figure 3.14 is partial Co-O phase diagram. There's no detail version on the very low oxygen limit as in the Fe-O phase diagram. However, there is still clear exhibition of the steep liquidus curve quite similar to that of Fe-O. The temperature dependence of solubility can be derived following the argument of Porter and Easterling [44]. When oxygen is barely soluble in

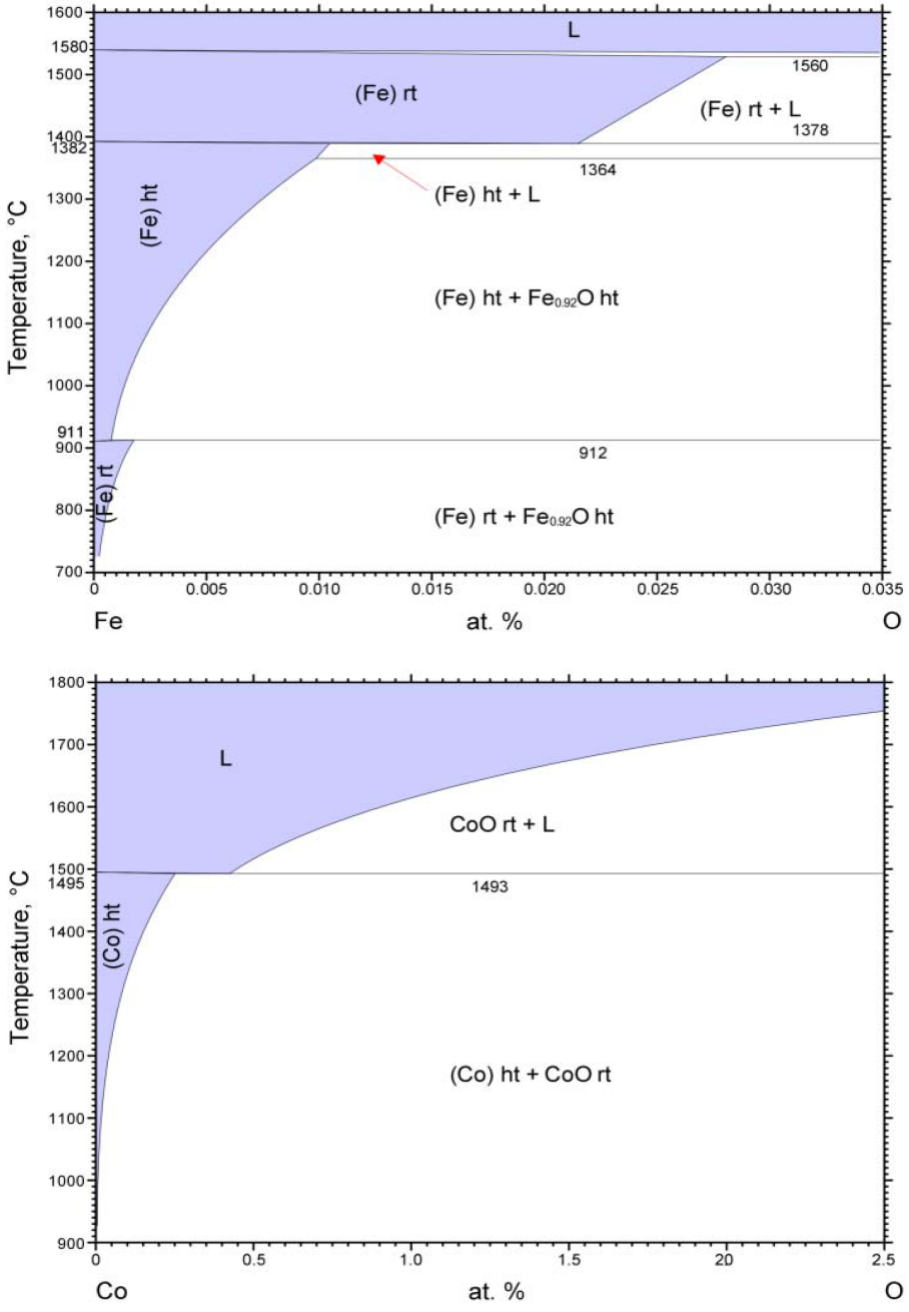

Figure 3.14: Partial Fe-O and partial Co-O phase diagram

cobalt $c_O << 1$, it has an exponential relationship to the temperature as

$$c_O = Aexp(-\frac{Q}{RT}) \tag{3.46}$$

where A is a fitting parameter and Q is the enthalpy change for 1 mol of oxygen to dissolve in cobalt. From Co-O phase diagram, we may fit the curve by the exponential relationship and get the details for lower oxygen level. The fitting yields that the liquidus temperature is about 1060 °C for 100 ppm oxygen, 1036 °C for 80 ppm oxygen, and 970 °C for 40 ppm oxygen. It appears that oxygen has a slightly higher solubility in Co than in Fe. Considering that Fe is also the major constituent element ($\sim$ 60 atomic %), it is the key bottleneck when dealing with oxide inclusions.

Here we have only discussed the binary phase diagram which is the simplest case. In reality the major crystalline oxides would be silicate, borate, phosphate, or even more complicated matters. Yet the essence here is to notice the high sensitivity of liquidus temperature over oxygen concentration. The sensitivity of required overheating temperature also validates the necessity of fluxing. If the oxygen level is at a few hundred ppm without fluxing, the liquidus temperature from Fe-O phase diagram would be over 1400 even 1500 °C, which may damage the quartz tube. (The softening point of fused quartz is 1665 °C.)

The increase in glass forming ability with overheating does not necessarily imply that the crystallization behavior due to heterogeneous nucleation is completely suppressed. Even with crystallization time research by ESL technique, it is possible that the crystallization time is influenced by both heterogeneous and homogeneous nucleation. A statistical analysis with repeated undercooling need to be carried out to distinguish these two. The extent of scattering in the maximum undercooling or crystallization time after isothermal annealing will be correlated with the number of potential nuclei. In a homogeneous nucleation process, all atoms are potential nuclei so the scattering is expected to be large. In a heterogeneous nucleation process, the number of nuclei is a much smaller and relatively fixed number with small variance. If heterogeneous nucleation still plays an important role even after being adequately overheated, then the glass forming ability we have obtained so far is still not the intrinsic one of the composition. Amorphous alloys may still have a big potential into even larger sizes, as long as we find a clever way to clear out the heterogeneous nuclei.

Chapter 4

Seeking Characterization of Soft Magnetic Properties

4.1 Introduction to soft magnetism

A basic motivation of my research on transition metal based metallic glasses is the wide use of soft magnetic devices. Soft magnetic materials can be repeatedly magnetized and de-magnetized. The frequency ranges from as low as 50 or 60 Hz, to the high regime of MHz. Power transformers and electric motors are the most widely used magnetic devices in low frequency regime [45]. High frequency applications include filters, amplifiers and reactors. All these make up an important part of various industries, including computer, medical equipment, automotive, electrical utility, telecommunications, lighting and displays, etc. In general, the choice of magnetic material is a careful consideration of trade-offs between saturation flux density, energy loss and cost. There are a lot of soft magnetic properties and parameters of which not one single optimal material can satisfy all. We will discuss these properties and parameters in the paragraghs below.

First in Table 4.1 we list the correspondence between CGS units and SI units to help clarify future notations. CGS (centimeter-gram-second) has its unique advantage in electromagnetism since it is nicely sized for real world applications.

Description	SI unit – CGS unit
H-field density, magneto-motive force per unit length	1 amp/meter = 0.0125 oersted
B-field, magnetic flux	1 weber = 10^8 maxwells 1 weber = 1 volt-second
B-field density, magnetic flux density	1 tesla = 10^4 gauss 1 tesla = 1 weber/meter^2 1 gauss = 1 maxwell/cm^2
Energy	1 joule = 10^7 ergs, 1 erg = 1 g $\cdot$ cm^2/s^2
Volume magnetization	1 amp/meter = 10^{-3} emu/cm^3

Table 4.1: Key parameters in SI and CGS units

For a typical setup comprising of a coil and a magnet core, both the current in the coil and

the magnet core contribute to the total B-field flux density. The latter is what we usually measure in experiments. The contribution from the coil describes the magneto-motive force and the H-field applied, while the existence of the magnet core helps enhance the concentration of flux lines and increase the B-field within the coil. They have the following relationship

$$\begin{aligned} \mathbf{B} &= \mu_0(\mathbf{H}+\mathbf{M}) \\ &= \mu\mathbf{H} = \mu_r\mu_0\mathbf{H} \\ &= \mu_0(1+\chi)\mathbf{H} \end{aligned} \tag{4.1}$$

where μ_0 and μ are absolute permeability for vacuum and for medium, respectively. μ_r is relative permeability. χ is called susceptibility and is, as well as μ, an indicator for the medium property.

Not all magnetic materials respond equally to the applied H-field. Permeability μ (or μ_r) is an important term to describe the mathematical ratio of flux density to magnetizing force. It is a measure of the magnetic sensitivity of the material. All magnetic materials have a permeability that is greater than that of free space. A material's relative permeability is the ratio of its absolute permeability to that of free space. Thus for all magnetic materials,

$$\mu_r = \frac{\mu}{\mu_0} > 1$$

The absolute permeability of free space is 1 (CGS) or $4\pi \times 10^{-7}$ (SI). Stainless steel has relative permeability of slightly greater than 1, and can reach 1000 when appropriately annealed. Ferrite is about 10 to 1000. Permalloy is about 8000. Metglas can reach 10^6. The permeability of a certain material is not constant. It changes as the excitation level changes, and is also affected by their environment, such as temperature and mechanical shock. As the applied field increases, there is a limit where the permeability appproaches that of free space and cannot hold any more magnetic energy. This is the limited flux capacity and is referred to as saturation. Saturation is a property of the core material; not a function of the excitation or current in the coil. A material's saturation is only a result of its metallurgy and its operating temperature. However, the excitation level to reach saturation depends on other conditions.

A better explanation of various concepts would be illustrated via the hysteresis loop, or B-H loop, as in Figure 4.1. It is obtained by exciting the material with a controlled H-field and recording the resulting B-field induced in the material. As the excitation increases slowly, the magnetization flux is built up in the material and increases until the saturation point. Note that the usual convention is to plot the induced magnetization $\mathbf{M}$, instead of the total $\mathbf{B}$ in Eqn. (4.1). Otherwise, the total B-field should be increasing permanently as the applied H-field increases, instead of becoming flat at saturation, since it is the sum of $\mathbf{M}$ and $\mathbf{H}$. What we actually see in Figure (4.1) is indeed

an "M-H loop." Readers should clarify that when presented a B-H graph. If the loop eventually becomes a straight line with slope 1, we need to make adjustments to get the intrinsic magnetization loop for the material. After saturation, the current is slowly decreased to zero, but the induced flux is not. This value is the residual magnetization B_r. This lag in response is a manifestation of the fact that magnetic materials have memory of their previous excitation condition. When the applied field is large enough in the negative direction, the induced flux is eventually driven to zero. This amount of negative H-field required to demagnetize a material is called the coercivity of the material. Coercivity is a key parameter to differentiate "hard" and "soft" magnetic materials. For soft magnetic materials, it usually takes a small **H** to magnetize, thus the total flux **B** and the intrinsic flux **M** from the material are close. Hard magnetic materials, by contrast, usually have a large coercity, which makes it very difficult to be demagnetized. For example, a hard magnet could have coercivity of tens of thousands Oe, while that of a soft magnet may be below 1 Oe.

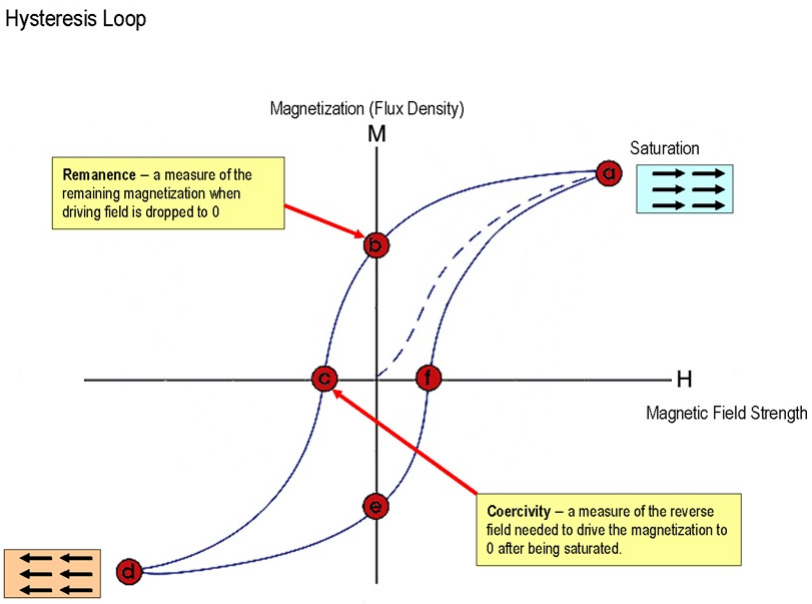

Figure 4.1: B-H loop

Magnetic energy by definition is the product of **B** and **H**. The ability of soft magnetic to store magnetic energy is normally short-term due to the ease of demagnetization. This is desirable in electronic and electrical circuits where cores are used to allow magnetic energy to be converted back into electrical energy easily.

A magnetic circuit is essentially a schematic of the magnetic path in a closed loop, where the magneto-motive force sources (permanent magnets or coils with currents) and drops (areas with low permeability) are represented. The resistance or reluctance of a section not only depends on the material's permeability, but also the dimensions and shape. We can make an analogy between a magnetic circuit and an electrical circuit. Just as electrical current, magnetic flux tends to take

the path of least resistance. Reluctance is inversely proportional to permeability and directly proportional to the length of the magnetic circuit. Minimum circuit reluctance is realized when the material's permeability is high, when the air gap is reduced, and when the configuration tends to form a closed loop. Normally air gap is unwanted not only because it greatly reduces the permeability; more importantly, the flux spreads into the surrounding medium causing the so-called flux fringing effect. It is an unwanted phenomenon, which usually increases proximity and eddy current losses in conductors, which are located in the vicinity of the air gap. There are artifical ways to generate and distribute air gaps intentionally for certain applications though. We point out here that when the device is connected to a circuit that provides current, it will exhibit certain electrical properties as well. Specifically, the inductance is inversely proportional to the reluctance of the magnetic circuit of the device. When a magnetic material saturates, permeability decreases and reluctance increases rapidly. Consequently, the impedance of that device tends toward zero and begins to disappear from the electrical circuit.

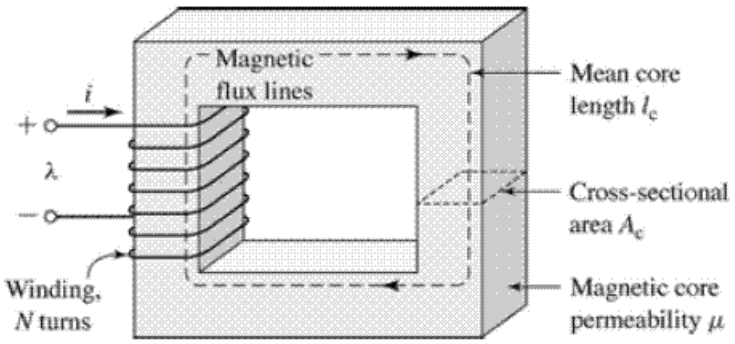

Figure 4.2: Magnetic circuit

When the magnetic core is subjected to a changing magnetic field, such as in transformers, inductors, AC motors and alternators, some of the power that would ideally be transferred through the device is lost in the core, dissipated as heat and sometimes noise. This is known as core loss, and is of great significance in soft magnetics. Core loss has two major components: hysteresis loss and eddy current loss. Hysteresis loss results from the fact that not all energy required to magnetize a material is recovered when it is demagnetized. This is essentially the loop area shown on the hysteresis loop. To reduce hysteresis loss, we want the soft magnetic material to present a "thin" loop shape. Eddy current loss is the heat loss due to small circulating eddy current. This is dependent on the electrical resistivity of the material. Soft ferrites are often used at high-frequency applications due to their very high resistivities and low eddy current losses, although they have large hysteresis losses. Eddy current loss can also be minized by lamination, because the insulating gap between laminated sheets will stop the current flow.

The magnetic cores used in low frequency (50-60 Hz) applications are usually silicon and carbon

steels of various grades. The most advanced crytalline core materials are grain-oriented iron-silicon alloys with high saturation magnetic induction of about 2 T, low core loss and economic feasibility. Possible use of metallic glasses in magnetic applications was realized with the synthesis of noncrystalline $Fe_{80}B_{20}$ in ribbon form. This material has saturation magnetization at room temperature of about 1.6 T, and core loss lower than that of a crystalline $Fe_{50}Ni_{50}$ with the same saturation value. Considerable efforts have since been directed at increasing the saturation induction and reducing the core loss. However, the understanding of magnetism in noncrystalline solids is still very limited. We aim to investigate the soft magnetic properties of the newly developed Fe-based metallic glasses and to correlate the magnetic properties and the structural and thermodynamic properties. The understanding may further help optimize alloy development for applications. In order to do that we need appropriate instrumentation. In section 4.3, we will discuss the build-up of a B-H loop device which may help provide simple but straightforward results. In section 4.4, we will also investigate the attractiveness and feasibility of commercially available measuring systems for soft magnetic materials. Preparation of samples with specific sizes and shapes are experimented and results are presented in section 4.5.

4.2 Ferromagnetism in amorphous alloys

The origin of magnetism has long been a myth to physicists. While most substances are paramagnetic, with a typical magnetization of about 10^{-3} emu/cm^3, pure iron has saturated magnetization of about 1700 emu/cm^3. Ferromagnetism therefore involves an effect which is millions of times strong. But no progress in understanding ferromagnetism was made until Weiss introduced his hypothesis of the molecular field in 1906 [46]. His theory contains two essential postulates: spontaneous magnetization, and division into domains. According to Weiss, there is a molecular field acting in a ferromagnetic material regardless of the Curie temperature, and it is so strong that it could magnetize the material to saturation in absence of an applied field. A ferromagnetic material in its demagnetized state is divided into a number of smaller regions called domains. Each domain is spontaneously magnetized to saturation, but the directions of magnetization of various domains are cancelling each other so that the specimen as a whole has no net magnetization. The process of magnetization is one of converting the specimen from a multi-domain state into one with a single domain in the direction of the applied field.

The Weiss theory of molecular field says nothing about the physical origin of the field, except the implication that a coorperative interaction is involved. It was not understood until 1928 when Heisenberg showed that it was caused by quantum-mechanical exchange interaction, which has no classical analog. It is due to the wave function of indistinguishable particles being subject to exchange symmetry, i.e., the wave function either remains unchanged (symmetric) or changes sign

(antisymmetric) when two particles are exchanged. The exchange energy forms an important part of the total energy and plays a decisive role in ferromagnetism. If two atoms have spin angular momentum $\mathbf{S}_i$ and $\mathbf{S}_j$, then the exchange energy between them is given by

$$E_{ex} = -2J_{ex}\mathbf{S}_i \cdot \mathbf{S}_j = -2J_{ex}S_iS_jcos\phi \tag{4.2}$$

where J_{ex} is the exchange integral, from the calculation of exchange effect. $cos\phi$ is either 1 (parallel spins) or -1 (antiparallel spins). Therefore, if the exchange integral J_{ex} is negative, then the lowest energy results from antiparallel spins. If J_{ex} is positive, parallel spins are favored. Since ferromagnetism is due to the parallel alignment of spins on adjacent atoms, a positive J_{ex} becomes a necessary condition. Figure 4.3 shows the variation of exchange integral with the ratio a/r, usually called the Bethe-Slater curve. a is the atom radius and r is the radius of 3d shell, because the spin alignment of 3d electrons is the immediate cause of ferromagnetism. $2a$ is the atom diameter, as well as the distance apart of the atom centers. When interatomic distance is very small it brings J_{ex} to be negative, which favors antiparallel spins and thus antiferromagnetism, which separates Fe, Co, Ni from Mn.

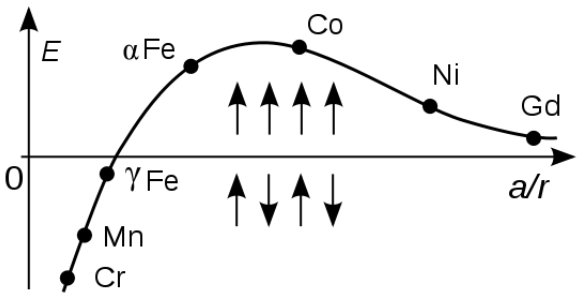

Figure 4.3: Bethe-Slater curve

Band theory explains why the partially filled 3d electrons play a key role in ferromagnetism. For a single atom, an electron energy level goes from 1s, 2s, ... up until 3d and 4s orbits, which are very close. When many atoms are brought together to form a solid, their electron clouds begin to overlap and Pauli principle prevents them from having one single 1s level - so the 1s level split into many sublevels which actually form a band. So do 3d and 4s levels. The 3d band and 4s band actually overlap to a great extent. In many transition metals, the electrons will only fill up to part of 3d and 4s bands. For free atoms, the n 3d electrons will fill the lower $n/2$ sub-levels, with half of them spin-up and half spin-down. But exchange force will create spin imbalance (for instance, more than half spin-up and less than half spin-down), which creates magnetic moment. Partially filled 4s band will not be affected by exchange force because its density of state is quite low and the spin imbalance will cause a significant energy increase. Researchers have studied binary alloys of Fe, Co, and Ni with each other and with other elements. When two elements go into solid

solution in each other, the variation of the saturation and Curie temperature T_C with composition is generally unpredictable. When an alloy consists of two phases, and a change in total composition changes only the relative amout of the two phases, the alloy's saturation will vary linearly with the weight percentage, and T_C will remain constant. The Slater-Pauling curve shown in Chapter 2 (Figure 2.2) is an example of single-phase solid solutions. Issues about ferromagnetism remain rather complicated. Today there is no single theory, but many viewpoints from various experiments and theories. Cullity's and Berkowitz's books [47, 48] offer abundant information for further reading.

Gubanov [49] first studied the theory of ferromagnetism in noncrystalline substances. As ferromagnetism is caused by exchange interaction between neighboring atoms, there is no need to have a rigorous periodicity in the distribution of magnetic atoms. Theorists have used effective mean field theory to study this topic, which is greatly facilitated by more and more advanced computational techniques today. Magnetism in amorphous state is effectively determined by the relative relation between the nature of exchange interaction and the local configuration of magnetic atoms [50]. The various transition-metal based amorphous alloys in which 3d magnetic moments are diluted have a density of states at the Fermi level which is more or less depressed as compared with pure transition metals. Nevertheless, the d-character of these electronic states is basically preserved. [7]

Accumulating experimental evidence has shown that amorphous alloys display a well-defined magnetic transition just like the second-order phase transition occurring in most crystalline magnets. Indications for a sharp transition at the Curie temperature T_C were provided by early Mossbauer and specific heat measurements on amorphous iron alloys. We have been able to identify T_C as the peak of the 'λ-transition' by DSC measurements. The Curie temperature was found in most cases to be affected by the structural disorder more severely than the saturation magnetization. The effects of metal and metalloid substitutes have been studied in great detail for binary and ternary systems [7]. Although our quinary system is more complicated, it is still found to follow the general trend, as shown in Figure 4.4. The first four series of data were taken from Luborsky's paper [51]. The last one series (black diamonds) are the results for $(Fe_xCo_{1-x})_{77}Si_{8.5}B_{7.5}P_7$, which are well in the same range with other series. The new Fe-based alloys' slightly lower Curie temperature may be due to the effect of dilution. Discrepancy may come from different experimental methods, since induction method is usually used with an AC bridge. Here T_C goes through a maximum value at around 50 atomic % of Co. It is believed that the magnetic moment decreases rather linearly with increasing Co content [7]. For the newly developed Fe-based alloys, we have been trying multiple approaches to characterize their softmagnetism, among which the saturation might be the most important one.

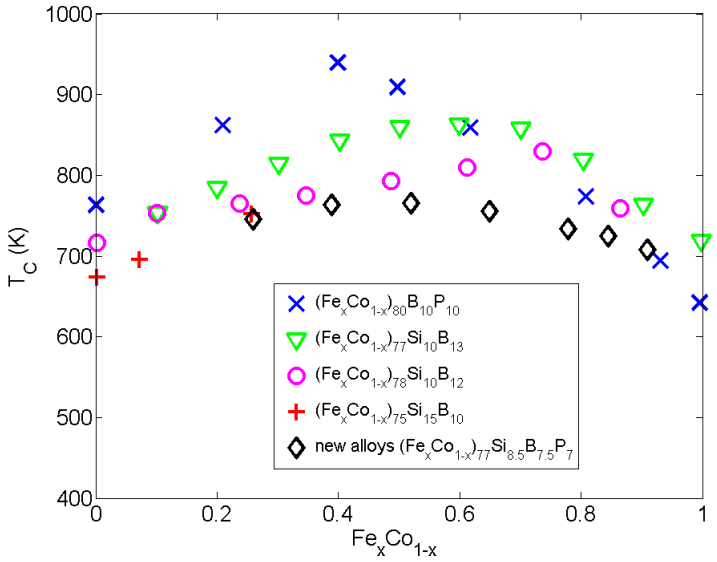

Figure 4.4: Curie temperature as a function of metal composition in FeCoSiBP series

4.3 In-house B-H loop device

A hysteresis B-H loop is able to provide several essential characters of great interest without engaging complicated measurements; therefore, an in-house B-H loop device will be very helpful. We have used the following devices in building up the B-H loop device: a 10 MHz four-channel analog oscilloscope (TENMA-72-8725), a 10 MHz sweep function generator (BK4017A-ND), a 0-30V two-channel power supply (Mastech HY3005F-3), as well as necessary electrical accessories. Figure 4.5 is a diagram of the circuit. The operating principle of the circuit is similar to that of a transformer.

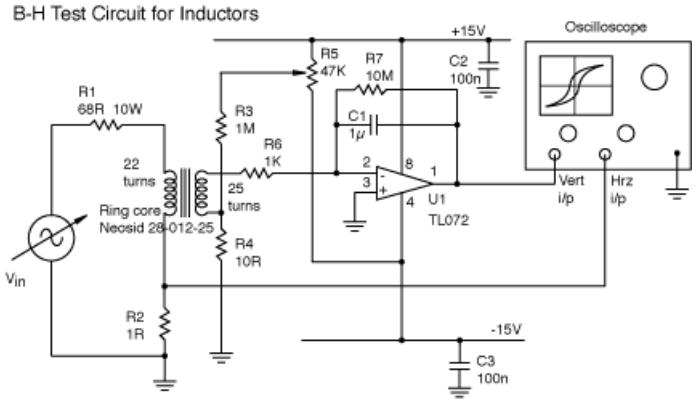

Figure 4.5: B-H loop circuit

The magnetic core inside the coils shown in the diagram comprises of a yoke and a sample rod, as shown in Figure 4.6. A sample rod with length $\sim$ 8 cm is placed in the gap of the C-shape yoke made with Metglas ribbons in order to form a closed magnetic loop. The C-shape yoke was provided

by Dr. Hasegawa. It has an air gap of 85 mm (to place the rod) and a cross section of 15 mm $\times$ 15 mm. A rectangular-shape core was made by Metglas2605SA1 (an Fe-B-Si based alloy) ribbons of thickness $\sim$ 25 μm, wound on a mandrel and glued by epoxy. It was then annealed in a magnetic field 20 Oe along the ribbon length direction at 340 °C for one hour and cut out to make the C-shape core. The Metglas ribbon has an acclaimed as-cast saturation of 1.56 T, as-cast permeability 45,000 and high-frequency annealed permeability 600,000. One or more layers of copper wires were wound tightly around the yoke, in order to provide various connections in series or in parallel. We put a plastic isolation layer between the yoke and the innermost layer of wire, as well as adjacent layers, in order to prevent the sharp edge of the yoke from cutting wire and causing leakgage. Each pair of plastic shield layer and wire layer would add $\sim$ 0.6 mm to the distance from the yoke; therefore, if we have four layers of windings, the cross sectional area from the outermost layer would be $\sim$ 20 mm $\times$ 20 mm. This distance will have an effect on the magnetic coupling and we will discuss the effect in later sections. The number of windings is theoretically arbitrary; yet we tend to make it as large as possible to fully utilize the length of the yoke so as to increase the primary excitation. Each layer has maximum $\sim$ 350 turns of windings. There's one layer of copper wire on the sample rod as secondary, or pick-up coil. The secondary coil can be as thin as possible, while the primary one only need to be thick enough so as not to heat up the coil too much (the saturation of the core falls rapidly with temperature). Here for both we have used 30 AUG magnetic copper wire which is $\sim$ 0.26 mm thick. The sample rod used to configure the circuit is a 8.5 cm long, 3 mm diameter iron-based metallic glass rod, with saturation magnetization a little over 1 T.

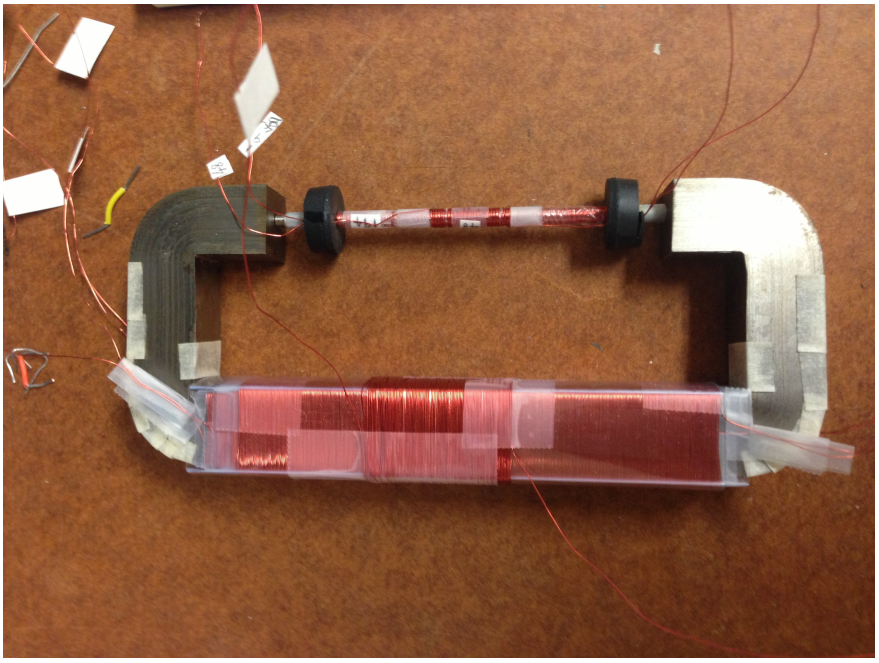

Figure 4.6: Yoke and sample rod

An oscillating sinusoidal current is driven by the function generator in the primary coil. A secondary current generated by electromagnetic induction in the magnetic circuit is measured by the oscilloscope. In the circuit diagram, resistor R_1 is to adjust the current. Clarke [52] has found that a source of AC current of about 0.3 A is needed to excite a reasonable secondary signal. The op-amp is used as a voltage inegrator. R_7 helps keep the drift from voltage and current offset under control. R_5 needs to be adjusted so that the output on pin 1 remains steady with no signal in or out of the integrator. The oscillator must be a 2 channel model with an "X-Y" mode in order to present essentially the primary voltage and the secondary voltage together.

An initial test of the circuit has primary coil $N_P \sim 100$ turns, secondary coil $N_S \sim 140$ turns, yields a very flat ellipse loop on the oscilloscope, as shown in Figure 4.7. The primary current I_P

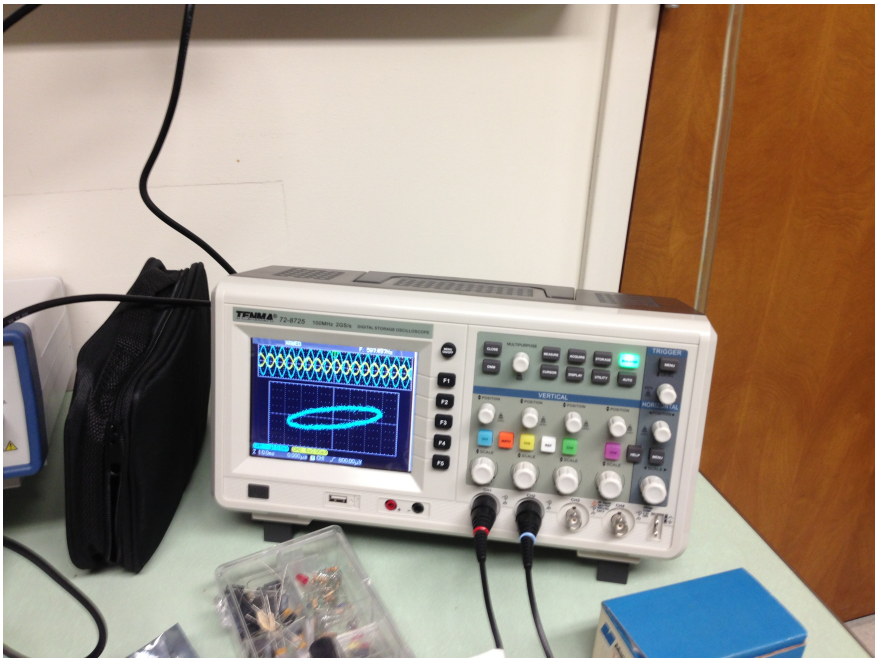

Figure 4.7: B-H loop

was measured to be $\sim 120mA$ via the voltage across R_2, as indicated by the horizontal span of the ellipse. Therefore, the change in applied field strength through the primary coil is

$$\begin{aligned} H &= N_P \times I_P / L_e \\ &= 100 \times 0.12/0.3 = 40A/m = 0.5Oe \end{aligned} \tag{4.3}$$

where $L_e \sim 30cm$ is the effective length which the primary coil covers. This value is adequate to saturate some Fe-based amorphous alloys. For example, $Fe_{81}B_{13.5}Si_{3.5}C_2$ need only about 0.3 Oe to reach saturation [53]. This difference makes it surprising that the B-H loop we see is far from saturation. A longer primary coil (300 turns instead of 100 turns) has been tried, but the improvement

on flux density is marginal, which indicates that these are not the key barriers. According to Eqn. (4.3), although the H-field is proportional to the winding number, the current is greatly suppressed when more windings gives larger inductance, therefore, smaller current.

Calculation of the excited flux is from the reading of vertical axis on the oscilloscope V_0, which tells the voltage on the secondary coil via the op-amp integrator.

$$\Phi = V_0(C_1R_6)/N_S \tag{4.4}$$

The B-field, or the flux density, is

$$B = \Phi/A_e \tag{4.5}$$

where A_e is the effective area for the flux to go through, which is just the cross sectional area of the sample rod. It could be more complex in a toroid configuration. Therefore, with $V_0 = 30mV$, $C_1 = 1\mu F$, $R_6 = 1k\Omega$, and $A_e = \pi \times (1.5mm)^2$ for the 3 mm diameter rod, we get

$$B = \frac{0.03 \times 10^{-6} \times 10^3}{140 \times 3.14 \times (0.0015)^2} = 0.03T$$

Comparing the excitation field 0.5 Oe and the induced field 0.03 T (most of the Fe-based alloys reach 1 T of saturation), the effectiveness of the coupling inside the magnetic circuit need to be further investigated. A tranformer configuration is set up for this purpose, as illustrated by Figure 4.8. Still the sample rod is placed in the air gap of the yoke to form a magnetic circuit. Channel 1

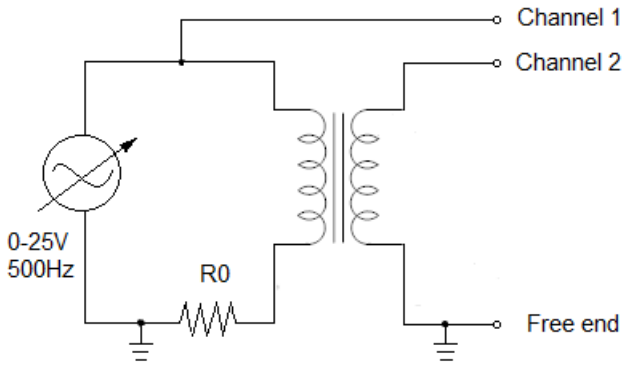

Figure 4.8: Simple transformer circuit

of the oscilloscope (horizontal axis) need to switch between the generator output (across both the primary coil and R_0) and the voltage only on the primary coil around the yoke, while channel 2 (vertical axis) is to pick up the secondary voltage around the sample rod. For an ideal transformer,

Configuration in series	Generator output	Primary current	Primary voltage	Secondary voltage	$\frac{voltageratio}{turnratio}$ $\frac{V_S/V_P}{N_S/N_P}$
layer 1 only	17 V	188 mA	15.2 V	2.4 V	28.5 %
layer 2 only	17 V	188 mA	15.2 V	1.8 V	21.4 %
layer 3 only	17 V	188 mA	15.2 V	1.6 V	19.0 %
layer 4 only	17 V	188 mA	15.2 V	1.5 V	17.8 %
layers 1, 2	21 V	63 mA	20.4 V	1.7 V	30.1 %
layers 1, 2, 3	22 V	29 mA	21.7 V	1.3 V	32.4 %
layers 1, 3, 4	22 V	28 mA	21.7 V	1.3 V	32.4 %
layers 1, 2, 3, 4	23 V	16 mA	22.8 V	1.2 V	38.0 %

Table 4.2: Coupling efficiency

$V_P/V_S = N_P/N_S$. However, flux leakage may cause inefficiency

$$\frac{V_S/V_P}{N_S/N_P} < 100\% \tag{4.6}$$

We may calculate this percentage to describe the coupling efficiency. Here all layers of primary windings are $\sim$ 350 turns, and multiple layers may be connected in series. When $R_0 = 9.6\Omega$, a 500 Hz AC source yields the following results in Table 4.2:

It is obvious that the efficiency of the transformer configuration is very low, where the voltage ratio is at best one third of the turn ratio. This may be due to the large mis-match between the cross sectional areas of the yoke (225 mm^2) and the sample rod (7 mm^2). Leakage flux is widely present in real world transformer. It traverses the theoretical path and escapes out of the magnetic circuit. For the flux going through the yoke across the interface, it tends to escape without entering the thin rod. The coupling coefficient can be determined from the primary self-inductance, secondary self-inductance, and their mutual inductance. A simple series RLC circuit is used to detect the inductances. When the circuit is at resonance, the current and the voltage output are in phase, therefore a straight line (instead of an ellipse) is present on the oscilloscope. The resonant frequency is

$$\omega_0 = 2\pi f_0 = \frac{1}{\sqrt{LC}} \tag{4.7}$$

When the inductance changes, the frequency from the AC source need to change accordingly in order to retain resonance. Approximately,

$$\left|\frac{\Delta L}{L}\right| = \left|2\frac{\Delta f_0}{f_0}\right| \tag{4.8}$$

With capacitor $C = 22nF$, and resistor $R = 281\Omega$, we've deteced the resonance frequency with and without the sample rod. When the rod is inserted, the yoke and the rod form a transformer configuration just as in Figure 4.8. Each layer of primary winding has $\sim$350 turns. Table 4.3

Primary windings	f_0 yoke alone	f_0 yoke with rod	$\frac{\Delta f_0}{f_0}$	$\frac{\Delta L}{L}$
one layer only	6485 Hz	6344 Hz	2.2 %	4.4 %
two layers	3224 Hz	3118 Hz	3.3 %	6.6 %
three layers	2177 Hz	2060 Hz	5.4 %	10.8 %
four layers	1642 Hz	1533 Hz	6.7 %	13.4 %

Table 4.3: Resonance frequency

presents the resonance frequency results to see the effect of inserting sample rod. When there's only the primary coil (including the yoke as its core), the electrical circuit is governed by

$$V_P = L_P \frac{dI_P}{dt} \tag{4.9}$$

When the rod is inserted, mutual inductance M will come into the picture so that a new inductance from the primary coil is detected

$$\begin{aligned} V_P &= L'_P \frac{dI_P}{dt} \\ &= L_P \frac{dI_P}{dt} - M \frac{dI_S}{dt} \\ &= (L_P - M \frac{dI_S}{dI_P}) \frac{dI_P}{dt} \end{aligned} \tag{4.10}$$

The mutual inductance M reflects the transformer's coupling coefficient k as $M = k\sqrt{L_P L_S}$. Theoretically $0 \leq k \leq 1$, while $k = 1$ is the perfectly coupled condition. And $I_S/I_P = \sqrt{L_P/L_S}$. Hence we get

$$L'_P = L_P(1-k) \tag{4.11}$$

$$\frac{\Delta L_P}{L_P} \sim k \tag{4.12}$$

The last column of the table clearly shows that the coupling coefficient is significantly low, considering that even real world transformers usually have the k value very close to 1. Notice that Table 4.2 and Table 4.3 are in different frequency regions, the first one is tested in 10^2 Hz regime while the second is in 10^3 Hz regime. We could essentially repeat the experiments for Table 4.3 in the 10^2 Hz regime, but that would require the capacitor to be hundreds of times larger. For Table 4.2 and Table 4.3 they both show that the low coupling efficiency is a key challenge in the B-H loop circuit. Considering that many iron alloys with promising soft magnetic properties have GFA of only 2 or 3 mm, it may be helpful to use nickel-based alloys developed by Na et al. [16] which have GFA over 1 cm, in order to overcome the mis-match problem and identify the feasibility of this method. An in-house B-H loop device is in practice more difficult to build than we thought. Not simply following a theoretically correct circuit diagram, it may actually require a lot of hands-on electrical

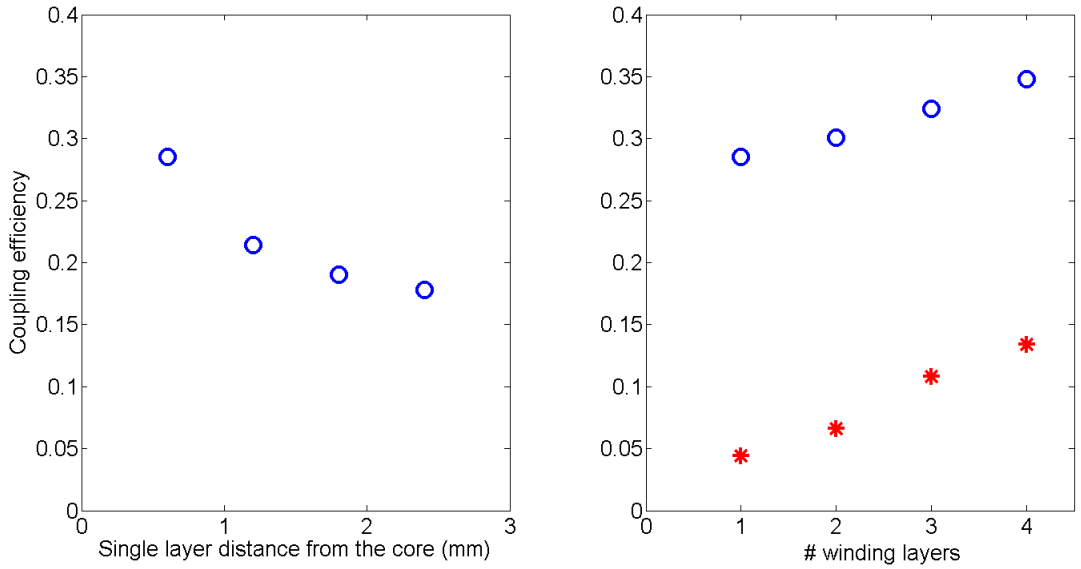

Figure 4.9: Coupling efficiency of different configurations

engineering experiences. In the next section we will discuss some commercially available measuring systems which give a holistic yet more complicated characterization. Air gap at the contact surfaces between the yoke and the rod is negligible, since loose and tight contacts have shown very little difference.

Yet we still have a few interesting findings from experimenting the B-H loop circuit. First of all, the distance of the winding from the yoke has an effect on secondary voltage. As shown in Table 4.3, from layer 1 to layer 4, the coupling efficiency drops, as each pair of plastic shield and wire layer adds $\sim$ 0.6mm to the distance, as shown in Figure 4.9. Second, multiple layers do help increase the efficiency of the coupling, maybe due to stronger magnetization in the yoke and therefore stronger excitation for the rod. However, this is offset by the increase in the primary turns to actually reduce the secondary signal. This is true for both 10^2 Hz regime (blue circles) and 10^3 Hz regime (red asterisks).

4.4 Hysteresis graph test systems

There are multiple commercialized machines to test the hysteresis loop at various conditions, manufactured by industry companies. Usually AC models have more restrictions than DC models on sample sizes and shapes. They are more expensive as well, especially for high frequency measurement. Here we examine as an example: the AC/DC permeameters for soft magnetic rings and strips, manufactured by the company Laboratorio Elettrofisico Walker LDJ Scientific (LE Walker). This is a whole line of permeameters for soft magnetic materials from DC to 20 kHz, 50 kHz, up to 1

MHz. Dynamic AC properties are affected by many factors dpending on the particular application conditions. The permeameter is designed with realistic characteristics of saturation, retentivity, coercivity, permeability, losses, etc. The machine allows two types of geometries to be measured: ring and strip. For strip size, a sample is required to be 30 mm wide and 300 mm long in order to utilize a specific frame for strip. This may be useful for thin films made by spin melting, but the geometry doesn't allow samples made by water quenching or vacuum casting. On the other hand, ring size doesn't have any specific requirement. More importantly, ring or toroid are the best shapes for magnetic characterization, since it is a naturally closed circuit, and demagnetizing field within the material is zeroed. Demagnetizing field is the H-field generated by the magnetic material itself. When it is present, the total H-field is different from the applied external field and this needs to be taken into account when plotting B-H curve for the magnetic material. This issue is avoided in a ring or toroid since no magnetic poles exist as H-line source. Rings can be made by stacked disks with the same inner and outer diameters, and by punching or laser cutting. It can also be prepared by thin film wound as a clock-spring. It is very important to perform the test in conditions that are similar to the designated application. Although there's no physical limit on ring size, essentially it has to be big enough to hold enough turns of coils, since the sample has to be prepared with widing both a primary coil for excitation and a secondary coil to detect the magnetic flux. The size also affects the maximum H-field.

A typical ring used for this test system has 1 cm inner diameter and 1.5 cm outer diameter. We may use these values to calculate a reasonable H-field which is generated inside the ring by the primary coil. The effective length of a ring/toroid is given by

$$L_e = 2\pi \frac{R_1 R_2}{R_2 - R_1} ln \frac{R_2}{R_1} \tag{4.13}$$

where R_1 and R_2 are inner and outer radii respectively. For the ring size given above, $L_e = 3.8cm$. Assume we still use 30 AWG copper wire. A reasonable guess for the number of turns is that the primary coil occupies about one quarter of the ring circumference, which still leaves enough space for the secondary coil and heat release. This gives the number of turns to be about

$$N_P = \frac{1/4\ of\ ring\ circumference}{wire\ thickness} = \frac{0.25\pi(1cm)}{0.025cm} \sim 30turns \tag{4.14}$$

The fusing current for the wire is about 10A for 10 seconds. Considering the typical test time as 60-120 seconds, it is reasonable to assume a safe working current as 0.5A. At these conditions, the H-field generated by the primary coil is about

$$H = \frac{N_P I_P}{L_e} = \frac{30 \times 0.5}{0.038} = 400A/m = 5Oe \tag{4.15}$$

which is about 10 times what we've gotten from the in house B-H loop device and is big enough to saturate a soft magnetic material.

For iron-based bulk amorphous alloys, it may be challenging to cast a disk with large diameter due to its marginal glass forming ability and brittle character under thermo-stress. Even if we only have a small ring with outer diamter 0.5 cm and inner diameter 0.33 cm which is one third the size of a typical ring sample, we can make a similar calculation and get an estimated H-field to be the same. (Both number of turns and effective magnetic length would reduce to one third of the previous value.) Ideally the ring size doesn't matter too much in terms of H-field, which assures us the advantage of ring shape sample for the hysteresis graph test system, but too small a ring may bring practical challenge of handling and circuit set-up. In the next section we will discuss the preparation of ring shape sample via different experimental approaches.

4.5 Ring sample preparation by casting and etching

In order to prepare ring-shape samples for hysteresis graph test, we have used various casting methods to make thin plates. Electrical discharge machining (EDM) is then to be used to etch out rings. Alloy $Fe_{60}Co_{17}Si_8B_7P_8$ is chosen since it has the best glass forming ability (3 mm) in this family of Fe-based alloys. Previous experimental experience suggests that an amorphous metal which has critical rod diamter of 3 mm can be made into plate up to $\sim$1 mm thick. This is partly due to the geometry and partly due to the heat transfer efficiency. A simple argument is that the ideal critical size of a certain geometry depends on the ratio between the volume and the surface area, provided that the processing conditions are the same. The critical thickness of a plate sample is usually much smaller than the diameter of a rod sample. Moreover, the high aspect ratio of the plate's cross-sectional area makes it harder to conduct heat out efficiently and uniformly. This severe non-uniformity furthers introduces thermal stress inside the sample and the plate tends to shatter easily during quenching.

Thin plate $\sim$ 0.8 mm thick has been successfully made by copper mold casting. After appropriate fluxing, alloy ingot was placed in quartz nozzle or quartz capillary. The casting was vacuumed by both mechanical pump and turbo pump to reach a vacuum better than 10^{-4} mbar and then refilled by Ar to near atmosphere. The best chamber pressure is about 0.2 bar below 1 atmosphere. Even lower pressure would benefit the purge force. However, it will also facilitate the evaporation of phosphorous, which generates bubbles and induces crystallization. 1300 °C and 1/3 bar appear to be an optimal combination of temperature and pressure for purge. Figure 4.10 shows two samples from rectangular and ring shaped slot, respectively. The sample on the left is $\sim$ 0.75 mm thick and 2 cm wide. The bottom part of the sample is fully amorphous, while the top part is crystalline due to the heat from surplus material. Non-uniform temperature and flow tend to generate thermal

Figure 4.10: Samples cast from rectangular and ring shaped molds

stress and induce cracking and shattering. The sample on the right is $\sim$ 1 mm thick and 1.5 cm in diameter, and it is fully amorphous. The challenge for directly casting from ring-shaped slot is that the argon gas trapped between the two streams will place resistance on the liquid so it is difficult to get a complete ring.

Water quenching quartz mold is another approach. It has the advantage of particularly clean finish since the alloy doesn't wet quartz. However, the vulnerability under thermal shock and low thermal expansion coefficient make quartz not a good candidate as mold, since it aggravates the thermal non-uniformity yet doesn't allow free expansion/contraction.

Chapter 5

A Numerical Investigation

In this chapter, a quantitative description of the millisecond capacitive discharge heating and forming process built on a finite-element simulation platform is introduced. The platform incorporates thermodynamic and rheological models that extend beyond the supercooled liquid regime accessible by conventional calorimetry and rheology, accessing the regime that has just recently been uncovered via millisecond Ohmic heating. For the first time, a description of the dynamic glass transition is introduced and incorporated into the platform. The platform accurately simulates the process evolution and the thermodynamic and rheological response of the metallic glass, providing excellent agreement with experiments. Features such as the rapid temperature response, a dynamic glass-transition accommodated by a broad enthalpy recovery, a remarkable temperature and deformational uniformity, and an enthalpy trend that validates the adiabatic constraint, are accurately simulated. The platform is thought of as a useful tool for modeling the dynamic response and process evolution of metallic glasses under rapid uniform heating.

A method of rapidly heating and shaping an amorphous metal using a rapid capacitor discharge has recently been introduced [54]. This method utilizes Joule heating to uniformly heat, rheologically soften, and thermoplastically shape metallic glasses rapidly (typically with processing times in the millisecond range). The method utilizes the discharge of electrical energy (typically 100 J to 100 kJ) stored in a capacitor to uniformly and rapidly heat a sample of metallic glass to a predetermined process temperature within the supercooled liquid region in a time scale of several milliseconds or less. This process proceeds from the observation that metallic glass, by its virtue of being a frozen liquid, has a relatively high electrical resistivity that depends weakly on temperature, which results in highly dissipative, efficient, spatially uniform, and nearly adiabatic heating of the material. By uniformly heating a bulk metallic glass in milliseconds, the stability of the supercooled liquid against crystallization is dramatically extended. Such a process has provided experimental access to physical properties such as enthalpy and viscosity in the entire range of the metastable liquid, as this range is no longer limited by crystallization on such short time scales. In the present study, a quantitative description of the rapid capacitive discharge process and a thorough analysis of the

physical properties of the metallic glass over the inaccessible temperature regime are attempted. Specifically, a finite-element model is developed to describe the effective coupling between electrical energy dissipation, heat generation, and fluid flow under the application of electrical discharge and deformational force. The heating and flow response of the metallic glass is simulated and contrasted to experimental data gathered under identical conditions. Thermodynamic and rheological models are presented that have been extended to apply beyond the temperature ranges associated with typical experiments into regimes typically inaccessible under conventional heating rates. Moreover, for the first time a model for the glass transition has been developed in order to simulate the dynamic glass transition under these ultra-high heating rates. When incorporated into the finite element simulation, these models yield excellent agreement with the thermodynamic and rheological data gathered in the experiments of Johnson et al. [54]. The finite element model introduced here can be thought of as a computational platform for implementing process and property simulation studies that extend outside the supercooled liquid regime accessible by conventional heating.

5.1 Modeling transport phenomena

The analytic model in the present study was built to conform closely to the experiment of Johnson et al. [54]. The samples used in those experiments were as-cast Vitreloy 1 ($Zr_{41.2}Ti_{13.8}Cu_{12.5}Ni_{10}Be_{22.5}$) rods with radius $\sim$ 2 mm and length $\sim$ 2 cm. The rods were placed between parallel copper electrodes, heated by capacitive discharge and deformed between two parallel ceramic discs with holes in the center. Various voltages and compression forces were used. The ceramic discs were used due to their very low thermal conductivity so that the heat dissipated into the environment is negligible and the adiabatic assumption is ensured. The central holes in the ceramic discs have also aided in alignment and uniformity of deformation. The sample's effective deforming length between the ceramic discs was $\sim$ 8 mm. In the present model, a cylindrical domain 2 mm in radius and 8 mm in length effectively simulates the samples in the experiments of Johnson et al. [54]. Considering the cylindrical geometry of the sample, a 2-dimensional model with axial symmetry is constructed using the COMSOL Multiphysics finite element analysis software. A mesh with $\sim$ 10,000 triangular elements was generated. The element size and growth rate were adjusted to optimal values, and the ratio between the element area minimum and maximum was adjusted to 0.002. The mesh elements at the boundaries were small enough to capture the steep gradients in strain rate, while the total element number still ensured the overall calculation load to be manageable on a stand-alone computer. Since the sample deformed severely in the experiment, the arbitrary Lagrange-Euler (ALE) method was adopted to generate a moving mesh. The model accommodated three component mechanisms coupled together: electrical conduction, heat generation and viscous deformation.

5.1.1 Electrical conduction

The circuit implemented in the experiment of Johnson et al. [54] was an effective RLC circuit with the time constant $\tau = L/R$ and damping factor $\zeta = (R/2)\sqrt{C/L}$, where R is the total resistance comprising the sample resistance R_s and system resistance R_0, L is the inductance and C the capacitance. The following values were reported [54]: $C \sim 0.264F$, $L \sim 2.4\mu H$, $R_s \sim 3m\Omega$, and $R_0 \sim 2.85m\Omega$. Together, these values yield a damping factor $\zeta \sim 1$. So the circuit was near its critical damping point. This gives the fastest and most effective capacitor discharge and also a relatively simple description of the electric current. Here, the time-dependent current is taken to have a simple exponential time decay function

$$I(t) = K \cdot t \cdot exp(-\frac{t}{2\tau}) \tag{5.1}$$

where K is a normalization constant obtained by integrating the time-dependent power over the total discharge time. This gives the total energy stored in the capacitor as

$$E_{tot} = \frac{1}{2}CV_{tot^2} = \int_0^\infty I(t)^2(R_0 + R_s)dt \tag{5.2}$$

where V_{tot} is the applied voltage.

Substituting Eqn. (5.1) into Eqn. (5.2) and integrating gives the normalization constant K as

$$K = \frac{V_{tot}}{2\tau}\sqrt{\frac{C}{\tau(R_0 + R_s)}} \tag{5.3}$$

Substituting Eqn. (5.3) into (5.1), the effective time-dependent voltage at the moving (top) boundary, $V = IR_s$, can be obtained as

$$V = \frac{1}{2}V_{tot}R_s\frac{t}{\tau}\sqrt{\frac{C}{\tau(R_0 + R_s)}}exp(-\frac{t}{2\tau}) \tag{5.4}$$

The stationary (bottom) boundary of the sample was grounded with $V = 0$. The two side boundaries are assumed to be electrically insulated.

Within the ultra-short discharge time window, the electric field and current are varying rapidly, which brings about electromagnetic effects that can cause non-uniformities in the sample, such as eddy currents and skin depth. Eddy currents are induced when a conductor is exposed to a changing magnetic field. They can generate heat and forces like all electric currents. Lenzs law states that eddy currents develop secondary flux opposing the external flux. This opposing field is strongest at the center of the conductor, with the resulting total current density greatest at the surface. The total current density declines exponentially, leading to non-uniformity over the conductors cross-section.

An analysis of the temperature difference between the sample surface and interior was presented by Lohofer and Pottlacher [55].

Here, we investigate the effect of this non-uniformity by resorting to the general form of Maxwells equation: $\bigtriangledown \times \mathbf{H} = \mathbf{J} + \frac{\partial \mathbf{D}}{\partial t}$, where $\mathbf{H}$ is the magnetic field, $\mathbf{J}$ is the current density and $\mathbf{D}$ is the electrical induction field. The first half period of a harmonic function is used to describe the rapid increase and damping of the actual current in our RLC circuit with time constant τ. When the actual current reaches its peak value at 2τ (which is obtained by taking the derivative of Eq. (5.1) to be zero), it corresponds to one quarter of a whole period. Then the harmonic AC frequency should be set at $f = 1/8\tau$. We should note that after 4τ, this analogy is not applicable, since the actual current nearly vanishes instead of alternating. However, the first 4τ is adequate to analyze the uniformity of the field. We solve the 2D skin effect problem for the circular cross-section of the sample using COMSOL Multiphysics AC Power Electromagnetics module. The following equation is solved

$$(j\omega\sigma - \omega^2\epsilon_0)\mathbf{A} + \bigtriangledown \times (\mu_0^{-1}\mu_r^{-1} \times \mathbf{A}) - \sigma\mathbf{v} \times (\bigtriangledown \times \mathbf{A}) = 0 \tag{5.5}$$

where j is the current density scalar, $\omega = 2\pi f$ is the alternating frequency, σ is the material conductivity, ϵ_0 and μ_0 are the permittivity and permeability in vacuum, μ_r is the relative permeability of the material, $\mathbf{A}$ is the magnetic potential vector, and $\mathbf{v}$ is the electron drift velocity. The boundary condition is set to be a virtual current density on the external boundary to make the magnetic field vanish outside our domain. This virtual current should be of same value and opposite sign of the real current throughput.

Using the data above for Vit1, we calculate a skin depth ~ 0.04 m, which is 20 times larger than the sample radius. This indicates that the current is uniformly distributed over the sample. No variation in current density is observed within the mesh resolution (Figure 5.1 a). Therefore, as long as we correctly describe the changing voltage or current, we could actually simplify the whole problem into a DC system, neglecting the effect of varying fields and inductance. However, this simplification is only suitable for this specific sample and alloy system. Different sample dimensions, permeability or circuit setup, will lead to different skin depths. For example, if we consider a ferromagnetic metallic glass sample (e.g., Fe-based or Co-based glass) with exactly the same dimensions and same circuit setup but with a different relative permeability of 1×10^4, the corresponding skin depth would drop to 0.004 m. With a sample radius of 0.002 m, a very obvious variation of current density can be observed (Figure 5.1 b). Therefore, uniform heating cannot be guaranteed for ferromagnetic samples without further modifying the circuit setup. Yet in the Vit1 case discussed here, the DC and uniform heating model can be safely implemented.

The differential equation considered in the simulation to describe the direct current electrical

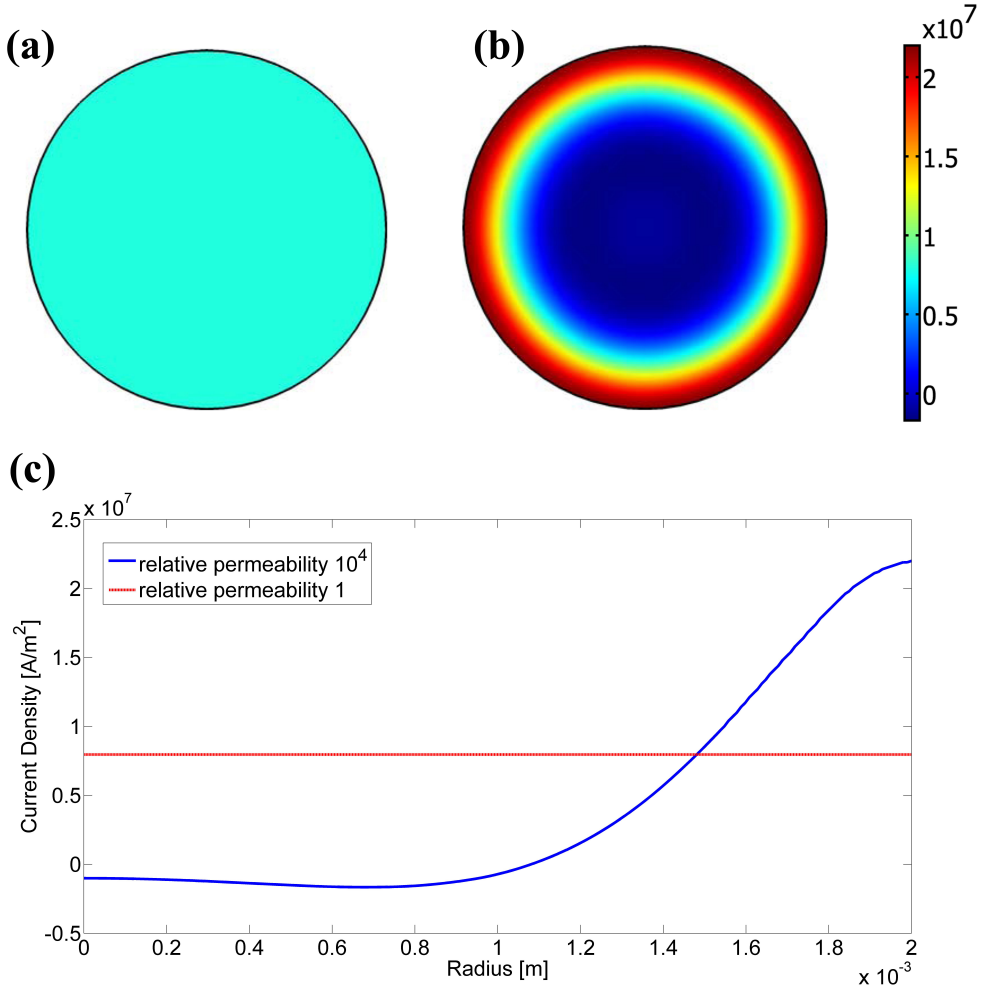

Figure 5.1: Skin depth for non-ferromagnetic and ferromagnetic materials

conduction was simply Joule's law

$$\bigtriangledown \cdot (\sigma(T) \bigtriangledown V) = 0 \tag{5.6}$$

where V is the electrical potential (voltage) field distribution over the sample and $\sigma(T)$ is the temperature-dependent conductivity

$$\sigma(T) = \frac{1}{r_0(1 + \alpha(T - T_0))} \tag{5.7}$$

For Vit 1, the resistivity at $T_0 = 300K$ is $r_0 = 1.91\mu\Omega \cdot m$, and the temperature coefficient is $\alpha = -1.2^{-4}K^{-1}$.

5.1.2 Heat generation

The thermal energy transfer in the sample was described by Fourier's law

$$\rho C_P \frac{\partial T}{\partial t} - \bigtriangledown \cdot (k \bigtriangledown T) = Q_{dc} \tag{5.8}$$

where the heat source $Q_{dc} = \sigma| \bigtriangledown V|^2$. The density $\rho = 6107kgm^3$ and the thermal conductivity $k = 10.83W((m \cdot K))$, both are assumed to be constant with temperature. The heat capacity C_P by contrast is strongly dependent on temperature, as will be discussed later in detail. Here the uniformity of the heating process is guaranteed by the negative temperature coefficient of resistivity α, as introduced in the previous section. Since α of supercooled liquid is negative and also fairly small, temperature fluctuations would be smoothed out without leading to numerical instability [56, 57].

5.1.3 Viscous deformation

Ignoring any compressibility effects in the supercooled liquid region, the incompressible Navier-Stokes equations can be assumed to apply within the applicable region of Newtonian flow [58]

$$\rho \frac{\partial \mathbf{u}}{\partial t} + \rho(\mathbf{u} \cdot \bigtriangledown)\mathbf{u} = \bigtriangledown \cdot [-P\mathbf{I} + \eta((\bigtriangledown \mathbf{u}) + (\bigtriangledown \mathbf{u})^T)] + \mathbf{F} \tag{5.9}$$

where P describes the liquid pressure (is identity matrix), and body force $\mathbf{F}$ is from gravity. The velocity at the stationary (bottom) boundary of the sample is set to zero. The moving (top) boundary was assumed to be driven by the force applied by the pneumatic piston. However, the actual inertia force experienced by the sample was different from the pneumatic force applied by the piston, because the top electrode assembly had a considerable mass that was moving as a flyer with a certain acceleration that had to be taken into account. Hence, the real-time effective force at the

upper boundary varied with time as follows

$$\mathbf{F}(t) = \mathbf{F}_0 + m_0\mathbf{g} + m_0\mathbf{a}(t) \tag{5.10}$$

Here $\mathbf{F}_0$ is the input from the pneumatic gauge, $m_0 \sim 1.15kg$ is the mass of the electrode flyer, and $\mathbf{a}(t)$ is the time-varying acceleration.

The temperature-dependent Newtonian viscosity for Vit 1 is taken as [24]

$$\eta(T) = \eta_\infty exp[\frac{W_g}{k_B T} exp(2n(1 - \frac{T}{T_g^0}))] \tag{5.11}$$

where W_g is given by $k_B T_g^0 ln(\eta_g/\eta_\infty)$. The Newtonian viscosity limit at T_g^0 is $\eta_g = 10^{12} Pa \cdot s$, where $T_g^0 = 613K$ is the "static" glass transition temperature (attained under infinitesimally-slow heating/cooling rate) as we introduced in the "fragility" section of Chapter 3. Paramters η_∞ and n are fitting parameters for Vit1, with the values of $9.3^{-3} Pa \cdot s$ and 0.93 respectively.

5.2 Modeling thermodynamics and kinetics

5.2.1 Dynamic glass transition temperature and heat capacity

The heat capacity of the metallic glass sample is required as an input into the model. The heat capacity for the undercooled liquid can be expressed from [59] as

$$C_P^{liq} = 3\mathcal{R} + (7.5 \times 10^{-3}[K] \cdot T + \frac{8.17 \times 10^6 [K^2]}{T^2})[J/mole \cdot K] \tag{5.12}$$

Here $\mathcal{R} = 8.31 J/mole \cdot K$ is the gas constant. The heat capacity of the glass, C_P^g, can be described by the first two terms in the above expression. With a heating rate of 20 K/min, typical in a calorimetric scan, a smooth jump is typically attained from C_P^g to $C_P^l iq$ around $T_g^0 \sim 613K$, as shown in Figure 5.2 (crystallization is not relevant here). However, the heating rate in the present millisecond-heating model is so rapid that the sample would remain in its glass state considerably above T_g^0, since the atoms won't have enough time to rearrange in order to relax the glass to the supercooled liquid state. The relaxation will begin at a dynamic T_g much higher than T_g^0, when the internal relaxation time scale has dropped considerably such as to be able to compete with the external heating time scale. The internal relaxation time is approximated by the Maxwell relaxation time constant, given as the ratio of viscosity to shear modulus: $\tau_M = \eta/G$, where both η and G are functions of temperatures [37, 60]. Here, we use a temperature-dependent function for τ_M as [11]:

$$\tau_M = \frac{\eta_\infty exp[\frac{W_g}{k_B T} exp(2n(1 - \frac{T}{T_g^0}))]}{G_g exp(n(1 - \frac{T}{T_g^0}))} \tag{5.13}$$

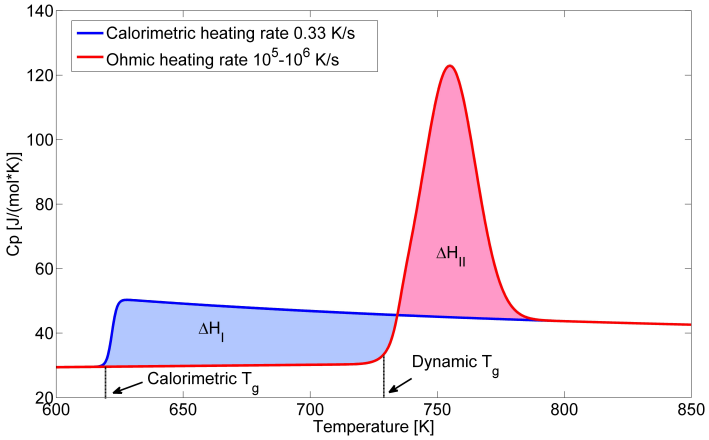

Figure 5.2: Dynamic glass transition temperature

which describes the internal time scale for configurational change in the glass. G_g is the shear modulus at T_g^0, and has the value of 33.2 GPa for Vit 1.

This internal time scale τ_M needs to match the time scale for external heating, τ_{ext}, given by

$$\tau_{ext} = \frac{\Delta T}{\dot{T}} \tag{5.14}$$

where $\dot{T}$ is the heating rate. The characteristic temperature scale ΔT effectively accounts for the temperature change during the glass transition, since such transition is a dynamic process evolving over a temperature range, rather than a unique temperature. Based on experimental evidence it is reasonable to assume $\Delta T \sim 10K$. The heating rate $\dot{T}$ is simply the power generated divided by the heat capacity. Using the heat capacity of glass (the first two terms in Eqn. (5.12)), the heating rate prior to the glass transition can be calculated as

$$\dot{T} = \frac{I^2 R_s}{C_P^g} = \frac{\frac{1}{4}\frac{V_{tot}^2}{\tau^3}\frac{C}{(R_0+R_s)R_s}t^2 exp(-\frac{t}{\tau})}{(3\mathcal{R} + 7.5\times 10^{-3}[K^{-1}]\cdot T)\cdot(m/M)} \tag{5.15}$$

where m is the sample mass and M is the molar mass of Vit 1. Substituting Eqn. (5.15) back to Eqn. (5.14) gives an explicit expression for the external heating time scale. Therefore, we have explicit expressions for the two time scales, τ_M and τ_{ext}, both as functions of temperature. When the two are equal, we can extract the onset temperature of the dynamic glass transition, T_g.

Starting from this new dynamic T_g, the heat capacity increases drastically to a peak value and drops back to the heat capacity of the liquid state. This peak accounts for the so-called enthalpy recovery, which represents the accumulated enthalpy stored in the glass state. In order to describe this peak, we introduce a quasi-step function and a quasi-delta function which are modified to give a certain degree of smoothness to ensure numerical stability. The following expression is used to

describe how heat capacity behaves after reaching T_g

$$C_P = 3\mathcal{R} + [7.5 \times 10^{-3}T + \frac{8.17 \times 10^6}{T^2}(\frac{1}{2} + \frac{1}{2}tanh(\frac{T - \Delta T - T_g}{\Delta T/3})) + Aexp(-\frac{(T - 3\Delta T - T_g)^2}{2(\Delta T)^2})]J/mole \cdot K \quad (5.16)$$

where $\Delta T \sim 10K$. Here the coefficient A is a mathematical constant that we will now solve for. This peak value in C_P characterizes the enthalpy recovery from the glass state to the liquid state. Thus, the two shaded areas in Figure 5.2 should be equal.

ΔH_I is the temperature integral of $C_P^{liq} - C_P^{glass}$ (which is simply the third term in Eqn. (5.12)) from $T_g^0 = 613K$ to the dynamic T_g, so that

$$\begin{aligned} \Delta H_I &= \int_{T_g^0}^{T_g} (C_P^{liq} - C_P^{glass})dT \\ &= \int_{613}^{T_g} \frac{8.17 \times 10^6}{T^2} dT = 8.17 \times 10^6 (\frac{1}{613} - \frac{1}{T_g}) \end{aligned} \quad (5.17)$$

Similarly, ΔH_{II} is approximately the integral of the Gaussian function (the last term of Eqn. (5.16)) from the dynamic T_g to $6\Delta T$ above it. Then

$$\begin{aligned} \Delta H_{II} &= \int_{T_g}^{T_g + 6\Delta T} Aexp(-\frac{(T - 3\Delta T - T_g)^2}{2(\Delta T)^2})dT \\ &\approx \int_{-\infty}^{\infty} Aexp(-\frac{(T - 3\Delta T - T_g)^2}{2(\Delta T)^2})dT = A\sqrt{2\pi}\Delta T \end{aligned} \quad (5.18)$$

Letting $\Delta H_I = \Delta H_{II}$, we get the peak value A which is dependent on T_g. Thus we arrive at an explicit function of heat capacity based on Eqn. (5.16).

5.3 Simulation results

5.3.1 Heating

Using the sample parameters defined above and an applied capacitor voltage of $V_{tot} \sim 78V$, a simulation of rapid capacitive discharge heating and forming is performed on the present platform. The simulated temperature response is shown in Figure 5.3. The dynamic T_g in the simulation is found to be $\sim$ 725K. The heating curve overall agrees well with the experimental curve obtained in the study of Johnson et al. [54] under essentially identical process conditions. The general solution to the heat generation problem in the absence of a glass transition is given by

$$T = T_0 + \frac{R_s C V_{tot}^2}{2C_P}[1 - exp(-\frac{t}{\tau})(1 + \frac{t}{\tau}(1 + \frac{t}{2\tau}))] \quad (5.19)$$

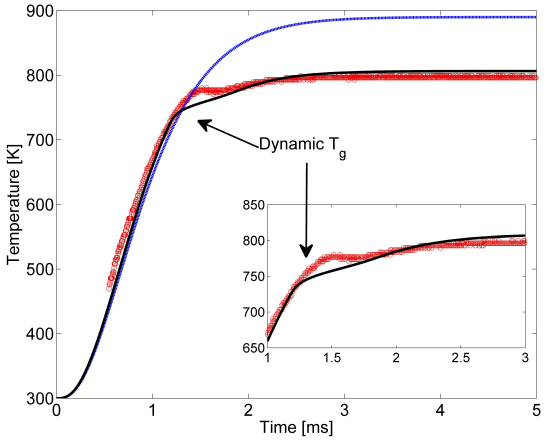

Figure 5.3: Heating: temperature dependence on time

Here C_P is the heat capacity of the glass state, and can be approximated by $3\mathcal{R}$. Where the two curves depart indicates the onset of glass transition, which corresponds to the dynamic T_g in Figure 5.2. The solution to Eqn. (5.19) is superimposed on the heating curve in Figure 5.3 to exemplify the effect of the glass transition on heating.

With the aid of the simulation, the effect of V_{tot} on T_g can be investigated. V_{tot} is varied to change the heating rate $\dot{T}$ in order to trigger different dynamic T_g. The condition for the onset of glass transition $\tau_M = \tau_{ext}$ can be expressed as $\dot{T} = \Delta T/\tau_M$, where $\Delta T \sim 10K$. The right-hand side is explicitly dependent on temperature. Also, the temperature approximately follows Eqn. (5.19) until it reaches T_g. Combining Eqn. (5.14) and Eqn. (5.19) we can express the heating rate as a function of temperature rather than time. Figure 5.4 shows a family of heating rate curves for different voltages ranging from 60V to 105V. The intersection with the $\Delta T/\tau_M$ curve describes the onset condition, i.e., the dynamic T_g for a specific voltage. As shown in Figure 5.5, merely increasing the voltage results in a diminishing ability to achieve a higher T_g, since in Eqn. (5.15) the increase in voltage will be greatly offset by the decrease in time duration of heating up.

5.3.2 Temperature and deformation

Eqn. (5.11) along with appropriate boundary conditions can be implemented to predict the spatial temperature profile and overall deformation of the sample. Figure 5.6 provides a straightforward comparison between experimental and simulation results. The images in the left column were taken by a high-speed infrared camera in the study by Johnson et al, with their temperatures indicated by the colormap. On the same scale, the simulation results (right column) give matching temperature and deformation. The images in the right column are from the simulation animation and are continuous in time, allowing for a comparison with the camera. As shown in Figure 5.7, the experimental

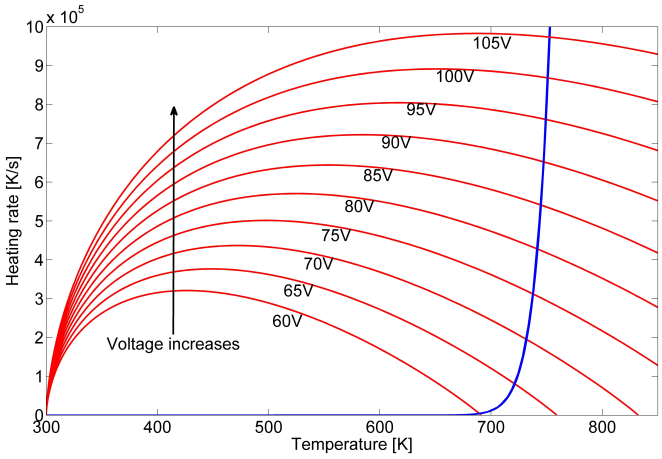

Figure 5.4: Heating rate curves with varying applied voltage

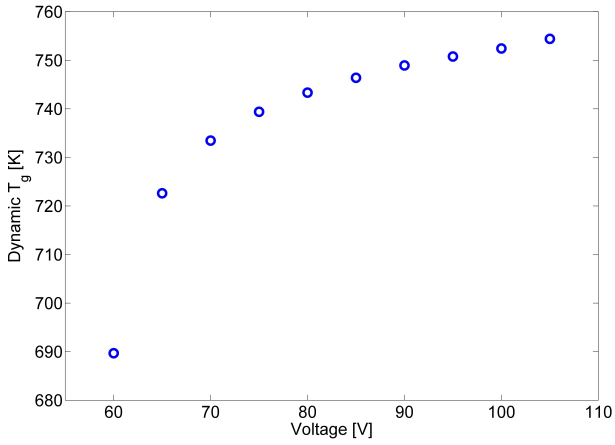

Figure 5.5: Dynamic Tg dependence on applied voltage

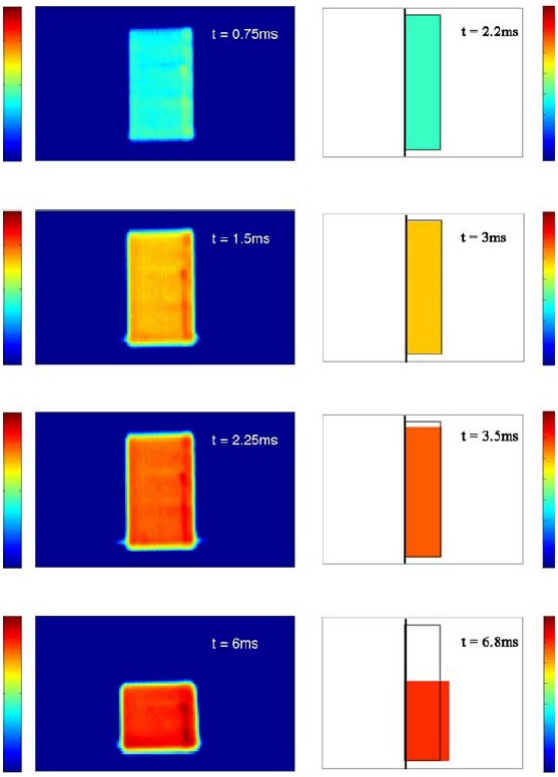

Figure 5.6: Snapshots of sample heating and deformation

data taken from a high-speed camera are consistent with the computational prediction, while the latter provides further details for analysis. This agreement strongly supports the self-consistency of the simulation platform.

5.3.3 Enthalpy

The applied voltage V_{tot} is varied to get different final steady-state temperatures and accordingly different enthalpy values. During this process, the effective time window is short enough (tens of milliseconds), and the very low thermal conductivity of air and the ceramic discs ($\sim$ 3 W/mK) minimizes the heat loss from the sample into the environment. Under these circumstances, we can make a reasonable assumption that the whole process is nearly adiabatic. Assuming that the side boundary is thermally insulated, the thermal energy generated is fully converted into enthalpy. Therefore, we can get a mapping between enthalpy and temperature in the supercooled liquid region, as shown in Figure 5.8. Experimental data reproduced from the study by Johnson et al. [54] and a fit using Eqn. (5.12) are also presented. Excellent agreement between simulation and experiment can be observed.

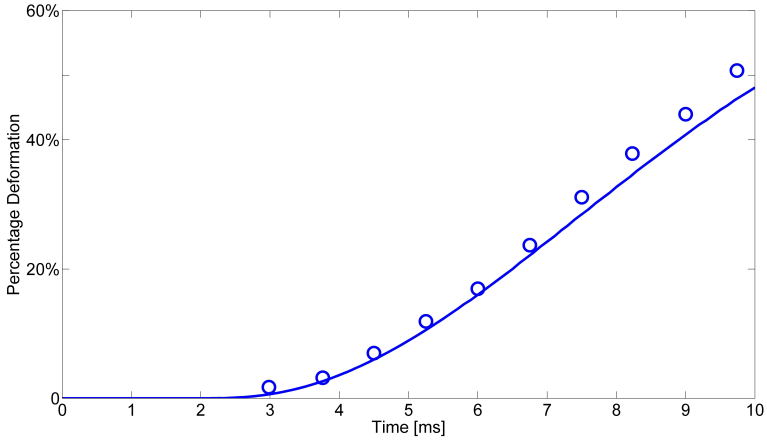

Figure 5.7: Time-dependent sample deformation from simulation and experiment

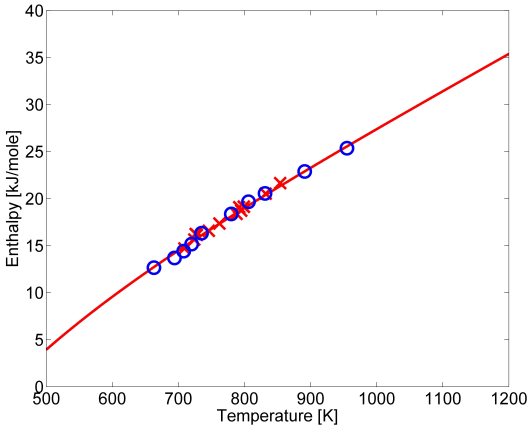

Figure 5.8: Temperature-dependent enthalpy

5.4 Summary

A quantitative description of the rapid Ohmic heating and forming process for metallic glasses was built on a finite-element modeling platform. The platform incorporates models for the material properties that capture the features of the metallic glass behavior through the glass transition under rapid heating conditions. These features include: (1) the temperature-dependent resistivity with a negative temperature coefficient; (2) the temperature-dependent heat capacity, exhibiting a jump at the dynamic glass transition accommodating the enthalpy recovery; and (3) the temperature-dependent Newtonian viscosity of the metallic glass across the supercooled regime. Under conditions essentially identical to the experiments, the platform yields results that quantitatively replicate all features of the experiment output. Specifically, the simulation demonstrates: (1) the temperature response of the sample closely resembles the experimental response, accurately capturing the glass transition and associated enthalpy recovery; (2) the dynamic glass-transition temperature is predicted with reasonable accuracy; (3) the remarkable temperature uniformity during heating is validated; (4) the deformational response is closely replicated; and (5) the calculated enthalpy closely matches the experimental trends and validates the adiabatic constraint. In summary, the simulation platform introduced in this work accurately predicts and evaluates the behavior of metallic glasses in the rapid Ohmic heating and forming process. More broadly, the simulation platform can be thought of as a useful tool for modeling the dynamic response and process evolution of a metallic glass under rapid uniform heating and forming.

Bibliography

[1] W. Klement, R. H. Willens, and P. Duwez. Noncrystalline structure in solidified gold-silicon alloys. *Nature*, 187:869–870, 1960.

[2] P. Duwez and S. C. H. Lin. Amorphous ferromagnetic phase in fepc alloys. *Journal of Applied Physics*, 38:4096, 1967.

[3] A. Inoue, T. Zhang, and T. Masumoto. Glass-forming ability of alloys. *Journal of Non-Crystalline Solids*, 156(8):473–480, 1993.

[4] N. Nishiyama Inoue and T. Matsuda. Preparation of bulk glassy pdnicup alloy of 40mm in diameter by water quenching. *Materials Transactions JIM*, 37(2):181–184, 1996.

[5] A. Peker and W. L. Johnson. A highly processable metallic glass-zrticunibe. *Applied Physics Letters*, 63(17:2342–2344, 1993.

[6] M. N. Chandrasekharaiah. Magnetic properties and applications. In M. N. Chandrasekharaiah, editor, *Metallic glasses: production, properties and applications*. Trans Tech Publications, 1984.

[7] J Durand. Magnetism in transition metal base amorphous alloys. In R. Hasegawa, editor, *Glassy metals:magnetic, chemical and structural properties*. CRC Press, 1983.

[8] R. C. O'Handley, L. I. Mendelsohn, R. Hasegawa, R. Ray, and S. Kavesh. Lowfield magnetic properties of fe80b20 glass. *Journal of Applied Physics*, 47:4660, 1976.

[9] H. Warlimont. The impact of amorphous soft magnetic alloys. *Materials Science and Engineering*, 99:1–10, 1988.

[10] R. Hasegawa. Present status of amorphous soft magnetic alloys. *J. Magn. Magn. Mater.*, 215:240–245, 2000.

[11] R. C. O'Handley, R. Hasegawa, R. Ray, and C. P. Chou. Ferromagnetic properties of some new metallic glasses. *Applied Physics Letters*, 29:330, 1976.

[12] R. Hasegawa and R. C. O'Handley. Soft magnetic properties of metallic glasses-recent developments. *Journal of Applied Physics*, 50:1551, 1979.

[13] T. D. Shen and R. B. Schwarz. Bulk ferromagnetic glasses prepared by flux melting and water quenching. *Applied Physics Letters*, 75:49, 1999.

[14] A. Inoue, B. L. Shen, H. Koshiba, H. Kato, and A. Yavari. Cobalt-based bulk glassy alloy with ultrahigh strength and soft magnetic properties. *Nature Materials*, 2:661, 2002.

[15] M. D. Demetriou, G. Kaltenboecj, J. Y. Suh, G. Garrett, M. Floyd, C. Crewdsom, D. C. Hofmann, H. Kozachkov, A. Wiest, J. P. Schramm, and . L. Johnson. Glassy steel optimized for glass-forming ability and toughness. *Applied Physics Letters*, 95:041907, 2009.

[16] J. H. Na, M. Demetriou, W. L. Johnson, and G. Garrett. Bulk nickle-based chromium and phosphorous bearing metallic glasses, 02 2013.

[17] J Durand. Magnetic properties of metallic glasses. In H. Beck and H. J. Guntherodt, editors, *Topics in applied physics: glassy metals II*. Springer-Verlag, 1983.

[18] N. A. Spaldin. In *Magnetic materials: fundamentals and device applications*. Cambridge University Press.

[19] A. Makino, T. Kubota, C. Chang, M. Makabe, and A. Inoue. Fesibp bulk metallic glasses with high magnetization and excellent magnetic softness.

[20] U. Koster and U. Herold. Crystallization of metallic glasses. In H. Beck and H. J. Guntherodt, editors, *Topics in applied physics: glassy metals I*. Springer-Verlag, 1983.

[21] D. C. Hofmann, J. Y. Suh, A. Wiest, G. Duan, M. L. Lind, M. D. Demetriou, and W. L. Johnson. Designing metallic glass matrix composites with high toughness and tensile ductility. *Nature*, 451:1085, 2008.

[22] C. V. Thompson and F. Spaepen. Crystal nucleation in metallic melts. *Acta Metall.*, 31:2021–2027, 1983.

[23] M. E. McHenry, M. A. Willard, and D. E. Laughlin. Amorphous and nanocrystalline materials for applications as soft magnets. *Progress in Materials Science*, 44:291–433, 1999.

[24] William L. Johnson, Marios D. Demetriou, Johnson S. Harmon, Mary L. Lind, and Konrad Samwer. Rheology and ultrasonic properties of metallic glass forming liquids: a potential energy landscape perspective. *MRS Bulletin*, 32:644–650, 2007.

[25] D. R. Gaskell. *Introduction to the thermodynamics of materials*. Taylor and Francis, 1995.

[26] W. L. Johnson. Model for configurational density of states. work in progress, 2013.

[27] X. H. Lin and W. L. Johnson. Formation of tizrcuni bulk metallic glasses. *Journal of Applied Physics*, 78:6514–6519, 1995.

[28] Jong Hyun Na, Marios D. Demetriou, and William L. Johnson. Fragility of iron-based glasses. *Applied Physics Letters*, 99:161902, 2011.

[29] G. J. Fan, J. F. Loffler, R. K. Wunderlich, and H. J. Fecht. Thermodynamics, enthalpy relaxation and fragility of the bulk metallic glass-forming liquid pd43ni10cu27p20. *Acta Materialia*, 52:667–674, 2004.

[30] V. N. Novikov and A. P. Sokolov. *Nature*, 442, 2006.

[31] J. Jackle. Residue entropy in glasses and spin glasses. *Physica B*, 127:79, 1984.

[32] W. Vogel. Residue entropy in glasses and spin glasses. *Physics Z*, 22:645, 1921.

[33] G. S. Fulcher. Residue entropy in glasses and spin glasses. *Journal of American Ceramic Society*, 8:339, 1925.

[34] K. Biswas, S. Venkataraman, W. Y. Zhang, S. Ram, and J. Eckert. Glass-forming ability and fragility parameter of amorphous fe67co9.5nd3dy0.5b20. *Journal of Applied Physics*, 100:023501, 2006.

[35] P. G. Debenedetti and F. H. Stillinger. Supercooled liquids and the glass transition. *Nature*, 410:259, 2001.

[36] F. H. Stillinger. A topological view of supercooled liquids and glass formation. *Science*, 267:1935–1939, 1995.

[37] M. L. Lind, G. Duan, and W. L. Johnson. Isoconfigurational elastic constants and liquid fragility of a bulk metallic glass forming alloy. *Physical Review Letters*, 97:015501, 2006.

[38] L. M. Wang, V. Velikov, and C. A. Angell. Direct determination of kinetic fragility indices of glassforming liquids by dsc: kinetic versus thermodynamic fragilities. *Journal of Chemical Physics*, 117:10184, 2002.

[39] David Lynch. Winning the global race of solar silicon. *JOM*, 61, 2009.

[40] X. H. Lin, W. L. Johnson, and W. K. Rhim. Effect of oxygen impurity on crystallization of an undercooled bulk glass forming zrticunial alloy. *Materials Transactions, JIM*, 38(5):473–477, 1997.

[41] R. D. Conner, R. E. Maire, and W. L. Johnson. Effect of oxygen concentration upon the ductility of amorphous zr57nb5al10cu15.4ni12.6. *Materials Science and Engineering A*, 419:148–152, 2006.

[42] S. Mukherjee, Z. Zhou, J. Schroers, W. L. Johnson, and W. K. Rhim. Overheating threshold and its effect on time-temperature-transformation diagrams of zr based bulk metallic glasses. *Applied Physics Letters*, 84:5010–5012, 2004.

[43] B. Sundman. An assessment of the fe-o system. *J. Phase Equilib.*, 1991.

[44] D. A. Porter and K. E. Easterling. *Phase transformations in metals and alloys.* Chapman and Hall, 1994.

[45] R. Hasegawa. Application of metallic glasses in low-frequency magnetic devices. In R. Hasegawa, editor, *Glassy metals:magnetic, chemical and structural properties.* CRC Press.

[46] P. Weiss. La variation du ferromagnetisme avec la temperature. *Compt. Rend.*, 143:1136–1139, 1906.

[47] B. D. Cullity. *Introduction to magnetic materials.* Addison-Wesley publishing company, 1972.

[48] A. E. Berkowitz and E. Kneller. *Magnetism and metallurgy.* Academic press, 1969.

[49] A. I. Gubanov. Quasi-classical theory of amorphous ferromagnets. *Sov. Phys. Solid State*, 2:468, 1960.

[50] T. Kaneyoshi. Theory of magnetism in noncrystlline solids. In R. Hasegawa, editor, *Glassy metals:magnetic, chemical and structural properties.* CRC Press.

[51] F. E. Luborsky. Composition dependence of the curie temperatures of amorphous alloys. *J. App. Phys.*, 51:2808, 1980.

[52] R. Clarke. Plotting magnetization curves. Technical report, University of Surrey, 2008.

[53] R. Boll, H. R. Hilzinger, and H. Warlimont. Magnetic material properties and applications of metallic glasses in electronic devices. In R. Hasegawa, editor, *Glassy metals:magnetic, chemical and structural properties.* CRC Press, 1983.

[54] W. L. Johnson, G. Kaltenboeck, M. D. Demetriou, J. P. Schramm, X. Liu, K. Samwer, P. Kim, and D. C. Hofmann. Beating crystallization in glass-forming metals by millisecond heating and processing. *Science*, 332:828, 2011.

[55] G. Lohofer and G. Pottlacher. *Int. J. Thermophys.*, 26:1239, 2005.

[56] H. J. Guntherodt. *Adv. Solid State Phys.*, 17:25, 1977.

[57] S. R. Nagel. *Phys. Rev. B*, 16:1694, 1977.

[58] J. Lu, G. Ravichandran, and W. L. Johnson. *Acta Mater.*, 51:3429, 2003.

[59] R. Busch, Y. J. Kim, and W. L. Johnson. Thermodynamics and kinetics of the undercooled liquid and the glass transition of the vit1 alloy. *J. Appl. Phys.*, 77:4039, 1995.

[60] M. D. Demetriou, J. S. Harmon, M. Tao, G. Duan, K. Samwer, and W. L. Johnson. *Phys. Rev. Lett.*, 97:065502, 2006.